

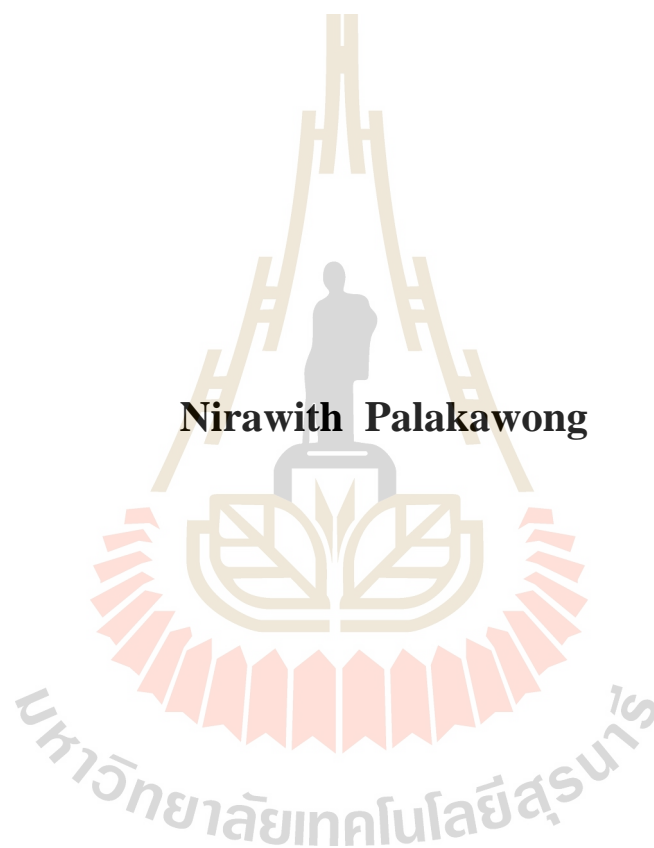
การศึกษาแบบเฟสต์พรินซิเพิลของความบกพร่องชนิดแทนที่
ในโลหะออกไซด์และโลหะไนไตรด์



นายนิรวิทย์ ปาลกะวงศ์ ณ อยุธยา

วิทยานิพนธ์นี้เป็นส่วนหนึ่งของการศึกษาตามหลักสูตรปริญญาวิทยาศาสตรดุษฎีบัณฑิต
สาขาวิชาฟิสิกส์
มหาวิทยาลัยเทคโนโลยีสุรนารี
ปีการศึกษา 2559

**FIRST-PRINCIPLES STUDY OF SUBSTITUTIONAL
DEFECTS IN METAL OXIDES AND
METAL NITRIDES**

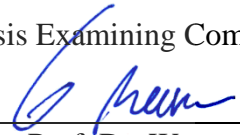


**A Thesis Submitted in Partial Fulfillment of the Requirements for the
Degree of Doctor of Philosophy in Physics
Suranaree University of Technology
Academic Year 2016**

**FIRST-PRINCIPLES STUDY OF SUBSTITUTIONAL
DEFECTS IN METAL OXIDES AND
METAL NITRIDES**

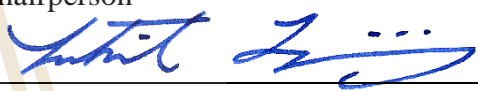
Suranaree University of Technology has approved this thesis submitted in partial fulfillment of the requirements for the Degree of Doctor of Philosophy.

Thesis Examining Committee



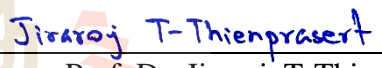
(Asst. Prof. Dr. Worawat Meevasana)

Chairperson



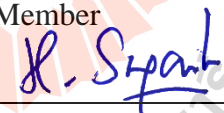
(Prof. Dr. Sukit Limpijumnong)

Member (Thesis Advisor)



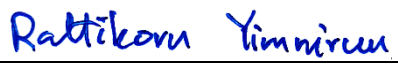
(Assoc. Prof. Dr. Jiraroj T-Thienprasert)

Member



(Prof. Dr. Kritsana Sagarik)

Member



(Assoc. Prof. Dr. Rattikorn Yimnirun)

Member



(Prof. Dr. Sukit Limpijumnong)

Vice Rector for Academic Affairs
and Innovation



(Prof. Dr. Santi Maensiri)

Dean of Institute of Science

นิรวิทย์ ปาลกะวงษ์ ณ อยุธยา : การศึกษาแบบเฟสดีฟรินซิเพิลของความบกพร่องชนิด
แทนทีในโลหะออกไซด์และโลหะไนไตรด์ (FIRST-PRINCIPLES STUDY OF
SUBSTITUTIONAL DEFECTS IN METAL OXIDES AND METAL NITRIDES)
อาจารย์ที่ปรึกษา : ศาสตราจารย์ ดร.ชูกิจ ลิมปิจำนงค์, 130 หน้า.

ความบกพร่องและสารเจือปนต่าง ๆ ในสารกึ่งตัวนำไม่ว่าจะเกิดขึ้นเองโดยธรรมชาติหรือ
เกิดขึ้นจากความตั้งใจก็ตามล้วนมีผลกระทบต่อคุณสมบัติของวัสดุ ในวิทยานิพนธ์ฉบับนี้
จะมุ่งเน้นการศึกษาความบกพร่องที่เกิดขึ้นจากการแทนที่บนตำแหน่งของแคตไอออนและแอน
ไอออนด้วยอะตอมชนิดอื่น ๆ ในกลุ่มของสารประกอบโลหะออกไซด์และโลหะไนไตรด์ที่มี
องค์ประกอบสองชนิดด้วยวิธีการคำนวณแบบเฟสดีฟรินซิเพิลที่อยู่บนพื้นฐานของทฤษฎี
ฟังก์ชันนัลความหนาแน่น โดยวัตถุประสงค์ของวิทยานิพนธ์ฉบับนี้สามารถแบ่งออกได้เป็นสาม
ส่วนหลัก ๆ ได้แก่ ส่วนที่หนึ่ง เพื่อศึกษาความบกพร่องชนิดที่เกิดจากการแทนที่อะตอม N ลงใน
กลุ่มของสารประกอบโลหะออกไซด์ที่มีองค์ประกอบสองชนิดและการแทนที่อะตอม O ลงในกลุ่ม
ของสารประกอบโลหะไนไตรด์ที่มีองค์ประกอบสองชนิด เพื่อศึกษาความสัมพันธ์ของความ
บกพร่องแบบการแทนที่ดังกล่าวในกลุ่มของสารประกอบโลหะออกไซด์และโลหะไนไตรด์ที่
แตกต่างกัน ส่วนที่สอง เพื่อตรวจสอบสภาพแวดล้อมเฉพาะที่ของ Mg ในสารตัวอย่างที่ได้จากการ
เจือ Mg ลงในสารประกอบ ZnO ด้วยวิธีการผสมผสานกันระหว่างการคำนวณแบบเฟสดีฟรินซิเพิล
และเทคนิคการวัดการดูดกลืนรังสีเอกซ์ และส่วนที่สาม เพื่อศึกษาผลของความเค้นต่อระดับ
พลังงานตัวรับที่เกิดจากอะตอม Ga ที่เข้าไปแทนที่อะตอม Sn ในสารประกอบ SnO₂ โดยความเค้น
ที่เกิดขึ้นนั้นสามารถสร้างขึ้นโดยการบีบอัดขนาดของเซลล์ผลึกโดยตรงหรือการเจืออะตอมอื่นที่
เล็กกว่าอะตอม Sn ลงไปเพื่อแทนที่ตำแหน่งของอะตอม Sn

สาขาวิชาฟิสิกส์
ปีการศึกษา 2559

ลายมือชื่อนักศึกษา นิรวิทย์ ปาลกะวงษ์ ณ อยุธยา
ลายมือชื่ออาจารย์ที่ปรึกษา ดร. ชูกิจ ลิมปิจำนงค์

NIRAWITH PALAKAWONG : FIRST-PRINCIPLES STUDY OF
SUBSTITUTIONAL DEFECTS IN METAL OXIDES AND METAL
NITRIDES. THESIS ADVISOR : PROF. SUKIT LIMPIJUMNONG, Ph.D.
130 PP.

FIRST-PRINCIPLES/DEFECTS/METAL OXIDES/METAL NITRIDES

The defects and impurities in semiconductors, which are intentionally or unintentionally introduced, have a significant effect on material properties. In this thesis, the substitutional defects for cation's and anion's sites in various selected binary metal-oxides/nitrides were theoretically investigated by using first-principles density functional calculations. The main purposes of this thesis can be classified into three parts: (1) investigation of N and O substitutional defects in selected binary metal oxides/metal nitrides to determine the relationship of these substitutional defects among different metal oxides/nitrides, (2) identification of local environments of Mg in $Mg_xZn_{1-x}O$ alloy sample by using a combination of first-principles calculations and x-ray absorption spectroscopy, and (3) investigation of Ga acceptor defect level in SnO_2 with/without compressive strains by directly compressing the unit cell or alloying with the smaller cation to create the strain.

School of Physics

Academic Year 2016

Student's Signature Nirawith Palakawong

Advisor's Signature Sukit Limpijumnong

ACKNOWLEDGEMENTS

This thesis would not be completed without supports of many persons. First of all, I would like to express my sincere gratitude to Prof. Dr. Sukit Limpijumnong, my thesis advisor, for giving me a chance to be a Ph.D. student with the Royal Golden Jubilee Ph.D. scholarship and all kindly support for my Ph.D. study and related researches. Besides my thesis advisor, I would like to express thanks to Asst. Prof. Dr. Worawat Meevasana, Assoc. Prof. Dr. Jiraroj T-Thienprasert, Prof. Dr. Kritsana Sagarik, and Assoc. Prof. Dr. Rattikorn Yimnirun for contributing as the thesis examining committee members. I would like to thank Prof. Dr. Shengbai Zhang for his kindness allowed me to join his group for almost a year in Rensselaer Polytechnic Institute (RPI), NY, USA. I would like to acknowledge the Thailand Research Fund for all financial support through the Royal Golden Jubilee Ph.D. Program (Grant No. PHD/0180/2552).

Moreover, I would like to express my thankfulness to Assoc. Prof. Dr. Jiraroj T-Thienprasert for his kindly supervision since I began to do research. I also thank Dr. Yi-Yang Sun and all members in Prof. Dr. Shengbai Zhang's group for their kindly carefulness, discussion, and guide me during staying in RPI, USA. I would like to thank the School of Physics, Suranaree University of Technology, all members in our research group, and all members in the Computational Materials Unit at the Department of Physics, Kasetsart University.

Most importantly, I would like to thank my family for great supporting me. At the end, I am also grateful to my beloved wife, Mrs. Suppanart Palakawong, for her helpful and encouragement anytime.

Nirawith Palakawong



CONTENTS

	Page
ABSTRACT IN THAI.....	I
ABSTRACT IN ENGLISH.....	II
ACKNOWLEDGEMENTS.....	III
CONTENTS.....	V
LIST OF TABLES.....	IX
LIST OF FIGURES.....	XI
LIST OF ABBREVIATIONS.....	XVII
CHAPTER	
I INTRODUCTION	1
1.1 Overview of the Calculation Approaches.....	4
1.2 Research Objectives.....	5
1.3 Scope and Limitation of the Studies.....	6
1.4 References.....	7
II THEORETICAL BACKGROUNDS	12
2.1 Earlier Approaches.....	12
2.2 Density Functional Theory.....	14
2.2.1 The Hohenberg-Kohn Theorems.....	14
2.2.2 The Kohn-Sham Equations.....	15
2.3 The Exchange-Correlation Energy Functional.....	17

CONTENTS (Continued)

	Page
2.3.1 The Local Density Approximation (LDA).....	17
2.3.2 The Generalized Gradient Approximation (GGA).....	18
2.3.3 The Hybrid Functional.....	19
2.4 Bloch's Theorem and Plane Wave Basis Sets.....	20
2.5 <i>K</i> -points Sampling and Special <i>k</i> -points.....	21
2.6 Pseudopotential and Projector Augmented-Wave Method.....	22
2.7 The Hellmann-Feynman Theorem.....	24
2.8 Electronic Ground State Calculation with Vienna <i>Ab Initio</i> Simulation Package (VASP).....	25
2.9 Theory of X-ray Absorption Spectroscopy.....	27
2.10 References.....	29
III NITROGEN AND OXYGEN SUBSTITUTIONAL DEFECTS IN SELECTED METAL OXIDES AND METAL NITRIDES.....	33
3.1 Introduction.....	33
3.2 Computational Details.....	35
3.2.1 Structural Relaxations.....	36
3.2.2 Formation Energy of Defect Calculations.....	37
3.2.3 Defect Transition levels.....	39
3.2.4 Band Alignment calculations.....	40
3.3 Results and Discussion.....	42
3.3.1 Bulk Properties.....	42

CONTENTS (Continued)

	Page
3.3.2 Defect Properties.....	46
3.3.2.1 Defect Positioning.....	46
3.3.2.2 Defect Formation Energies.....	47
3.3.2.3 Defect Transition Levels.....	48
3.3.2.4 Band Alignment Calculations.....	51
3.4 Conclusions.....	55
3.5 References.....	56
IV LOCAL STRUCTURE OF MAGNESIUM IN	
MAGNESIUM ZINC OXIDE ALLOY.....	61
4.1 Introduction.....	61
4.2 Experimental Details.....	63
4.3 Computational Details.....	63
4.4 Results and Discussion.....	66
4.4.1 Zn and Mg K-edge XANES measurements.....	66
4.4.2 Computational Results.....	69
4.4.2.1 Intrinsic and Mg Defects in WZ-ZnO.....	69
4.4.2.2 Formation of Complex Defects between Mg and Other Native point Defects.....	71
4.4.2.3 Clustering of Mg _{zn} in WZ-ZnO.....	71
4.4.2.4 The 5-fold Mg _{zn}	73
4.5 Conclusions.....	74

CONTENTS (Continued)

	Page
4.6 References.....	75
V GALLIUM ACCEPTOR DEFECTS IN TIN DIOXIDE	
REVISITED: A HYBRID FUNCTIONAL STUDY.....	80
5.1 Introduction.....	80
5.2 Computational Details.....	82
5.3 Results and Discussion.....	86
5.4 Conclusions.....	92
5.5 References.....	92
VI CONCLUSIONS AND FUTURE RESEARCHES.....	96
APPENDICES	
APPENDIX A THE ASSOCIATED CRYSTAL STRUCTURES OF THE SELECTED METAL OXIDES AND METAL NITRIDES.....	99
APPENDIX B PUBLICATIONS AND PRESENTATIONS.....	101
CURRICULUM VITAE.....	130

LIST OF TABLES

Table	Page
3.1 The calculated lattice parameters of selected metal oxides with LDA and GGA functionals accompanying with the corresponding experimental values. The values in the parenthesis represent the percentage error between the calculated and the experimental values.....	43
3.2 The calculated lattice parameters of selected metal nitrides with LDA and GGA functionals accompanying with the corresponding experimental values. The values in the parenthesis represent the percentage error between the calculated and the experimental values.....	45
3.3 The summary of non-polar plane used in the surface calculations for selected metal oxides to determine the electrostatic potential difference (ΔV) between bulk-like and vacuum regions obtained from LDA and GGA functionals.....	51
3.4 The summary of non-polar plane used in the surface calculations for selected metal nitrides to determine the electrostatic potential difference (ΔV) between bulk-like and vacuum regions obtained from LDA and GGA functionals.....	52

LIST OF TABLES (Continued)

Table	Page
4.1 The phase fractions of Mg (f_{Mg}) and Zn (f_{Zn}) in 6-fold coordination of $\text{Mg}_x\text{Zn}_{1-x}\text{O}$ alloys obtained by linear combination fits between 4-fold WZ and 6-fold RS spectra for each Mg and Zn K -edge XANES measurements. The RS phase fractions (F_{RS}) were obtained from Eq. (4.3).	67
5.1 The calculated lattice parameters (a and c), internal parameter (u), and cell volume (Ω) of SnO_2 and SiO_2 in the tetragonal rutile structure by using the GGA-PBE and HSE functionals accompanied with the corresponding experimental values.	83
5.2 The calculated parameters of 72-atom SnO_2 with and without alloying with Si atom. L_x , L_y , and L_z are the expanded cell dimensions in relative to the primitive cell parameters, where $L_x = L_y = 2a$ and $L_z = 3c$. The parameters for the alloy are explicitly calculated only for the GGA-PBE case. For HSE calculations, the compression ratio obtained from the GGA-PBE case (-6.22%) is used to calculate the alloy parameters relative to bulk SnO_2 (the cell shape of the alloy is approximated to be a cube, i.e., $L_x = L_y = L_z = \Omega^{1/3}$).	89

LIST OF FIGURES

Figure	Page	
2.1	The illustrations of the pseudo wave function and pseudopotential. The dash blue lines represent the real wave function (ψ) and real Coulomb potential (V). The solid red lines represent the corresponding pseudo wave function (ψ_{pseudo}) and pseudopotential (V_{pseudo}). The cutoff radius (r_c) marked by the vertical dash line represents the boundary at which the real quantities become identical with pseudo quantities. This figure is reproduced from Ref. (Wolfram, 2006)......	23
2.2	The self-consistent scheme used in VASP codes to calculate the electronic ground state total energy and wave function of the system.....	26
2.3	The measured Zn <i>K</i> -edge XAS spectrum of Zn foil. The XANES and EXAFS regions are indicated. The data obtained from Ref. (Ravel and Newville, 2005)......	27
2.4	The illustration of electrons in the core levels. The electron in the <i>K</i> -shell can be excited to higher unoccupied state by absorbing incoming x-ray energy, which is equal or greater than the binding energy of that electron creating the photoelectron. <i>K</i> , <i>L</i> , and <i>M</i> indicate the absorption edges.....	28
3.1	The calculated total energy of rocksalt-MgO as a function of lattice constant for determining the equilibrium lattice constant. The black dots and red line represent the calculated and fit datas, respectively.....	36

LIST OF FIGURES (Continued)

Figure	Page
3.2 The illustration of the surface calculations for determining the electrostatic potential different between bulk-like and vacuum regions in wurtzite-AlN. The green and red balls represent Al and N atoms, respectively. The planar and macroscopic averages of the electrostatic potential are showed in red and blue lines, respectively.	41
3.3 The illustration of the calculated heat of formations of selected metal-oxides/nitrides obtained from LDA (red circles) and GGA (blue squares) functionals compared with the available experimental values (black plus signs).	47
3.4 The illustration of the calculated defect formation energies of neutral N_O defect in metal oxides under metal-rich (top panel) and metal-poor (bottom panel) growth conditions. The red circles and blue squares represent the calculated results with LDA and GGA functionals, respectively.	48
3.5 The illustration of the calculated defect formation energies of neutral O_N defect in metal nitrides under metal-rich (top panel) and metal-poor (bottom panel) growth conditions. The red circles and blue squares represent the calculated results with LDA and GGA functionals, respectively.	49

LIST OF FIGURES (Continued)

Figure	Page
3.6	Schematic diagram for the defect transition levels $\varepsilon(0/-1)$ of No defect in selected metal oxides obtained from LDA (black lines) and GGA (red lines) functionals. The calculated VBM of each compound is set to zero.....50
3.7	The illustrations of (a) CBM, (b) defect transition level $\varepsilon(0/-)$, and (c) VBM aligned with the vacuum level for selected metal oxides obtained from LDA (black filled circles) and GGA (red filled circles) functionals. The blue circles represent group I oxides (Li_2O , Na_2O , K_2O , and Rb_2O) having the same antifluorite structure and the blue squares represent group II oxides (MgO , CaO , and SrO) having the same rocksalt structure.....53
3.8	The illustrations of (a) CBM and (b) VBM positions aligned with the vacuum level for selected metal nitrides obtained from LDA (black filled circles) and GGA (red filled circles) functionals. The blue squares represent group II nitrides (Be_3N_2 , Mg_3N_2 , Ca_3N_2 , and Sr_3N_2) having the same antibixbyite structure and the blue triangles represent group III nitrides (AlN , GaN , and InN) having the same wurtzite structure.....54
4.1	The measured (a) Zn <i>K</i> -edge and (b) Mg <i>K</i> -edge XANES spectra of MZO alloys. The number labeled on each spectrum is the Mg mole fraction (<i>x</i>). For the mixed phase (<i>x</i> = 0.15 and 0.50), the linear combination fits based on 4-fold WZ and 6-fold RS spectra for each cation species are shown using dashed lines.....66

LIST OF FIGURES (Continued)

Figure	Page
4.2 Phase fractions of $Mg_xZn_{1-x}O$ alloy with different the Mg mole fraction (x) as determined by the linear combination fits from measured Zn and Mg K -edge XANES spectra (black circle). The area under (above) the black curve represents the fraction of 6-fold RS (4-fold WZ) phase. The cation compositions for each phase were represented by different color, magenta and green for Mg and Zn, respectively.	68
4.3 The illustration of formation energies of native defects and Mg defects in WZ-ZnO as a function of Fermi level calculated under Zn-rich (left panel) and O-rich (right panel) growth conditions. The slope of each line indicates the charge state of the defect. The Fermi level, referenced to the (special k -point) VBM of bulk, is shown up to the calculated band gap at the special k -point (the vertical dashed line).	70
4.4 Calculated Mg K -edge XANES spectra of $MgZn$ in WZ-ZnO (a) with random configurations and (b) with cluster configurations at different Mg concentrations. (c) Calculated Mg K -edge XANES spectrum of HX-MgO structure compared to that of RS-MgO (upper curve) and $MgZn$ in WZ-ZnO (lower curve).	72
5.1 Schematic illustration of the structures for $Si_xSn_{1-x}O_2$ alloy (a), $GaSn$ in $Si_xSn_{1-x}O_2$ alloy at <i>inside</i> (b) and <i>outside</i> (c) Si-cluster configurations. The red, green, blue, and yellow balls represent Sn, O, Si, and Ga atoms, respectively.	85

LIST OF FIGURES (Continued)

Figure	Page
5.2 (a) The total energy (ΔE) of Ga_{Sn}^0 in bulk SnO_2 as a function of the Ga's displacement (d) near the saddle point. The total energy of the Ga_{Sn}^0 at the <i>on-center</i> configuration ($d = 0.00 \text{ \AA}$) is set to be zero and the vertical dashed line marks the mirror symmetry point. (b) Ga atom is moved along the Ga-O bond, as indicated by the blue arrow, until one Ga-O bond appears broken and the total energy is reduced by 0.5 eV. The localized hole states on the oxygen atom nearby Ga_{Sn} are depicted as a gray color.	87
5.3 Defect transition levels $\varepsilon(0/-)$ associated with Ga_{Sn} in four configurations, i.e., (a) bulk SnO_2 , (b) $\text{Si}_x\text{Sn}_{1-x}\text{O}_2$ alloy with <i>inside</i> configuration, (c) $\text{Si}_x\text{Sn}_{1-x}\text{O}_2$ with <i>outside</i> configuration, and (d) 6.22% compressed bulk SnO_2 . In the plot, the valence band maximum for each configuration is set to be zero.	91

LIST OF FIGURES (Continued)

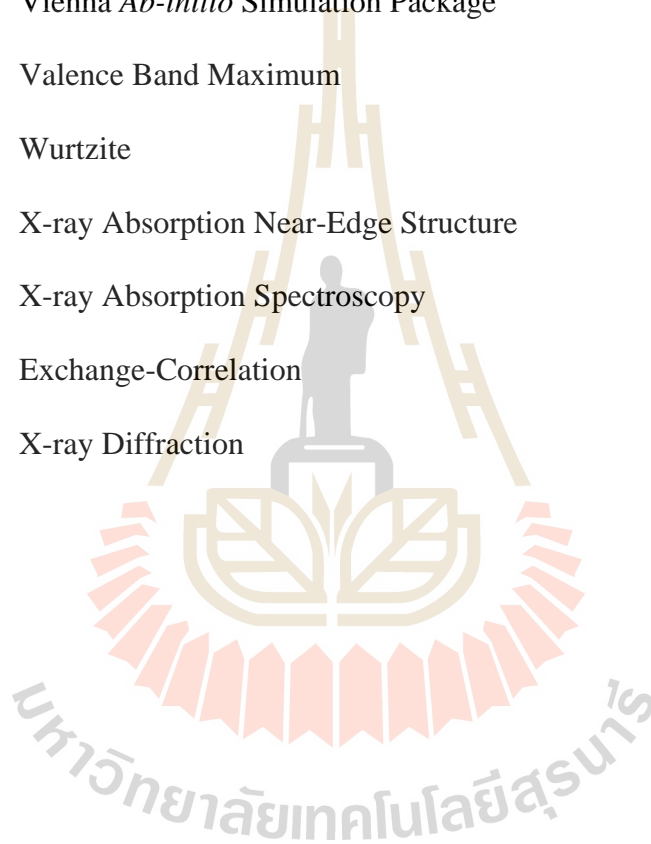
Figure		Page
A.1	<p>The associated crystal structures of the selected metal-oxides/nitrides, i.e., (a) the antifluorite structure for Li_2O, Na_2O, K_2O, and Rb_2O, (b) the wurtzite structure for BeO, AlN, GaN, and InN, (c) the rocksalt structure for MgO, CaO, and SrO, (d) the corundum structure for Al_2O_3, (e) the monoclinic structure for Ga_2O_3, (f) the bixbyite structure for In_2O_3, (g) the hexagonal structure for Li_3N, and (h) the antibixbyite structure for Be_3N_2, Mg_3N_2, Ca_3N_2, and Sr_3N_2. The green (larger) and red (smaller) balls represent the cations (metal atoms) and anions (O for metal oxides and N for metal nitrides) positions, respectively.</p>	100

LIST OF ABBREVIATIONS

BZ	Brillouin Zone
CBM	Conduction Band Minimum
DFT	Density Functional Theory
EXAFS	Extended X-ray Absorption Fine Structure
GGA	Generalized Gradient Approximation
HEG	Homogeneous Electron Gas
HSE	Heyd, Scuseria, and Ernzerhof
HX	Unbuckled Wurtzite
LDA	Local Density Approximation
LED	Light-Emitting Diode
LR	Long-Range
MZO	Magnesium Zinc Oxide ($\text{Mg}_x\text{Zn}_{1-x}\text{O}$)
PAW	Projector Augmented-Wave
PBE	Perdew, Burke, and Ernzerhof
RF	Radio Frequency
RMM-DIIS	Residual Minimization Scheme-Direct Inversion in the Iterative Subspace
RS	Rocksalt
SLRI	Synchrotron Light Research Institute
SR	Short-Range

LIST OF ABBREVIATIONS (Continued)

SSD	Solid-State Drive
TCOs	Transparent Conductive Oxides
UV A	Ultra Violet A
VASP	Vienna <i>Ab-initio</i> Simulation Package
VBM	Valence Band Maximum
WZ	Wurtzite
XANES	X-ray Absorption Near-Edge Structure
XAS	X-ray Absorption Spectroscopy
XC	Exchange-Correlation
XRD	X-ray Diffraction



CHAPTER I

INTRODUCTIONS

In solid state physics, materials can be classified into three main categories based on their electrical property, i.e., conductor, insulator, and semiconductor. While electrons in the conductor can move freely, electrons in insulator cannot flow. The electrical property of semiconductor is between conductor and insulator and it can be controlled or modified into desired way by adding or doping with other elements; making it suitable for a wide range of many technological applications, such as optoelectronic devices including light-emitting diode (LED), laser diode, and solar cell (Green, 1982; Jeff, 1999; Zheludev, 2007), memory storage technology for solid-state drive (SSD) (Russell and Cohn, 2012), and photocatalyst for environmental purifications (Na Phattalung et al., 2017; Nakata and Fujishima, 2012).

In semiconductors, the defects, which have an important impact on their physical properties, are point defects. They can be classified into two types, i.e., intrinsic and extrinsic defects. For intrinsic defects, the electrical conductivity in semiconductor arises by itself without doping other elements, such as the missing of host atoms from its lattice sites called vacancy defect, the insertion of host atoms into vacant sites called interstitial defect, and the exchange of atoms in different sites called antisite defect. Regarding extrinsic defects, the electrical conductivity in materials can be controlled or modified by intentionally or unintentionally adding other elements into materials. For examples, doping silicon (Si) with phosphorus (P)

causes an extra electron donating from each P atom making Si become *n*-type semiconductor because these extra electrons are the majority carrier. On the other hand, Si can be turned into *p*-type semiconductor when doped with boron (B). This is because doping Si with B will create holes, which become the majority carrier. In addition, it has been reported that hydrogen (H) is one of the most unintentional defects incorporating in the metal oxide materials (McCluskey et al., 2012; Norby et al., 2004). This strongly affects the electronic and optical properties of materials.

In nature, the two most abundant compositions in the air are composed of nitrogen (N) and oxygen (O), i.e., about 78.08% and 20.95% by volume for N and O, respectively (Brimblecombe, 1996). Therefore, during the crystal growth process, N and O atoms might incorporate into the crystal affecting the physical property of material. For metal oxide and metal nitride materials, since the atomic sizes of N and O are comparable, i.e., 0.65 Å and 0.60 Å for N and O, respectively (Slater, 1964), N atom might substitute on the O sites in metal oxide materials forming N_O defect. Similarly, O atom has a tendency to substitute on the N sites forming O_N defect in metal nitride materials. This can affect some physical properties of metal oxide and metal nitride materials. The understanding of the physical properties related to these defects in both metal oxide and metal nitride materials is therefore the crucial fundamental for controlling and improving material properties into desired ways.

Several binary metal oxide and metal nitride materials have attracted great attention due to their excellent properties, making them suitable for a wide range of applications such as, electronic and optoelectronic devices (Davis, 1991; Henini and Razeghi, 2004; Yu et al., 2016), photocatalyst applications (Asahi et al., 2001; Gromov and Chukhlomina, 2015; Khan et al., 2015), and high-power and high-

temperature electronic applications (Ambacher, 1998; Gangler, 1950; Stampfl and Van de Walle, 1998). Although many research groups have paid attention on the studies of N defect in metal oxides (Elfimov et al., 2007; Haffad et al., 2012; Lee et al., 2001; Rignanese et al., 1997; Varley et al., 2011) and O defect in metal nitrides (Graciani et al., 2009; Harris et al., 1993; Mattila and Nieminen, 1996; Orellana and Chacham, 2000; Piquini et al., 1997), the connections of N/O defects in different oxide/nitride materials are still limited. In this thesis, N_O defect in various metal oxide materials and O_N defect in various metal nitride materials will be systematically investigated to determine the connection of N/O defects in several metal oxide/nitride materials.

In addition, it has been reported that the band gap of some materials could be adjusted by adding other element. This technique is called the band gap engineering (Ohtomo et al., 1998). For example, the band gap of InN can be tuned from ~ 0.7 to ~ 3.6 eV by adding O into a crystal to form InN_xO_{1-x} (T-Thienprasert et al., 2008). Regarding zinc oxide (ZnO), which is the most interesting wide band gap semiconductors, the band gap is ~ 3.3 eV limited to the ultraviolet A (UVA) region (Srikant and Clarke, 1998). Therefore, to make it usable for the application in higher energy regions, magnesium oxide (MgO), which has the band gap of 7.8 eV (Taurian et al., 1985), is mixed into ZnO to tune the band gap of this material called magnesium zinc oxide ($Mg_xZn_{1-x}O$ or MZO) alloy. Therefore, in principle, the band gap of MZO alloy can be adjusted to any values between 3.3 and 7.8 eV depending on the Mg composition (x). However, due to the difference in crystal structures between wurtzite (WZ) ZnO and rocksalt (RS) MgO, the fundamental understanding of the

local structures of Mg in MZO alloy with different compositions is quite important for controlling the electrical and optical properties of MZO alloy.

Finally, in order to make semiconductor usable for a wide range of electronic devices, the semiconductor must be able to be doped into both of *n*- and *p*-types. Regarding tin dioxide (SnO₂), which is one of the most interesting ceramic materials (Jarzebski and Marton, 1976; Jarzebski and Morton, 1976), as-grown SnO₂ exhibits *n*-type conductivity with a high carrier concentration (Fonstad and Rediker, 1971; Masahiro and Shigeo, 1971; Samson and Fonstad, 1973; Stjerna et al., 1990). In principle, substitution of group III elements for Sn's Site could make it *p*-type. However, the inherent *n*-type conductivity is an obstacle for making SnO₂ into *p*-type semiconductor. In addition, for the case of Na-doped ZnO, it has been reported that applying the compressive strain can make the acceptor level shallower and enhance the acceptor concentration (Sun et al., 2014). In this thesis, the acceptor level introduced by Ga acceptor defects in SnO₂ with and without compressive strain was investigated. The compressive strain effects on the acceptor level either by direct compression or alloying with smaller cations were studied in order to enhance the acceptor concentration.

1.1 Overview of the Calculation Approaches

In quantum mechanics, many physical properties of a crystal can be obtained from the wave function of the system by solving the Schrödinger equation, which contains too complicated interactions, i.e., nuclei-nuclei, nuclei-electron, and electron-electron interactions. These complicated interactions make the problem impossible to solve directly. As a result, there is an important theory purposed to simplify the

complicated Schrödinger equation into a solvable problem, i.e., density functional theory (DFT). In DFT calculations, the electron wave function will be replaced with the electron density and many electron-electron interactions will be mapped into the interactions between electrons and its density. This introduces the correction term in the potential energy called exchange-correlation (XC), which is a function of electron density. The two most common uses of XC functionals are the local density approximation (LDA) and the generalized gradient approximation (GGA). More theoretical details can be found in Chapter II. In this thesis, first-principles calculations based on DFT were used to systematically study the physical property of some defects in selected metal oxide and metal nitride materials.

1.2 Research Objectives

In this thesis, first-principles calculations based on density functional theory were used to systematically study the physical properties of substitutional defects in several selected binary metal oxides and metal nitrides. The thesis focuses on three main parts: (1) the N_O and O_N defects in selected binary metal oxides and metal nitrides, respectively, (2) Mg defects in MZO alloy, and (3) Ga acceptor defects in SnO_2 . For the first one, by systematically selecting metal oxides and metal nitrides to create the defects, the relation between the defect properties, such as defect formation energy and defect transition level can be determined. For the second, the detailed local structures of Mg in MZO alloy at different Mg concentration could be obtained and compared with the x-ray absorption measurements to confirm the calculated results. For the third, the compressive strain effects on the Ga acceptor defects in SnO_2 were investigated.

1.3 Scope and Limitation of the Studies

Based on first-principles density functional theory calculations, the N_O and O_N defects in selected binary metal oxides and metal nitrides, respectively, were systematically studied. The metal cations will be systematically selected from each group and row of the periodic table to form both metal oxides and metal nitrides, i.e., group I: lithium (Li), sodium (Na), potassium (K), and rubidium (Rb), group II: beryllium (Be), magnesium (Mg), calcium (Ca), and strontium (Sr), and group III: aluminium (Al), gallium (Ga), and indium (In). Several physical properties related to N_O defect in metal oxides and O_N defect in metal nitrides, such as the local relaxed geometries, the defect formation energies, and the defect transition levels will be examined. In addition, the relations of these physical properties in different metal oxides or metal nitrides were investigated. Second, the local structures of Mg in MZO alloy with different Mg concentrations were studied by using a combination of first-principles calculations and x-ray absorption spectroscopy (XAS) technique. The plausible forms of Mg in ZnO will be investigated by considering the defect formation energy. The local structures of the dominant defect will be used to generate the XAS spectrum to compare with the measured XAS spectrum of MZO alloy with different Mg concentrations. Last, the compressive strain effects on the Ga acceptor defects were studied to enhance the acceptor concentration in SnO_2 . All of the calculations were carried out by using Vienna *ab-initio* simulation package (VASP) codes based on density functional theory with LDA or GGA or hybrid functional for the exchange-correlation functional. For defect calculations, the supercell approach was used with a supercell size of ~50 - 120 atoms due to a limitation of our computational resources (512 CPUs, 2.4 GHz).

This thesis is organized as follows: chapter II briefly describes information of theoretical backgrounds used in this research. Chapter III illustrates some bulk properties and some physical properties related to N_O and O_N defects in selected binary metal oxides and metal nitrides, respectively. In chapter IV, the local structures of Mg in MZO alloy were investigated and compared with the experimental results. Chapter V, the acceptor level of Ga defects in SnO_2 was identified and the compressive strain effects on the acceptor level were investigated in order to enhance the acceptor conductivity of the SnO_2 . Finally, chapter VI gives summaries of all completed researches in this thesis and future works.

1.4 References

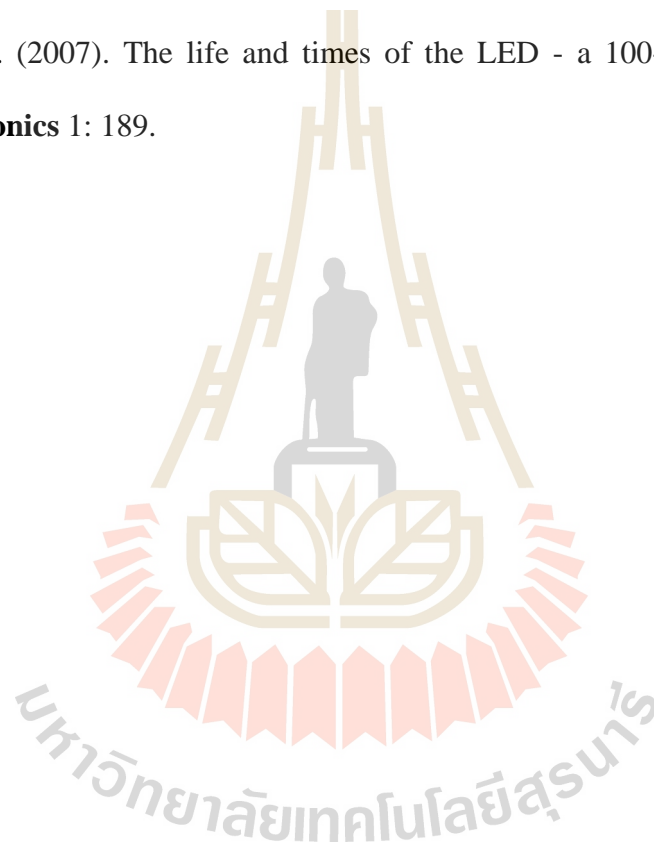
- Ambacher, O. (1998). Growth and applications of group III-nitrides. **Journal of Physics D: Applied Physics** 31: 2653.
- Asahi, R., Morikawa, T., Ohwaki, T., Aoki, K., and Taga, Y. (2001). Visible-light photocatalysis in nitrogen-doped titanium oxides. **Science** 293: 269.
- Brimblecombe, P. (1996). **Air Composition and Chemistry**. Cambridge University Press.
- Davis, R. F. (1991). III-V nitrides for electronic and optoelectronic applications. **Proceedings of the IEEE** 79: 702.
- Elfimov, I. S., Ruydi, A., Csiszar, S. I., Hu, Z., Hsieh, H. H., Lin, H. J., Chen, C. T., Liang, R., and Sawatzky, G. A. (2007). Magnetizing oxides by substituting nitrogen for oxygen. **Physical Review Letters** 98: 137202.
- Fonstad, C. G. and Rediker, R. H. (1971). Electrical properties of high-quality stannic oxide crystals. **Journal of Applied Physics** 42: 2911.

- Gangler, J. J. (1950). Some physical properties of eight refractory oxides and carbides. **Journal of the American Ceramic Society** 33: 367.
- Graciani, J., Hamad, S., and Sanz, J. F. (2009). Changing the physical and chemical properties of titanium oxynitrides $TiN_{1-x}O_x$ by changing the composition. **Physical Review B** 80: 184112.
- Green, M. A. (1982). **Solar cells: operating principles, technology, and system applications**. Prentice-Hall.
- Gromov, A. A. and Chukhlomina, L. N. (2015). **Nitride Ceramics: Combustion Synthesis, Properties and Applications**. Wiley.
- Haffad, S., Samah, M., and Cicero, G. (2012). Effect of nitrogen impurities on the physical properties of ZnO nanowires: First-principles study. **Physical Review B** 85: 165207.
- Harris, J. H., Enck, R. C., and Youngman, R. A. (1993). Photoinduced thermal-conductivity changes in aluminum nitride. **Physical Review B** 47: 5428.
- Henini, M. and Razeghi, M. (2004). **Optoelectronic Devices: III Nitrides**. Elsevier Science.
- Jarzebski, Z. M. and Marton, J. P. (1976a). Physical properties of SnO_2 materials: II. Electrical properties. **Journal of the Electrochemical Society** 123: 299C.
- Jarzebski, Z. M. and Morton, J. P. (1976b). Physical properties of SnO_2 materials: III. Optical properties. **Journal of the Electrochemical Society** 123: 333C.
- Jeff, H. (1999). **Semiconductor Diode Lasers-Structures**. Laser Guidebook, Second Edition, McGraw-Hill Professional, Access Engineering.
- Khan, M. M., Adil, S. F., and Al-Mayouf, A. (2015). Metal oxides as photocatalysts. **Journal of Saudi Chemical Society** 19: 462.

- Lee, E. -C., Kim, Y. S., Jin, Y. G., and Chang, K. J. (2001). Compensation mechanism for N acceptors in ZnO. **Physical Review B** 64: 085120.
- Masahiro, N. and Shigeo, S. (1971). Properties of oxidized SnO₂ single crystals. **Japanese Journal of Applied Physics** 10: 727.
- Mattila, T. and Nieminen, R. M. (1996). *Ab initio* study of oxygen point defects in GaAs, GaN, and AlN. **Physical Review B** 54: 16676.
- McCluskey, M. D., Tarun, M. C., and Teklemichael, S. T. (2012). Hydrogen in oxide semiconductors. **Journal of Materials Research** 27: 2190.
- Na Phattalung, S., Limpijumnong, S., and Yu, J. (2017). Passivated co-doping approach to bandgap narrowing of titanium dioxide with enhanced photocatalytic activity. **Applied Catalysis B: Environmental** 200: 1.
- Nakata, K. and Fujishima, A. (2012). TiO₂ photocatalysis: Design and applications. **Journal of Photochemistry and Photobiology C: Photochemistry Reviews** 13: 169.
- Norby, T., Wideroe, M., Glockner, R., and Larring, Y. (2004). Hydrogen in oxides. **Dalton Transactions**: 3012.
- Ohtomo, A., Kawasaki, M., Koida, T., Masubuchi, K., Koinuma, H., Sakurai, Y., Yoshida, Y., Yasuda, T., and Segawa, Y. (1998). Mg_xZn_{1-x}O as a II-VI widegap semiconductor alloy. **Applied Physics Letters** 72: 2466.
- Orellana, W. and Chacham, H. (2000). Energetics of carbon and oxygen impurities and their interaction with vacancies in cubic boron nitride. **Physical Review B** 62: 10135.
- Piquini, P., Mota, R., Schmidt, T. M., and Fazzio, A. (1997). Theoretical studies of native defects in cubic boron nitride. **Physical Review B** 56: 3556.

- Rignanese, G. M., Pasquarello, A., Charlier, J. C., Gonze, X., and Car, R. (1997). Nitrogen incorporation at Si(001)-SiO₂ interfaces: Relation between N 1s core-level shifts and microscopic structure. **Physical Review Letters** 79: 5174.
- Russell, J. and Cohn, R. (2012). **Solid-State Drive**. Book on Demand.
- Samson, S. and Fonstad, C. G. (1973). Defect structure and electronic donor levels in stannic oxide crystals. **Journal of Applied Physics** 44: 4618.
- Slater, J. C. (1964). Atomic radii in crystals. **The Journal of Chemical Physics** 41: 3199.
- Srikant, V. and Clarke, D. R. (1998). On the optical band gap of zinc oxide. **Journal of Applied Physics** 83: 5447.
- Stampfl, C. and Van de Walle, C. G. (1998). Energetics and electronic structure of stacking faults in AlN, GaN, and InN. **Physical Review B** 57: R15052.
- Stjerna, B., Granqvist, C. G., Seidel, A., and Häggström, L. (1990). Characterization of rf-sputtered SnO_x thin films by electron microscopy, Hall-effect measurement, and Mössbauer spectrometry. **Journal of Applied Physics** 68: 6241.
- Sun, Y. Y., Abtew, T. A., Zhang, P., and Zhang, S. B. (2014). Anisotropic polaron localization and spontaneous symmetry breaking: Comparison of cation-site acceptors in GaN and ZnO. **Physical Review B** 90: 165301.
- T-Thienprasert, J., Nukeaw, J., Sungthong, A., Porntheeraphat, S., Singkarat, S., Onkaw, D., Rujirawat, S., and Limpijumnong, S. (2008). Local structure of indium oxynitride from x-ray absorption spectroscopy. **Applied Physics Letters** 93: 051903.

- Taurian, O. E., Springborg, M., and Christensen, N. E. (1985). Self-consistent electronic structures of MgO and SrO. **Solid State Communications** 55: 351.
- Varley, J. B., Janotti, A., and Van de Walle, C. G. (2011). Mechanism of visible-light photocatalysis in nitrogen-doped TiO₂. **Advanced Materials** 23: 2343.
- Yu, X., Marks, T. J., and Facchetti, A. (2016). Metal oxides for optoelectronic applications. **Nature Materials** 15: 383.
- Zheludev, N. (2007). The life and times of the LED - a 100-year history. **Nature Photonics** 1: 189.



CHAPTER II

THEORETICAL BACKGROUNDS

2.1 Earlier Approaches

In quantum mechanics, especially in computational physics, the physical properties of material could be achieved from the wave function of the system by solving the exact Schrödinger equation,

$$\hat{H}\Psi = E\Psi, \quad (2.1)$$

where Ψ is the wave function of the system, E is the total energy, and \hat{H} is the Hamiltonian operator which is composed of the kinetic and potential energies of the system. In the materials, there are many electrons and nuclei in the system (called many-body system) resulting in very complicated interactions. As a result, the full Hamiltonian of the system can be expressed by,

$$\begin{aligned} \hat{H} = & -\sum_I \frac{\hbar^2}{2M_I} \nabla_I^2 - \sum_i \frac{\hbar^2}{2m} \nabla_i^2 \\ & + \frac{1}{2} \sum_I \sum_{J \neq I} \frac{e^2 Z_I Z_J}{|\mathbf{R}_I - \mathbf{R}_J|} + \frac{1}{2} \sum_i \sum_{j \neq i} \frac{e^2}{|\mathbf{r}_i - \mathbf{r}_j|} - \sum_I \sum_i \frac{e^2 Z_I}{|\mathbf{R}_I - \mathbf{r}_i|}, \end{aligned} \quad (2.2)$$

where the first two terms correspond to the kinetic energies of the nuclei and electrons, respectively, the third to the fifth terms are the Coulomb electrostatic potential energies between nuclei-nuclei, electrons-electrons and nuclei-electrons in the system, respectively. The above equation can be written in a more compact form

as

$$\hat{H} = \hat{T}_N(\mathbf{R}) + \hat{T}_e(\mathbf{r}) + \hat{V}_{NN}(\mathbf{R}) + \hat{V}_{ee}(\mathbf{r}) + \hat{V}_{Ne}(\mathbf{R}, \mathbf{r}), \quad (2.3)$$

where \mathbf{R} and \mathbf{r} are the sets of nucleus and electron position vectors, respectively, M_I and m are the masses of ion and electron, respectively, and Z_I is the atomic number of the nuclei. However, the full Schrödinger equation of many-body system is impossible to solve. To simplify the complicated Schrödinger equation, Born and Oppenheimer (Born and Oppenheimer, 1927) proposed that the motion of nuclei and electrons in the system can be separated due to the nucleus mass is too heavier than the electron mass. The motion of the nucleus is therefore much slower than that of the electron. Hence, the nuclei could be assumed to be static allowing us to neglect the kinetic energy of the nuclei. This approximation is known as Born-Oppenheimer approximation. Then, the electronic Hamiltonian (\hat{H}_e) can be written as

$$\hat{H}_e = \hat{T}_e(\mathbf{r}) + \hat{V}_{ee}(\mathbf{r}) + \hat{V}_{Ne}(\mathbf{R}, \mathbf{r}). \quad (2.4)$$

In addition, the Hartree and Fock proposed (Fock, 1930; Hartree, 1928) the method (Hartree-Fock method) to construct the wave function of the system by assuming that the many-electron wave function can be written as a product of one-electron wave functions, called a Hartree product, which can be obtained from the antisymmetric Slater determinant satisfied the Pauli exclusion principle. Hence, the Hartree-Fock equation of one-electron can be written as

$$\left(-\frac{\hbar^2}{2m} \nabla^2 + \hat{V}_{ee}(\mathbf{r}) + \hat{V}_{Ne}(\mathbf{r}) \right) \psi(\mathbf{r}) - \sum_i \int \frac{d\mathbf{r}'}{|\mathbf{r} - \mathbf{r}'|} \psi_i^*(\mathbf{r}') \psi(\mathbf{r}') \psi_i(\mathbf{r}) \psi^*(\mathbf{r}) = \varepsilon \psi(\mathbf{r}), \quad (2.5)$$

where the last term on the left hand side corresponds to the exchange term which is still complicated to calculate. In the next part, the theory, that can be used to reduce

the complicated Schrödinger equation into solvable problems by considering the electron density instead of the electron wave function called density functional theory, will be described.

2.2 Density Functional Theory

The density functional theory (DFT) has essential basic roots from the Thomas-Fermi model (Fermi, 2011; Thomas, 1927). The main objective of DFT is to reduce the complicated interactions by considering the electron density instead of the electron wave function. A brief theory of DFT will be explained in the following section.

2.2.1 The Hohenberg-Kohn Theorems

Hohenberg and Kohn (Hohenberg and Kohn, 1964) have demonstrated two theorems for the system of an electron moving under the influence of an external potential $v(\mathbf{r})$ that

- I) An external potential $v(\mathbf{r})$ and also the ground state total energy of a many-electron system are uniquely determined by the electron density $n(\mathbf{r})$, which depends on only three spatial coordinates.
- II) The electron density $n(\mathbf{r})$ that minimizes the energy functional $E_v[n]$ of the system is the correct ground state electron density,

$$E_0 \leq E_v[n], \quad (2.6)$$

where E_0 is the ground state total energy of the system and the energy functional is defined by

$$E_v[n] \equiv \int v(\mathbf{r})n(\mathbf{r})d\mathbf{r} + F[n], \quad (2.7)$$

where $F[n]$ is a universal functional of the electron density $n(\mathbf{r})$ and does not depend on an external potential $v(\mathbf{r})$.

The energy functional $E_v[n]$ in Eq. (2.7) can be obtained by variational method (Griffiths, 2005). If $F[n]$ is known, the ground state total energy could then be determined with a given external potential $v(\mathbf{r})$. However, it is quite complicated to determine the universal functional $F[n]$ that includes the kinetic energy and electron-electron interaction terms.

2.2.2 The Kohn-Sham Equations

To simplify the complicated Schrödinger equation of the many-electron system, Kohn and Sham (Kohn and Sham, 1965) have proposed a useful method based on the Hohenberg-Kohn theorems (Hohenberg and Kohn, 1964). In this method, the full interacting electrons system is mapped into the non-interacting electrons system, called the Kohn-Sham system, in which the same electronic density are obtained. The Kohn-Sham equation is defined by an effective potential, called the Kohn-Sham potential, in which the non-interacting electrons move. They showed that the energy functional $E_v[n]$ of the system can be written as

$$E_v[n] = \int v(\mathbf{r})n(\mathbf{r})d\mathbf{r} + \frac{1}{2} \iint \frac{n(\mathbf{r})n(\mathbf{r}')}{|\mathbf{r} - \mathbf{r}'|} d\mathbf{r}d\mathbf{r}' + G[n], \quad (2.8)$$

where the first term in Eq. (2.8) is the electron-ion Coulomb energy, the second term is the electron-electron Coulomb energy, and $G[n]$ is a universal functional of the electron density that includes the kinetic energy $T[n]$ of the non-interacting electrons system with density $n(\mathbf{r})$ and the exchange-correlation energy $E_{xc}[n]$ of the interacting system with density $n(\mathbf{r})$ which can be written as

$$G[n] = T[n] + E_{xc}[n]. \quad (2.9)$$

According to the stationary property of Eq. (2.8), that is

$$\int \delta n(\mathbf{r}) \left\{ v(\mathbf{r}) + \int \frac{n(\mathbf{r}')}{|\mathbf{r} - \mathbf{r}'|} d\mathbf{r}' + \frac{\delta T[n]}{\delta n(\mathbf{r})} + \mu_{xc}[n] \right\} d\mathbf{r} = 0, \quad (2.10)$$

where

$$\mu_{xc}[n] = \frac{\delta E_{xc}[n]}{\delta n(\mathbf{r})}. \quad (2.11)$$

Therefore, the effective (or Kohn-Sham) potential can be written as

$$v_{\text{eff}}(\mathbf{r}) = v(\mathbf{r}) + \int \frac{n(\mathbf{r}')}{|\mathbf{r} - \mathbf{r}'|} d\mathbf{r}' + \mu_{xc}[n], \quad (2.12)$$

and the kinetic energy can be written as the sum of the kinetic energy of the single particles,

$$T = \sum_{i=1}^N \int d\mathbf{r} \psi_i^*(\mathbf{r}) \left(-\frac{\hbar^2}{2m} \nabla^2 \right) \psi_i(\mathbf{r}). \quad (2.13)$$

Finally, the ground state properties of the system can be obtained by solving the Schrödinger equation for non-interacting particles moving in the effective potential $v_{\text{eff}}(\mathbf{r})$,

$$\left(-\frac{\hbar^2}{2m} \nabla^2 + v_{\text{eff}}(\mathbf{r}) \right) \psi_i(\mathbf{r}) = \varepsilon_i \psi_i(\mathbf{r}), \quad (2.14)$$

which is called the Kohn-Sham equation. The Eq. (2.14) shows that the complicated problem of the interacting electrons system is mapped onto the non-interacting electrons system moving in the effective potential, in which the exchange-correlation energy is included.

2.3 The Exchange-Correlation Energy Functional

The effective potential appeared in Eq. (2.12) contains the unknown exchange-correlation energy, $E_{xc}[n]$, term. In order to solve the Kohn-Sham equations in Eq. (2.14), the $E_{xc}[n]$ must be defined or approximated. Nowadays, there are several approximations proposed to define or calculate the $E_{xc}[n]$ term. The two most widely used approximations are the local density approximation (LDA) and the generalized gradient approximations (GGA). However, both LDA and GGA functionals lead to the well-known underestimation in band gap of many materials. Recently, Heyd, Scuseria, and Ernzerhof proposed the method to remedy the band gap problem occurred in LDA and GGA functionals by mixing between the Hartree-Fock exchange functional and another exchange-correlation functional such as GGA parameterized by Perdew, Burke, and Ernzerhof (GGA-PBE), called the HSE functional. Next, the details of each exchange-correlation will be provided.

2.3.1 The Local Density Approximation (LDA)

The LDA approximation is derived from the homogeneous electron gas (HEG) model. In this approximation, the inhomogeneous electron density can be locally treated as a homogeneous electron gas, of which the exchange-correlation energy ($E_{xc}^{LDA}[n]$) can be written as

$$E_{xc}^{LDA}[n] = \int \varepsilon_{xc}^{LDA}[n]n(\mathbf{r})d\mathbf{r} = \int (\varepsilon_x^{LDA}[n] + \varepsilon_c^{LDA}[n])n(\mathbf{r})d\mathbf{r}, \quad (2.15)$$

where $\varepsilon_{xc}^{LDA}[n]$ is the exchange-correlation energy per electron of a homogeneous electron gas, which can be separated into two terms, i.e., the exchange ($\varepsilon_x^{LDA}[n]$) and the correlation ($\varepsilon_c^{LDA}[n]$) energies.

For the exchange energy, it can be obtained from Dirac's expression (Dirac, 1930) by directly applying the HEG model as written below.

$$\varepsilon_X^{\text{LDA}}[n] = -\frac{3}{4} \left(\frac{3}{\pi} \right)^{1/3} n(\mathbf{r})^{1/3} = -\frac{3}{4} \left(\frac{9}{4\pi^2} \right)^{1/3} \frac{1}{r_s} = -\frac{0.4582}{r_s}, \quad (2.16)$$

where $r_s = \left(\frac{4}{3} \pi n \right)^{-1/3}$ is the Wigner-Seitz radius of an electron.

Regarding the correlation energy, there are only two density limits, which are known, i.e., low- and high-density limits, for the HEG model. The first approximation for the correlation energy was introduced by Wigner (Wigner, 1934) as

$$e_C^{\text{LDA}}[n] = -\frac{0.44}{r_s + 7.8}. \quad (2.17)$$

Later, Ceperley and Alder (Ceperley and Alder, 1980) performed more accurate quantum Monte Carlo simulations for intermediate values of the density. Now, the most widely LDA functional is introduced by Perdew and Zunger (Perdew and Zunger, 1981).

2.3.2 The Generalized Gradient Approximation (GGA)

Although LDA functional provides very good descriptions for the equilibrium atomic structure, elastic, and vibrational properties of many materials, it always gives an overestimation in the binding energy. Later, the improvement of the LDA functional is done by including the gradient of the electron gas into the exchange-correlation energy, known as GGA functional. In the GGA functional, the exchange-correlation energy can be written as

$$E_{\text{XC}}^{\text{GGA}}[n] = \int \varepsilon_{\text{XC}}^{\text{GGA}}[n, \nabla n] n(\mathbf{r}) d\mathbf{r}, \quad (2.18)$$

where $\varepsilon_{\text{xc}}^{\text{GGA}}[n, \nabla n]$ is the exchange-correlation energy per electron that is still local but also take the gradient of the electron density at the same coordinate into calculation.

Although the GGA functional tends to improve the binding energy over LDA functional, it sometime overestimates some physical properties. There are many forms to determine the exchange-correlation functional for GGA functional. The widely used GGA functional are PW91 functional proposed by Perdew and Wang (Perdew and Wang, 1992) and PBE functional proposed by Perdew, Burke, and Enzerhof (Perdew et al., 1996).

2.3.3 The Hybrid Functional

Although the LDA and GGA functionals give very good descriptions of many physical properties in materials, both of them lead to the well-known underestimation in the band gap for semiconductor and insulator (Lany and Zunger, 2008; Perdew, 1985). The hybrid functional was first introduced by Becke (Becke, 1993) to remedy the band gap problem. In the hybrid functional, some portion of exact exchange energy from Hartree-Fock theory is combined with the exchange-correlation energy from the other functional. This method provides an improvement for the band gap in semiconductor and insulator.

The Hartree-Fock exchange energy can be written as

$$E_{\text{x}}^{\text{HF}} = -\frac{1}{2} \sum_{i,j} \iint d\mathbf{r} d\mathbf{r}' \frac{\psi_i^*(\mathbf{r})\psi_j^*(\mathbf{r}')\psi_i(\mathbf{r})\psi_j(\mathbf{r}')}{|\mathbf{r}-\mathbf{r}'|}, \quad (2.19)$$

where $\psi_i(\mathbf{r})$ and $\psi_j(\mathbf{r}')$ are the set of one-electron eigenstate of the system. The sums over i and j run over all k -points that chosen to sample the Brillouin zone (BZ).

In the hybrid functional, some portion of the Hartree-Fock exchange energy in Eq. (2.19) is mixed with the other exchange-correlation functional to construct the full exchange-correlation functional. There are many types of hybrid functional, such as B3LYP proposed by Becke and Lee (Becke, 1993; Lee et al., 1988), PBE0 proposed by Adamo and Barone (Adamo and Barone, 1999), and HSE03/HSE06 proposed by Heyd, Scuseria, and Ernzerhof (Heyd et al., 2003). The HSE06 functional was used to improve some calculated results in this thesis.

In the HSE03/HSE06 functionals, a screened Coulomb potential is applied to the exchange interaction. The exact exchange functional is divided into two components, i.e., short-range (SR) and long-range (LR), with the screening parameter (ω). Normally, $\omega = 0.3 \text{ \AA}^{-1}$ refers to HSE03 functional, while $\omega = 0.2 \text{ \AA}^{-1}$ refers to HSE06 functional. The Hartree-Fock exchange energy will be mixed with the GGA-PBE functional only in the SR component as shown below,

$$E_{XC}^{\text{HSE06}} = \alpha E_X^{\text{HF,SR}}(\omega) + (1-\alpha)E_X^{\text{PBE,SR}}(\omega) + E_X^{\text{PBE,LR}}(\omega) + E_C^{\text{PBE}}, \quad (2.20)$$

where α is the mixing parameter. The HSE06 functional is equivalent to PBE0 functional when $\omega = 0$, i.e., the LR component becomes zero, and equivalent to pure GGA-PBE functional when $\omega \rightarrow \infty$, i.e., the SR component becomes zero.

2.4 Bloch's Theorem and Plane Wave Basis Sets

In Bloch's theorem, the wave functions of an electron in a crystal can be written as (Kittel, 2004)

$$\psi_{\mathbf{k}}(\mathbf{r}) = u_{\mathbf{k}}(\mathbf{r})e^{i\mathbf{k}\cdot\mathbf{r}}, \quad (2.21)$$

where $u_{\mathbf{k}}(\mathbf{r})$ has the same periodicity as the crystal, i.e., $u_{\mathbf{k}}(\mathbf{r}) = u_{\mathbf{k}}(\mathbf{r} + \mathbf{a})$, \mathbf{a} is the primitive lattice vector of the system, and \mathbf{k} is a wave vector confined to the first Brillouin zone. Due to the periodicity of $u_{\mathbf{k}}(\mathbf{r})$, it can be expanded in a Fourier series, i.e.,

$$u_{\mathbf{k}}(\mathbf{r}) = \sum_{\mathbf{G}} C_{\mathbf{k},\mathbf{G}} e^{i\mathbf{G}\cdot\mathbf{r}}, \quad (2.22)$$

where \mathbf{G} is the reciprocal lattice vector and $C_{\mathbf{k},\mathbf{G}}$ is the Fourier coefficient. Then, the Eq. (2.21) can be rewritten as

$$\psi_{\mathbf{k}}(\mathbf{r}) = \sum_{\mathbf{G}} C_{\mathbf{k}+\mathbf{G}} e^{i(\mathbf{k}+\mathbf{G})\cdot\mathbf{r}}. \quad (2.23)$$

Bloch's theorem states that the wave function of an electron in a periodic system can be described by the product of a periodic function and a plane wave. In principle, an infinite numbers of plane wave are required to construct the actual wave function. However, in practice, too many numbers of plane waves require high computational demand. In the calculation, the numbers of plane wave are limited by the plane wave energy cutoff (E_{cut}), i.e.,

$$\frac{\hbar^2}{2m} |\mathbf{k} + \mathbf{G}|^2 < E_{\text{cut}}. \quad (2.24)$$

2.5 K -points Sampling and Special k -points

In real space, the Wigner-Seitz cell is the enclosed area, which has the smallest volume. This area can be determined by drawing the lines from the chosen lattice point to the neighboring lattice points. Then, at the midpoint of each line, another lines are drawn normal to each of the first set of lines. The area enclosed by the second set of lines is call Wigner-Seitz cell (see text book for more details

(Martin, 2004)). In reciprocal space, the same process used to construct Wigner-Seitz will create smallest cell in reciprocal space, which is called the first Brillouin zone. Many physical properties of a crystal can be obtained by considering only the wave function in the first Brillouin zone because the wave functions outside the first zone will be brought back to the first zone by any reciprocal lattice vectors \mathbf{G} of a crystal. However, the summation over k -points in Eq. (2.23) has an infinite number, which is impossible for calculation. Some approaches for k -points sampling in the first Brillouin zone are proposed to calculate the electronic states at sampled k -points and interpolate them between those calculated k -points, such as Chadi-Cohen (Chadi and Cohen, 1973) and Monkhorst-Pack schemes (Monkhorst and Pack, 1976). These approaches allow us to reduce the number of k -points sampling from infinite to finite number.

2.6 Pseudopotential and Projector Augmented-Wave Method

In general, the electrons in each atom can be separate into two groups, i.e., valence and core electrons. While valence electrons are the electrons in the outermost shell that participates in the formation of chemical bonding with other atoms, core electrons are the electrons in the inner shell that are strongly bound with the nucleus and do not participate in the formation of chemical bonding. In addition, an oscillation of the wave function in the core region is quite rapid. This makes the calculation requiring a lot of the Fourier components to construct the wave function in this region. However, many physical properties of materials mostly depend on the valence electrons. Therefore, the wave function in the core region will be replaced by

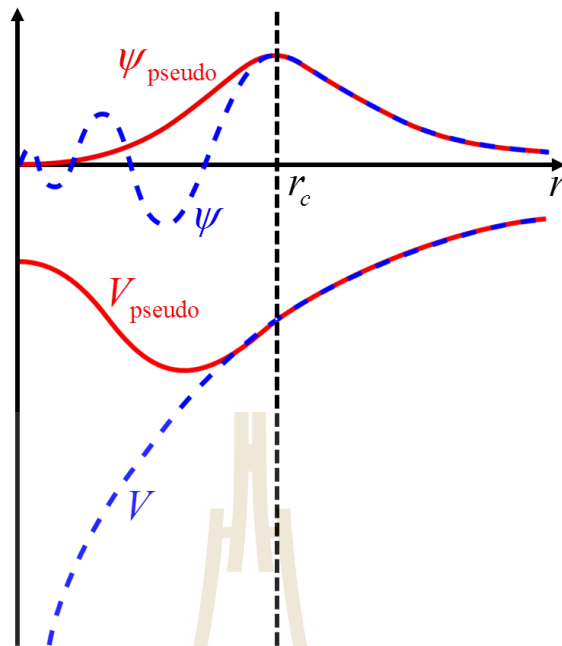


Figure 2.1 The illustrations of the pseudo wave function and pseudopotential. The dash blue lines represent the real wave function (ψ) and real Coulomb potential (V). The solid red lines represent the corresponding pseudo wave function (ψ_{pseudo}) and pseudopotential (V_{pseudo}). The cutoff radius (r_c) marked by the vertical dash line represents the boundary at which the real quantities become identical with pseudo quantities. This figure is reproduced from Ref. (Wolfram, 2006).

a smooth wave function to reduce the computational demanding. This method is called the pseudopotential approximation firstly introduced by Hellmann (Hellmann, 1935). Figure 2.1 illustrates the pseudopotential and pseudo wave function compared to the Coulombic potential and real wave function, respectively.

Later, the projector augmented-wave (PAW) method is one of the popular methods adopted from the pseudopotential proposed by Blöchl (Blöchl, 1994; Kresse and Joubert, 1999). In the PAW method, the rapidly oscillating all-electron wave

function (ψ) is derived from the smooth (pseudo) wave functions ($\tilde{\psi}$) through the transformation operator (τ):

$$|\psi\rangle = \tau|\tilde{\psi}\rangle, \quad (2.25)$$

where the transformation operator (τ) can be written as

$$\tau = 1 + \sum_i (|\psi_i\rangle - |\tilde{\psi}_i\rangle)\langle p_i|, \quad (2.26)$$

where ψ_i is a set of all-electron partial waves, $\tilde{\psi}_i$ is a set of pseudo partial waves, and p_i is a set of projector functions. The pseudo partial waves $\tilde{\psi}_i$ are equivalent to the all-electron partial waves ψ_i outside the cutoff radius (r_c). Normally, the cutoff radius r_c enclosing the atom is chosen around the half of the nearest-neighboring distance (Kresse and Joubert, 1999).

2.7 The Hellmann-Feynman Theorem

Hellmann (Hellmann, 1937) and Feynman (Feynman, 1939) have independently proposed the theorem to show that the derivative of the total energy with respect to a parameter can be obtained from the expectation value of the derivative of the Hamiltonian with respect to the same parameter, i.e.,

$$\begin{aligned}
\frac{\partial E}{\partial \lambda} &= \frac{\partial}{\partial \lambda} \langle \psi | \hat{H} | \psi \rangle \\
&= \left\langle \frac{\partial \psi}{\partial \lambda} | \hat{H} | \psi \right\rangle + \left\langle \psi | \hat{H} | \frac{\partial \psi}{\partial \lambda} \right\rangle + \left\langle \psi | \frac{\partial \hat{H}}{\partial \lambda} | \psi \right\rangle \\
&= E \left\langle \frac{\partial \psi}{\partial \lambda} | \psi \right\rangle + E \left\langle \psi | \frac{\partial \psi}{\partial \lambda} \right\rangle + \left\langle \psi | \frac{\partial \hat{H}}{\partial \lambda} | \psi \right\rangle . \tag{2.27} \\
&= E \frac{\partial}{\partial \lambda} \langle \psi | \psi \rangle + \left\langle \psi | \frac{\partial \hat{H}}{\partial \lambda} | \psi \right\rangle \\
&= \left\langle \psi | \frac{\partial \hat{H}}{\partial \lambda} | \psi \right\rangle
\end{aligned}$$

The Hellmann-Feynman theorem is mostly used to calculate the forces acting on nuclei, called the Hellmann-Feynman forces, when the parameters are the nuclei positions.

2.8 Electronic Ground State Calculation with Vienna *Ab Initio* Simulation Package (VASP)

To determine the electronic ground state of the system, the Kohn-Sham equation of the system need to be solved, which can be performed by several codes. In this thesis, the Vienna *Ab initio* Simulation Package (VASP) developed by Kresse, Hafner, and Furthmüller was carried out for all simulations. Most of the algorithms implemented in VASP codes use an iterative matrix-diagonalization scheme based on the conjugate gradient scheme, block Davidson scheme, or a residual minimization scheme-direct inversion in the iterative subspace (RMM-DIIS). An efficient Broyden/Pulay mixing scheme is used to mix the charge density. The interaction between ions and electrons is described by the projector-augmented wave (PAW) method and a plane wave basis set is used to construct the wave function. During the

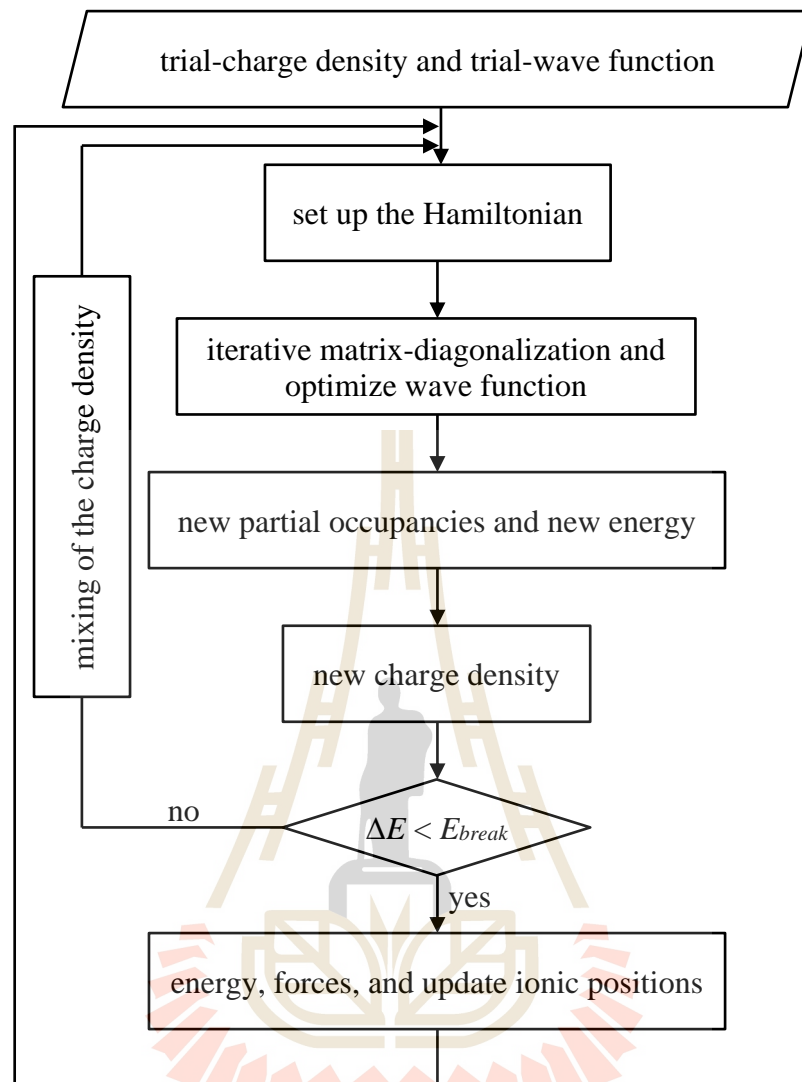


Figure 2.2 The self-consistent scheme used in VASP codes to calculate the electronic ground state total energy and wave function of the system.

calculation, the forces acting on each atom can be calculated through the Hellmann-Feynman theorem and these will be used to relax atoms into their equilibrium positions. The computational scheme used in VASP codes is illustrated in Figure 2.2. More details of VASP codes can be found in the VASP manual (Kresse et al., 2015).

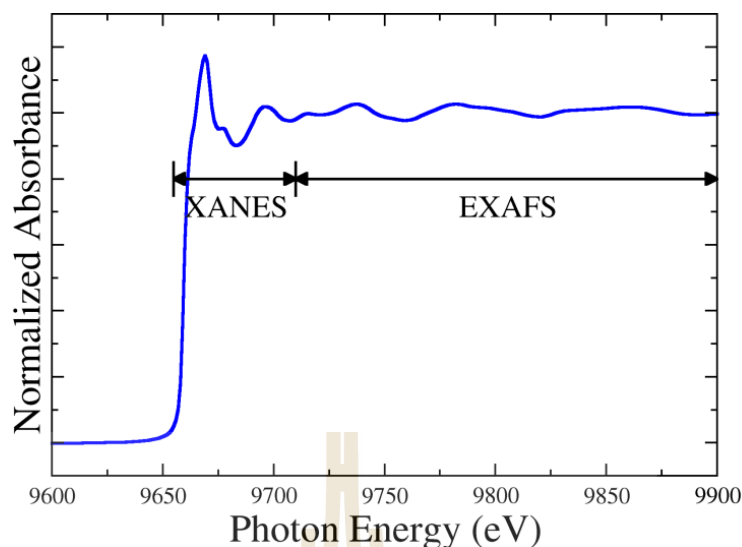


Figure 2.3 The measured Zn *K*-edge XAS spectrum of Zn foil. The XANES and EXAFS regions are indicated. The data obtained from Ref. (Ravel and Newville, 2005).

2.9 Theory of X-ray Absorption Spectroscopy

The x-ray absorption spectroscopy (XAS) technique is a powerful tool for identifying the local structures of any interested atoms or defects in materials. This is because this technique is an element selective by tuning incoming x-ray energy to the threshold energy of the measured element making it requiring a tunable x-ray energy source to scan the x-ray energy at the interested region. This technique can be performed at beamline no-8 of Synchrotron light Research Institute (SLRI), Thailand.

For XAS technique, the x-ray energy was scanned from the energy a bit lower than the threshold energy of selected element to the higher energy to obtain the XAS spectrum. In this process, the electrons at the core-level will be excited to the unoccupied states above Fermi-level by absorbing appropriate x-ray energy. In XAS spectrum, it can be divided into two regions as shown in Figure 2.3: (1) low energy

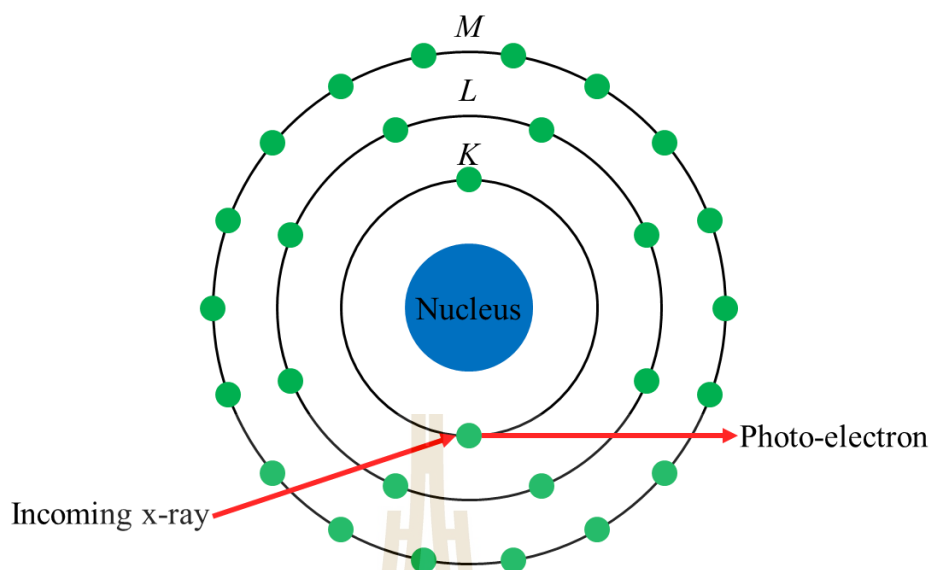


Figure 2.4 The illustration of electrons in the core levels. The electron in the *K*-shell can be excited to higher unoccupied state by absorbing incoming x-ray energy, which is equal or greater than the binding energy of that electron creating the photoelectron. *K*, *L*, and *M* indicate the absorption edges.

region called the x-ray absorption near-edge structure (XANES) and (2) high energy region called the extended x-ray absorption fine structure (EXAFS). While XANES spectrum usually covers around 50 – 100 eV above the absorption edge, the EXAFS spectrum can be extended to 500 eV above the absorption edge. The great usefulness of this technique is the elemental specificity since each element has different absorption edge. XANES can be used to determine the oxidation state and coordination environment of the interested element in the sample, while EXAFS can be used to determine the coordination number, disorder and radial distance of neighboring atoms.

The fundamental theory of XAS technique is based on the photoelectric effect. The core electron can be excited to a higher unoccupied energy state creating the

photoelectron (see Figure 2.4) by absorbing energy from the incident x-ray, which has energy equal or greater than the binding energy of core electron. XAS technique is the measurement of the x-ray absorption coefficient as a function of energy, $\mu(E)$, which must be satisfied Beer's law,

$$I = I_0 e^{-\mu d}, \quad (2.28)$$

where I_0 and I are the intensity of the incident and outgoing x-ray, respectively, and d is the thickness of the sample.

In Chapter IV, the comparison of XANES spectra, between the experiment and simulation, will be shown to determine the local structure of Mg in $\text{Mg}_x\text{Zn}_{1-x}\text{O}$ alloy. In the simulation, the crystal structures were firstly optimized by using VASP code and then the optimized structures were used to simulate the XANES spectrum by using FEFF codes (Ankudinov et al., 1998; Rehr et al., 2009).

2.10 References

- Adamo, C. and Barone, V. (1999). Toward reliable density functional methods without adjustable parameters: The PBE0 model. **The Journal of Chemical Physics** 110: 6158.
- Ankudinov, A. L., Ravel, B., Rehr, J. J., and Conradson, S. D. (1998). Real-space multiple-scattering calculation and interpretation of x-ray-absorption near-edge structure. **Physical Review B** 58: 7565.
- Becke, A. D. (1993a). Density-functional thermochemistry. III. The role of exact exchange. **The Journal of Chemical Physics** 98: 5648.
- Becke, A. D. (1993b). A new mixing of Hartree–Fock and local density-functional theories. **The Journal of Chemical Physics** 98: 1372.

- Blöchl, P. E. (1994). Projector augmented-wave method. **Physical Review B** 50: 17953.
- Born, M. and Oppenheimer, R. (1927). Zur quantentheorie der molekeln. **Annalen der Physik** 389: 457.
- Ceperley, D. M. and Alder, B. J. (1980). Ground state of the electron gas by a stochastic method. **Physical Review Letters** 45: 566.
- Chadi, D. J. and Cohen, M. L. (1973). Special points in the Brillouin zone. **Physical Review B** 8: 5747.
- Dirac, P. A. M. (1930). Note on exchange phenomena in the Thomas atom. **Mathematical Proceedings of the Cambridge Philosophical Society** 26: 376.
- Fermi, E. (1911). Statistical method to determine some properties of atoms. **Rendiconti Lincei-Scienze Fisiche E Naturali** 22: 283.
- Feynman, R. P. (1939). Forces in molecules. **Physical Review** 56: 340.
- Fock, V. (1930). Näherungsmethode zur lösung des quantenmechanischen mehrkörperproblems. **Zeitschrift für Physik** 61: 126.
- Griffiths, D. J. (2005). **Introduction to Quantum Mechanics**. Pearson Prentice Hall.
- Hartree, D. R. (1928). The wave mechanics of an atom with a non-Coulomb central field. Part I. Theory and methods. **Mathematical Proceedings of the Cambridge Philosophical Society** 24: 89.
- Hellmann, H. (1935). A new approximation method in the problem of many electrons. **The Journal of Chemical Physics** 3: 61.
- Hellmann, H. (1937). **Einführung in die Quantenchemie**. Franz Deuticke.

- Heyd, J., Scuseria, G. E., and Ernzerhof, M. (2003). Hybrid functionals based on a screened Coulomb potential. **The Journal of Chemical Physics** 118: 8207.
- Hohenberg, P. and Kohn, W. (1964). Inhomogeneous electron gas. **Physical Review** 136: B864.
- Kittel, C. (2004). **Introduction to Solid State Physics**. Wiley.
- Kohn, W. and Sham, L. J. (1965). Self-consistent equations including exchange and correlation effects. **Physical Review** 140: A1133.
- Kresse, G. and Joubert, D. (1999). From ultrasoft pseudopotentials to the projector augmented-wave method. **Physical Review B** 59: 1758.
- Kresse, G., Marsman, M., and Furthmüller, J. (2015). **Vienna *Ab-initio* Simulation Package: VASP the GUIDE**. Computational Materials Physics, Faculty of Physics, Universitat Wien, Sensengasse 8/12, A-1090 Wien, Austria.
- Lany, S. and Zunger, A. (2008). Assessment of correction methods for the band-gap problem and for finite-size effects in supercell defect calculations: Case studies for ZnO and GaAs. **Physical Review B** 78: 235104.
- Lee, C., Yang, W., and Parr, R. G. (1988). Development of the Colle-Salvetti correlation-energy formula into a functional of the electron density. **Physical Review B** 37: 785.
- Martin, R. M. (2004). **Electronic Structure: Basic Theory and Practical Methods**. Cambridge University Press.
- Monkhorst, H. J. and Pack, J. D. (1976). Special points for Brillouin-zone integrations. **Physical Review B** 13: 5188.
- Perdew, J. P. (1985). Density functional theory and the band gap problem. **International Journal of Quantum Chemistry** 28: 497.

- Perdew, J. P., Burke, K., and Ernzerhof, M. (1996). Generalized gradient approximation made simple. **Physical Review Letters** 77: 3865.
- Perdew, J. P. and Wang, Y. (1992). Accurate and simple analytic representation of the electron-gas correlation energy. **Physical Review B** 45: 13244.
- Perdew, J. P. and Zunger, A. (1981). Self-interaction correction to density-functional approximations for many-electron systems. **Physical Review B** 23: 5048.
- Ravel, B. and Newville, M. (2005). ATHENA, ARTEMIS, HEPHAESTUS: data analysis for x-ray absorption spectroscopy using IFEFFIT. **Journal of Synchrotron Radiation** 12: 537.
- Rehr, J. J., Kas, J. J., Prange, M. P., Sorini, A. P., Takimoto, Y., and Vila, F. (2009). Ab initio theory and calculations of x-ray spectra. **Comptes Rendus Physique** 10: 548.
- Thomas, L. H. (1927). The calculation of atomic fields. **Mathematical Proceedings of the Cambridge Philosophical Society** 23: 542.
- Wigner, E. (1934). On the interaction of electrons in metals. **Physical Review** 46: 1002.
- Wolfram, Q. (2006). **Pseudopotential** [On-line]. Available: https://upload.wikimedia.org/wikipedia/commons/f/fb/Sketch_Pseudopotential_s.png.

CHAPTER III

NITROGEN AND OXYGEN SUBSTITUTIONAL DEFECTS IN SELECTED METAL OXIDES AND METAL NITRIDES

3.1 Introduction

Binary metal-oxides/nitrides have attracted great attention due to their excellent optical and electrical properties, making them suitable for a wide range of technological applications (Nicollian and Brews, 1982; Piprek, 2007). For metal oxides, the alkali metal (group I) oxides, M_2O ($M = \text{Li, Na, K, and Rb}$), play a crucial role in solid state batteries because of their high ionic conductivity (Moakafi et al., 2008). The alkaline earth metal (group II) oxides, MO ($M = \text{Be, Mg, Ca, and Sr}$), are important materials for photocatalytic applications because the band gap of these oxides cover a wide range of spectral regions ranging from blue to ultraviolet regions (Pandey et al., 1991). The group III oxides, M_2O_3 ($M = \text{Al, Ga, and In}$), are also the promising materials for being used as transparent conducting oxides applications (Liu et al., 2010).

Regarding metal nitrides, for group I nitride, Li_3N is the only one structure, which is stable at room temperature and room pressure (Cui et al., 2009), and it is widely used as high-performance reversible hydrogen storage material in hydrogen energy system because of its high hydrogen absorption and desorption capacities

(Ichikawa et al., 2004). For group II nitrides, M_3N_2 ($M = \text{Be, Mg, Ca, and Sr}$), they are widely applied in many applications, for instance Be_3N_2 is as a device for the improvement of extreme ultraviolet to soft x-ray region (de la Cruz et al., 2004) and Mg_3N_2 as well as Ca_3N_2 catalysts are used for preparing a cubic phase of boron nitride (Heyns et al., 1998). Lastly, the group III nitrides, MN ($M = \text{Al, Ga, and In}$), they are extensively applied for light emission device because the band gaps of these materials cover a wide range of wavelengths ranging from green to ultraviolet regions (Walle and Neugebauer, 2004).

In general, several physical properties of materials are mainly controlled by the existence of native defects or impurities, which are intentionally or unintentionally created during the crystal growth processes. For example, some as-grown metal-oxides/nitrides always exhibit unintentional n -type conductivity, of which the cause is proposed to be due to the creation of nitrogen vacancy (V_N) for metal nitrides (Boguslawski et al., 1995) and oxygen vacancy (V_O) for metal oxides (Ágoston et al., 2009). In addition, hydrogen impurity is also suggested to be the cause of the observed n -type conductivity in metal-oxides/nitrides (Shi et al., 2004; Van de Walle, 2000). To obtain high purity materials, the equipment and techniques used to synthesize these materials are then carefully considered to prevent the formation of unintentional defects or impurities in materials. Nevertheless, N and O atoms are the two most abundant compositions in the air (78.08% and 20.95% by volume for N and O, respectively) (Brimblecombe, 1995), therefore, they can easily incorporate into metal-oxides/nitrides affecting the physical properties of materials. Since the atomic sizes of N and O are comparable, i.e., 0.65 Å and 0.60 Å for N and O, respectively (Slater, 1964), N atom is then likely to substitute for O sites in metal oxides forming

N_O defect. Similarly, O atom has a chance to substitute for N sites in metal nitrides forming O_N defect. The existence of these unintentional defects can affect some physical properties of metal-oxides/nitrides. However, there is still limited information on the comparative properties of N_O and O_N defects among different metal-oxides/nitrides. The understanding of physical properties related to these defects in metal-oxides/nitrides is deemed crucial for controlling and improving material properties into desired ways. In this work, N_O and O_N defects in various metal oxides and metal nitrides, respectively, were systematically studied by using first-principles calculations based on DFT to investigate the relation of these defects in different metal-oxides/nitrides.

3.2 Computational Details

In this work, first-principles calculations based on DFT within a plane-wave basis set as implemented in VASP code (Kresse and Furthmüller, 1996; Kresse and Hafner, 1994; Kresse and Joubert, 1999) were carried out. For the exchange-correlation energy, the two most common approximations, i.e., the local density approximation (LDA) (Perdew and Zunger, 1981) and the generalized gradient approximation (GGA) (Perdew and Wang, 1992), were used to investigate N_O and O_N defects in metal oxides and metal nitrides, respectively. The electron-ion interactions were described by the projector augmented wave (PAW) method (Blöchl, 1994). The energy cutoff for expanding the plane-wave basis set was set at 500 eV. All atoms in each system were fully allowed to relax until the residue forces acting on each atom became less than 0.01 eV/Å. More calculation details can be found in Chapter II.

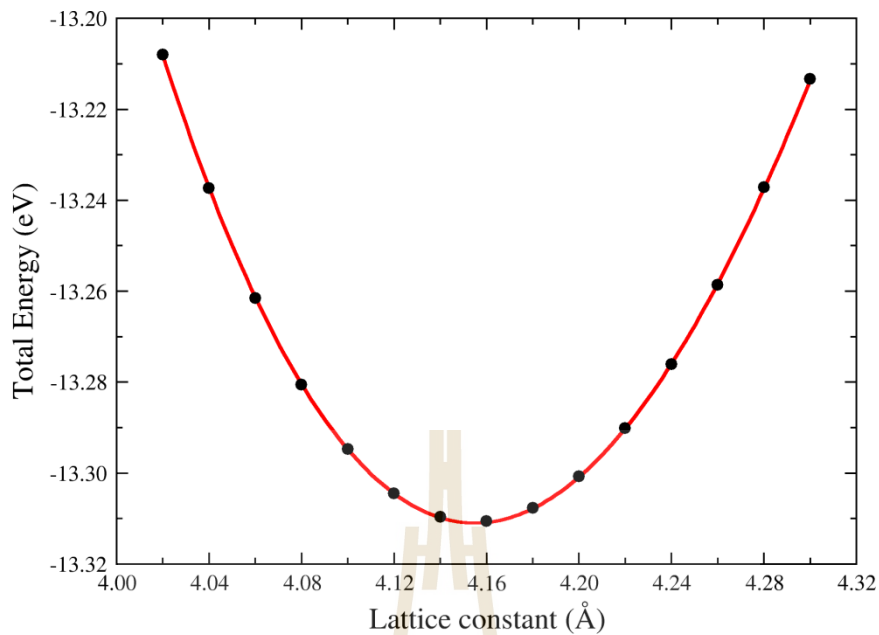


Figure 3.1 The calculated total energy of rocksalt-MgO as a function of lattice constant for determining the equilibrium lattice constant. The black dots and red line represent the calculated and fit data, respectively.

3.2.1 Structural relaxations

In this research, the most stable phases of metal-oxides/nitrides at room temperature and pressure were chosen in this study. Each crystal structure was then optimized to determine the lattice parameters and their shapes by calculating the total energy at different lattice parameters. Then, the energy vs. lattice constant curve was plot and fitted with the 3rd polynomial to find the equilibrium lattice constants. Figure 3.1 illustrates the energy vs. lattice constant curve for rocksalt-MgO as an example.

The stability of each metal-oxides/nitride can be determined from the heat of formation (ΔH_f) which is defined by

$$\Delta H_f[A_xB_y] = E_{\text{tot}}[A_xB_y] - xE_{\text{tot}}[A] - yE_{\text{tot}}[B], \quad (3.1)$$

where $E_{\text{tot}}[A_xB_y]$ is the total energy per formula unit of compound A_xB_y , $E_{\text{tot}}[A]$ and $E_{\text{tot}}[B]$ are the total energy per atom of A (metal) and B (N or O) elements. The negative value implies that the compound is stable.

3.2.2 Defect formation energy calculations

For defect calculations, including N_O defect in metal oxides and O_N defect in metal nitrides, a supercell approach (Payne et al., 1992) with at least 64-atom supercell was performed to reduce the defect-defect interactions arising from the neighboring cells due to the periodic boundary condition.

Under thermodynamic equilibrium, the defect concentration (c) in a crystal can be determined by

$$c = N_{\text{sites}} \exp\left(-\frac{E^f}{k_B T}\right), \quad (3.2)$$

where N_{sites} is the number of sites, on which the defect can be incorporated, E^f is the defect formation energy, k_B is the Boltzmann's constant, and T is the temperature. Eq. (3.2) demonstrates that the lower the defect formation energy, the higher the defect concentration can be obtained.

In principle, the possibility of defect formation in a crystal can be obtained from its formation energy, which is defined by (Walle and Neugebauer, 2004)

$$E^f [X^q] = E_{\text{tot}}[X^q] - E_{\text{tot}}[\text{bulk}] - \sum_i n_i \mu_i + q[E_F + E_{VBM} + \Delta V], \quad (3.3)$$

where $E_{\text{tot}}[X^q]$ is the total energy of a supercell with a defect X (where X is N_O or O_N defect) in charge state q , $E_{\text{tot}}[\text{bulk}]$ is the total energy of a defect-free supercell. n_i is the number of atoms species i (here i can be N or O) being removed from (the sign of

n_i is negative) or added to (the sign of n_i is positive) a supercell to create a defect X in charge state q with the corresponding atomic chemical potential μ_i , E_F is the Fermi energy or electron chemical potential referenced to the valence-band maximum (E_{VBM}), and ΔV is the correction term used to align the electrostatic potentials between bulk supercell and defect supercell at the point far away from the defect.

For example, the defect formation energy of N_O can be written as

$$E^f [N_O^q] = E_{\text{tot}} [N_O^q] - E_{\text{tot}} [\text{bulk}] + \mu_O - \mu_N + q[E_F + E_{VBM} + \Delta V], \quad (3.4)$$

and that of O_N defect is

$$E^f [O_N^q] = E_{\text{tot}} [O_N^q] - E_{\text{tot}} [\text{bulk}] + \mu_N - \mu_O + q[E_F + E_{VBM} + \Delta V]. \quad (3.5)$$

To grow a single crystal metal oxides (M_xO_y) or metal nitrides (M_xN_y) under thermodynamic equilibrium, the following conditions must be satisfied,

$$\mu_{M_xO_y} = x\mu_M + y\mu_O, \quad (3.6)$$

or

$$\mu_{M_xN_y} = x\mu_M + y\mu_N, \quad (3.7)$$

for metal oxides and metal nitrides, respectively. Where $\mu_{M_xO_y}$ and $\mu_{M_xN_y}$ is the total energy per formula unit of M_xO_y and M_xN_y compounds, respectively. To prevent the formation of undesired phases in a crystal, the upper limits for μ_M , μ_O , and μ_N are set to the energies per atom of metallic phases, gaseous O_2 ($\mu_O = \frac{1}{2}E_{\text{tot}}[O_2]$), and gaseous N_2 ($\mu_N = \frac{1}{2}E_{\text{tot}}[N_2]$), respectively. In practice, the defect formation energy is a function of chemical potentials as well as Fermi level as shown in Eq. (3.3). The defect formation energy can be plotted as a function of E_F under two extreme

conditions: (1) metal-rich growth condition and (2) metal-poor growth condition. The defect formation energy under other growth conditions can be interpolated from these two extreme conditions. For metal-rich growth condition, $\mu_M = E_{\text{tot}}(\text{metal})$, $\mu_O = \frac{1}{y}[\mu_{M_xO_y} - x\mu_M]$, and $\mu_N = \frac{1}{y}[\mu_{M_xN_y} - x\mu_M]$ were set. Regarding metal-poor growth condition, $\mu_O = \frac{1}{2}E_{\text{tot}}[\text{O}_2]$ and $\mu_N = \frac{1}{2}E_{\text{tot}}[\text{N}_2]$ were set; then μ_M can be determined from Eq. (3.6) and (3.7). For N_O defect in metal oxides, N_2 , NO_3 , $M_x\text{N}_y$, and $M_x\text{N}_y\text{O}_z$ phases were needed to take into consideration to prevent the formation of undesired phases. Regarding O_N defect in metal nitrides, μ_O is determined from $M_x\text{O}_y$ phase for both metal-rich and metal-poor growth conditions.

3.2.3 Defect transition levels

In practice, N_O and O_N defects in metal oxides and metal nitrides, respectively, could be stable in different charge states depending on the Fermi level position. This leads to the creation of extra energy level lying within the band gap; affecting the electrical and optical properties of metal-oxides/nitrides. However, N and O are non-isovalent atom, i.e., N atom has one valence electron less than O atom. Therefore, N_O defect in metal oxides could be stable in either negative charge state ($q = -1$) or neutral charge state ($q = 0$). In opposite, O_N defect in metal nitrides could be stable in either positive charge state ($q = +1$) or neutral charge state. The extra energy level created by the defect is called defect transition level or thermodynamic transition level. This energy level is defined as the Fermi level position, at which the formation energies of the defect in two different charge states are equal (Walle and

Neugebauer, 2004). For N_O defect in metal oxides, the defect transition level can be determined from

$$\varepsilon(0/-) = E_{\text{tot}}[N_O^-] - E_{\text{tot}}[N_O^0] - E_v - \Delta V . \quad (3.9)$$

Similarly, for O_N defect in metal nitrides,

$$\varepsilon(+/0) = E_{\text{tot}}[O_N^0] - E_{\text{tot}}[O_N^+] - E_v - \Delta V . \quad (3.10)$$

3.2.4 Band alignment calculations

The calculated electronic structures, including the VBM, conduction band minimum (CBM), and defect transition level, obtained from different metal oxides/nitrides as well as different XC-functional cannot be directly compared to each other because each calculation is referenced to their own atomic energies. In order to compare those levels obtained from different calculations, further calculations were needed to make such levels comparable. There are a few approaches used to align such levels obtained from different calculations, for instance simulating the heterointerfaces of two materials to find the valence band and conduction band offsets (Van de Walle and Martin, 1987), using the defect transition level of hydrogen as a common reference (Van de Walle and Neugebauer, 2003), and aligning the valence band and conduction band positions with respect to the vacuum level (Grüneis et al., 2014). In this research, the latter was used to align the VBM and CBM obtained from different compounds as well as different functionals with respect to the vacuum level by performing the surface calculations to find the difference between the average local electrostatic potential in bulk-like region and that in vacuum region (Moses et al., 2011). By combining surface and bulk calculations, such levels obtained from different compounds and functionals are comparable. This approach is so-called “band alignment”.

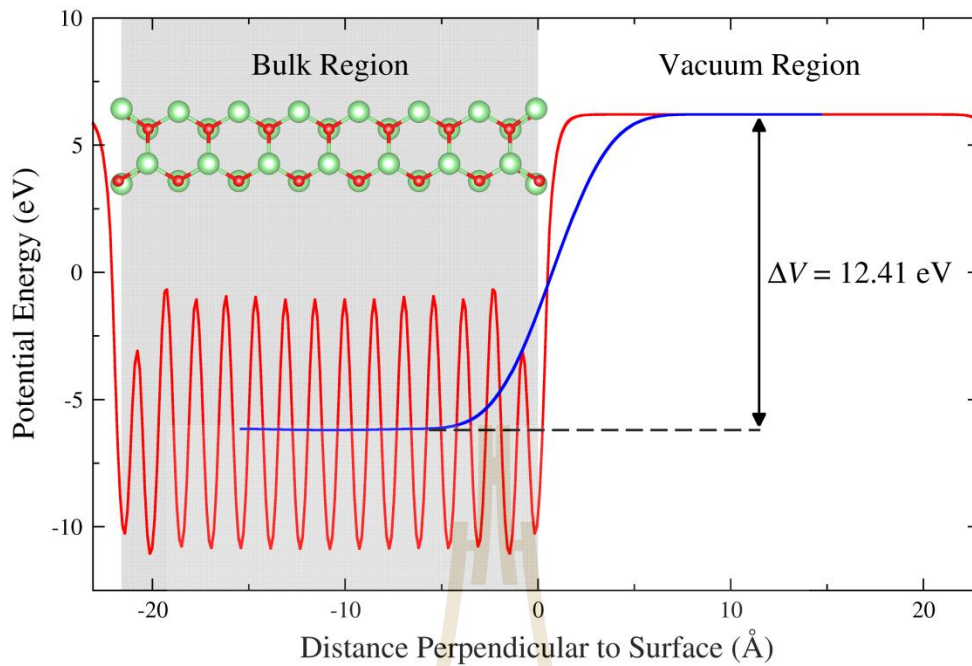


Figure 3.2 The illustration of the surface calculations for determining the electrostatic potential different between bulk-like and vacuum regions in wurtzite-AlN. The green and red balls represent Al and N atoms, respectively. The planar and macroscopic averages of the electrostatic potential are showed in red and blue lines, respectively.

The band alignment calculations consist of two main separate procedures: (i) a bulk calculation to determine the VBM and CBM positions for each compound and (ii) a surface calculation to find the difference between the local electrostatic potential in the bulk-like and vacuum regions. In the surface calculations, a slab model was performed by constructing the non-polar surface of chosen compound separated by the vacuum region. The atoms in the outermost at least three layers were fully allowed to relax while the remaining atoms were kept fixed to represent the bulk-like region. Then, the local electrostatic potential at every point in the cell were calculated to determine the planar average in the direction

parallel to the surface. After that, the macroscopic average is obtained by averaging the planar average potential over the entire cell along the direction perpendicular to the surface. Figure 3.2 illustrates planar and macroscopic average potentials for the wurtzite-AlN as an example.

3.3 Results and Discussion

3.3.1 Bulk Properties

The calculated lattice parameters of all selected metal oxides and metal nitrides obtained from LDA and GGA functionals were tabulated in Table 3.1 and 3.2 for metal oxides and metal nitrides, respectively, along with the corresponding experimental lattice parameters. It is clearly seen that the LDA functional give the lattice parameters a bit lower than the experimental values. In opposite, the calculated results with GGA functional are a bit higher than the experimental values. The differences between the calculated and experimental values are less than 4% as shown in the parenthesis in Table 3.1 and 3.2. Consequently, both LDA and GGA functionals seem to be sufficiently describe the crystal structures of these compounds. Note that the crystal structures of selected metal-oxides/nitrides are demonstrated in Appendix A.

Figure 3.3 demonstrates the calculated heat of formation of the selected metal-oxides/nitrides accompanying with the corresponding experimental values. The results reveal that the calculated heat of formations obtained from LDA functional are again lower than that obtained from the GGA calculations for both metal-oxides/nitrides. Regarding metal oxides, LDA functional seems to provide better heat of formations than GGA functional when comparing with the experimental

Table 3.1 The calculated lattice parameters of selected metal oxides with LDA and GGA functionals accompanying with the corresponding experimental values. The values in the parenthesis represent the percentage error between the calculated and the experimental values.

Compound	Structure	Lattice parameters (Å)		
		LDA	GGA	Expt.
Group I oxide				
Li ₂ O	Antifluorite	$a = 4.51$ (-2.38%)	$a = 4.64$ (+0.43%)	$a = 4.62^a$
Na ₂ O	Antifluorite	$a = 5.37$ (-3.42%)	$a = 5.57$ (+0.18%)	$a = 5.56^a$
K ₂ O	Antifluorite	$a = 6.19$ (-4.03%)	$a = 6.47$ (+0.31%)	$a = 6.45^a$
Rb ₂ O	Antifluorite	$a = 6.55$ (-2.82%)	$a = 6.86$ (+1.78%)	$a = 6.74^b$
Group II oxide				
BeO	Wurtzite	$a = 2.66$ (-1.48%)	$a = 2.71$ (+0.37%)	$a = 2.70$
		$c = 4.33$ (-0.92%)	$c = 4.41$ (+0.92%)	$c = 4.37^c$
MgO	Rocksalt	$a = 4.15$ (-1.43%)	$a = 4.24$ (+0.71%)	$a = 4.21^d$
CaO	Rocksalt	$a = 4.72$ (-1.67%)	$a = 4.84$ (+0.83%)	$a = 4.80^d$
SrO	Rocksalt	$a = 5.08$ (-1.55%)	$a = 5.20$ (+0.78%)	$a = 5.16^e$

^a (Sommer et al., 2012)

^b (Eithiraj et al., 2007)

^c (Baumeier et al., 2007)

^d (Doll et al., 1996)

^e (Madelung et al., 1982)

Table 3.1 (Continued) The calculated lattice parameters of selected metal oxides with LDA and GGA functionals accompanying with the corresponding experimental values. The values in the parenthesis represent the percentage error between the calculated and the experimental values.

Compound	Structure	Lattice parameters (Å)		
		LDA	GGA	Expt.
Group III oxide				
Al ₂ O ₃	Corundum	$a = 4.73$ (-0.63%)	$a = 4.81$ (+1.05%)	$a = 4.76$
		$c = 12.91$ (-0.62%)	$c = 13.11$ (+0.92%)	$c = 12.99^f$
Ga ₂ O ₃	Monoclinic	$a = 12.15$ (-0.65%)	$a = 12.41$ (+1.47%)	$a = 12.23$
		$b = 2.99$ (-1.64%)	$b = 3.16$ (+3.95%)	$b = 3.04$
		$c = 5.70$ (-1.72%)	$c = 6.02$ (+3.79%)	$c = 5.80^g$
In ₂ O ₃	Bixbyite	$a = 10.08$ (-0.40%)	$a = 10.29$ (+1.68%)	$a = 10.12^h$

^f (Finger and Hazen, 1978)

^g (He et al., 2006)

^h (Körber et al., 2010)

values, especially for group III oxides, i.e., Al₂O₃, Ga₂O₃, and In₂O₃. On the other hand, for metal nitrides, the calculated heat of formations with GGA functional provide better agreement with the experimental values. Although the calculations with both LDA and GGA functionals yields a good description of crystal structures as well as heat of formations, these functionals always give underestimation of the band gap (not shown).

Table 3.2 The calculated lattice parameters of selected metal nitrides with LDA and GGA functionals accompanying with the corresponding experimental values. The values in the parenthesis represent the percentage error between the calculated and the experimental values.

Compound	Structure	Lattice parameters (Å)		
		LDA	GGA	Expt.
Group I nitride				
Li ₃ N	Hexagonal	$a = 3.56$ (-2.47%)	$a = 3.65$ (0.00%)	$a = 3.65$
		$c = 3.80$ (-2.06%)	$c = 3.88$ (0.00%)	$c = 3.88^a$
Group II nitrides				
Be ₃ N ₂	Antibixbyite	$a = 8.04$ (-1.35%)	$a = 8.16$ (+0.12%)	$a = 8.15^b$
Mg ₃ N ₂	Antibixbyite	$a = 9.82$ (-1.41%)	$a = 10.00$ (+0.40%)	$a = 9.96^b$
Ca ₃ N ₂	Antibixbyite	$a = 11.21$ (-2.27%)	$a = 11.55$ (+0.70%)	$a = 11.47^c$
Sr ₃ N ₂	Antibixbyite	$a = 12.03$ (-2.35%)	$a = 12.32$ (0.00%)	$a = 12.32^d$

^a (Hossain et al., 2009)

^b (Moreno Armenta et al., 2000)

^c (Heyns et al., 1998)

^d (Römer et al., 2009)

Table 3.2 (Continued) The calculated lattice parameters of selected metal nitrides with LDA and GGA functionals accompanying with the corresponding experimental values. The values in the parenthesis represent the percentage error between the calculated and the experimental values.

Compound	Structure	Lattice parameters (Å)		
		LDA	GGA	Expt. ^e
Group III nitrides				
AlN	Wurtzite	$a = 3.07$ (-1.29%)	$a = 3.11$ (0.00%)	$a = 3.11$
		$c = 4.97$ (-0.20%)	$c = 5.03$ (+1.00%)	$c = 4.98$
GaN	Wurtzite	$a = 3.18$ (-0.31%)	$a = 3.21$ (+0.63%)	$a = 3.19$
		$c = 5.19$ (0.00%)	$c = 5.24$ (+0.96%)	$c = 5.19$
InN	Wurtzite	$a = 3.54$ (0.00%)	$a = 3.57$ (+0.85%)	$a = 3.54$
		$c = 5.76$ (-1.05%)	$c = 5.80$ (+1.75%)	$c = 5.70$

^e (Zoroddu et al., 2001)

3.3.2 Defect Properties

3.3.2.1 Defect Positioning To create a substitutional defect, i.e., N_O defect in metal oxides and O_N defect in metal nitrides, N or O atoms will be replaced on one of anions in metal oxides or metal nitrides supercell. However, in some structures, there are nonequivalent anion sites, i.e., three nonequivalent O sites in monoclinic Ga_2O_3 and two nonequivalent N sites in antiperovskite structures including Be_3N_2 , Mg_3N_2 , Ca_3N_2 , and Sr_3N_2 . In this case, the defect was created on each nonequivalent anion site to calculate the ground state total energy associated with

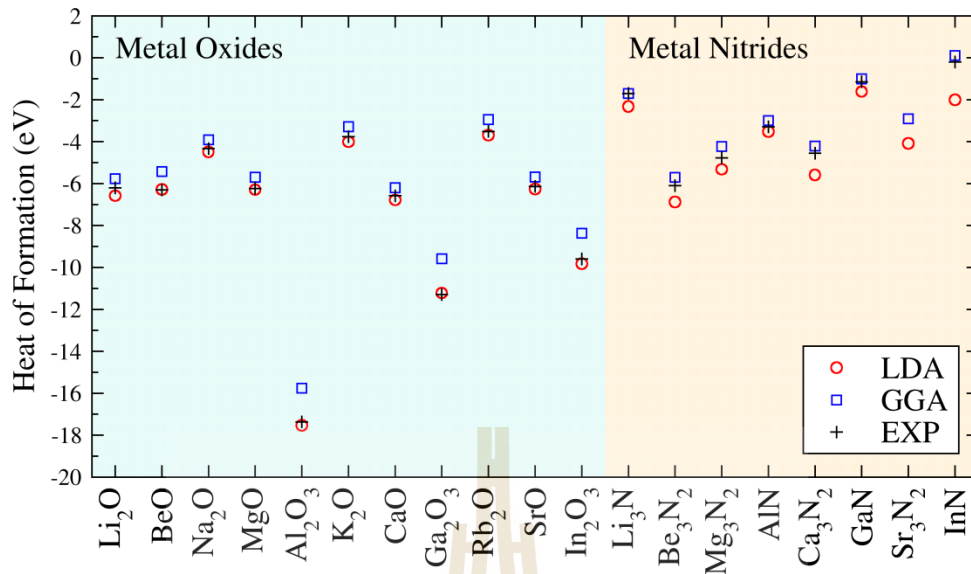


Figure 3.3 The illustration of the calculated heat of formations of selected metal-oxides/nitrides obtained from LDA (red circles) and GGA (blue squares) functionals compared with the available experimental values (black plus signs).

each configuration. Finally, the defect configuration that gives the lowest energy were chosen for further study.

3.3.2.2 Defect formation energies As described in section 3.2.2, the likelihood of defect formation is determined by its formation energy as defined by Eq. (3.3). In order to investigate the effect of the crystal growth conditions on the defect formation energy of N_O and O_N defects in metal oxides and metal nitrides, respectively, the formation energies of N_O and O_N defects in the neutral charge ($q = 0$) were chosen to illustrate under two extreme conditions, i.e., metal-rich and metal-poor growth conditions, as shown in Figure 3.4 and 3.5 for metal oxides and metal nitrides, respectively. The neutral defects are selected because they do not depend on the Fermi level throughout the band gap of materials. The results reveal that N_O defect in metal oxides and O_N defect in metal nitrides prefer to incorporate in the

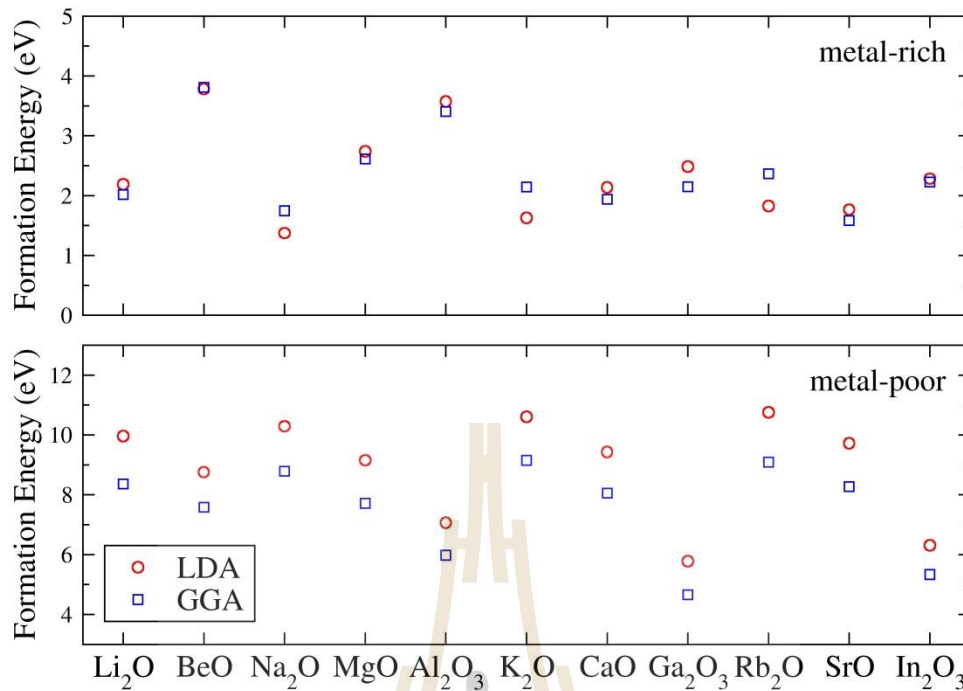


Figure 3.4 The illustration of the calculated defect formation energies of neutral N_O defect in metal oxides under metal-rich (top panel) and metal-poor (bottom panel) growth conditions. The red circles and blue squares represent the calculated results with LDA and GGA functionals, respectively.

crystal under metal-rich condition rather than metal-poor condition. This is because under metal-rich condition the formation of anion vacancy defects, i.e., V_O defect in metal oxides and V_N defect in metal nitrides, are most likely due to the low defect formation energies. Therefore, N or O atom can easily occupy these vacant sites forming N_O or O_N defect. In opposite, the formation energies of anion vacancy defects are quite high under metal-poor condition; resulting in a difficulty of N_O or O_N defect formation.

3.3.2.3 Defect transition levels Regarding N_O defect in metal oxides, the relevant charge states of this defect should be neutral ($q=0$) and a negative

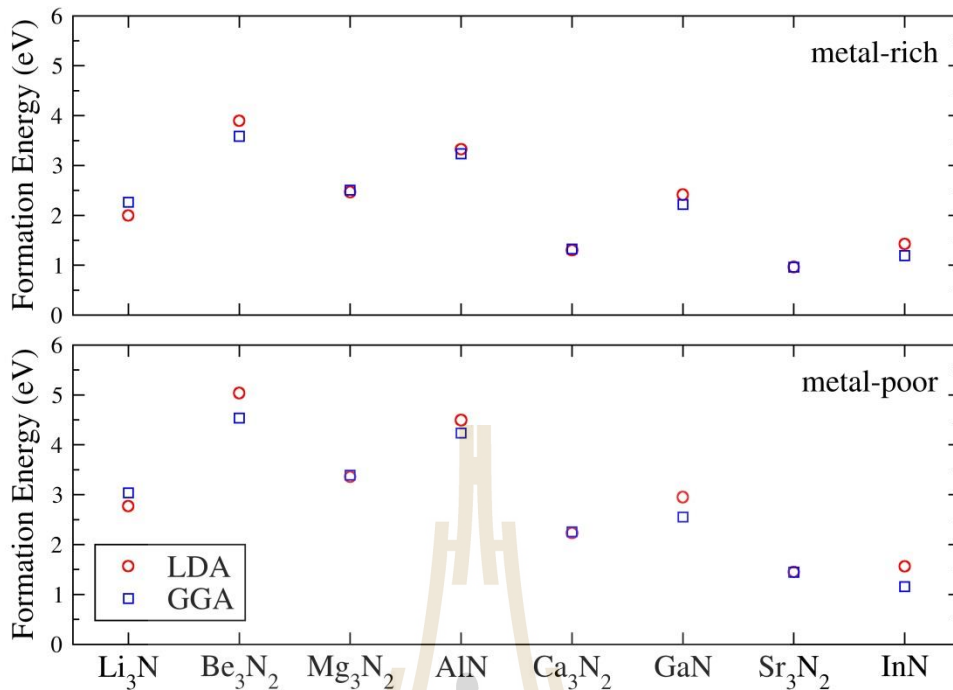


Figure 3.5 The illustration of the calculated defect formation energies of neutral O_N defect in metal nitrides under metal-rich (top panel) and metal-poor (bottom panel) growth conditions. The red circles and blue squares represent the calculated results with LDA and GGA functionals, respectively.

charge state ($q = -1$) because N atom has one valence electron less than O atom. Therefore, N_O defect in metal oxides can act as an acceptor, which might be the cause of hole carrier or p -type conductivity in the materials. However, the defect can be difficult or easy to ionize depending on the defect transition level (or ionization energy). Based on defect formation energy calculations, N_O defect in metal oxides can be stable in both neutral and a negative charge state depending on the Fermi level position. For comparison, the defect transition levels $\varepsilon(\text{O}/-)$ of N_O for selected metal oxides are illustrated in Figure 3.6. It is clearly seen that N_O defect in selected metal oxides always acts as a deep acceptor because $\varepsilon(\text{O}/-)$ levels lie far away from

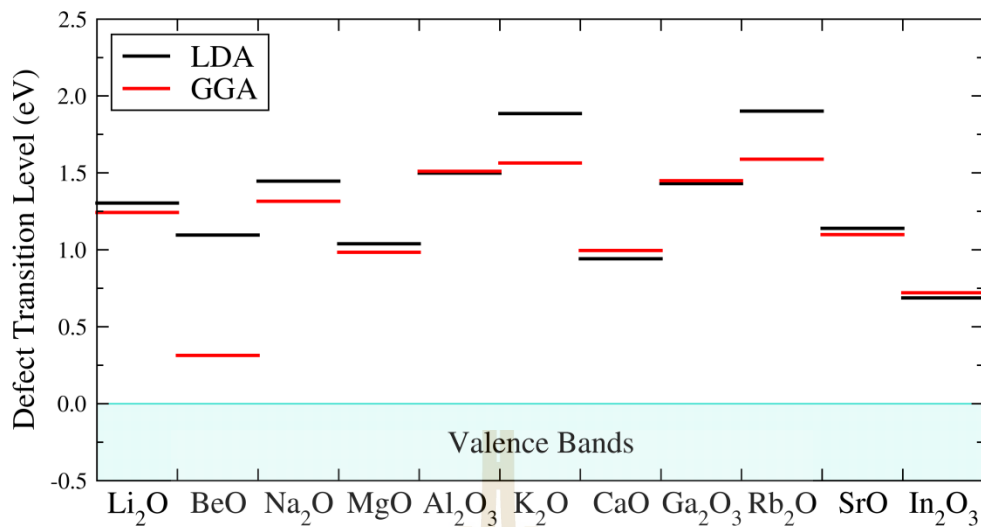


Figure 3.6 Schematic diagram for the defect transition levels $\varepsilon(0/-1)$ of No defect in selected metal oxides obtained from LDA (black lines) and GGA (red lines) functionals. The calculated VBM of each compound is set to zero.

the VBM. Even though the lowest $\varepsilon(0/-)$ level (from BeO with GGA functional) locates at 0.31 eV above the VBM, this level is still too high to be active at room temperature (the thermal energy at room temperature $k_B T \sim 25$ meV).

With regard to O_N defect in metal nitrides, the relevant charge states of this defect are neutral and a single positive charge state ($q = +1$). Then, O_N defect in metal nitrides acts as a donor, which might be the cause of electron carrier or n -type conductivity in the compounds. Based on the calculated formation energies, O_N defect can be stable only in a single positive charge state without introducing any defect level in the band gap. These results reveal that the O_N defect in selected metal nitrides is a single shallow donor and could be a source of unintentional n -type conductivity in several metal nitrides.

Table 3.3 The summary of non-polar plane used in the surface calculations for selected metal oxides to determine the electrostatic potential difference (ΔV) between bulk-like and vacuum regions obtained from LDA and GGA functionals.

Compound	Structure	Non-polar plane	ΔV (eV)	
			LDA	GGA
Group I oxide				
Li ₂ O	Antifluorite	(110)	-5.61	-6.02
Na ₂ O	Antifluorite	(110)	-5.39	-4.87
K ₂ O	Antifluorite	(110)	-3.41	-2.91
Rb ₂ O	Antifluorite	(110)	-3.56	-3.08
Group II oxide				
BeO	Wurtzite	(11 $\bar{2}$ 0)	-11.23	-10.66
MgO	Rocksalt	(100)	-10.61	-9.88
CaO	Rocksalt	(100)	-6.86	-7.83
SrO	Rocksalt	(100)	-5.63	-5.32
Group III oxide				
Al ₂ O ₃	Corundum	(001)	-12.86	-12.36
Ga ₂ O ₃	Monoclinic	(100)	-11.20	-9.94
In ₂ O ₃	Bixbyite	(111)	-12.32	-11.60

3.3.2.4 Band alignment calculations To compare the electronic properties, including VBM, CBM, and $\varepsilon(0/-)$ level, obtained from different materials as well as different functional, the surface calculations were separately performed to determine the electrostatic potential differences ΔV between bulk-like

Table 3.4 The summary of non-polar plane used in the surface calculations for selected metal nitrides to determine the electrostatic potential difference (ΔV) between bulk-like and vacuum regions obtained from LDA and GGA functionals.

Compound	Structure	Non-polar plane	ΔV (eV)	
			LDA	GGA
Group I nitride				
Li ₃ N	Hexagonal	(10 $\bar{1}$ 0)	-4.51	-4.96
Group II nitride				
Be ₃ N ₂	Antibixbyite	(111)	-10.86	-10.47
Mg ₃ N ₂	Antibixbyite	(111)	-8.41	-7.85
Ca ₃ N ₂	Antibixbyite	(111)	-5.03	-5.98
Sr ₃ N ₂	Antibixbyite	(111)	-4.56	-4.24
Group III nitride				
AlN	Wurtzite	(11 $\bar{2}$ 0)	-12.41	-12.03
GaN	Wurtzite	(11 $\bar{2}$ 0)	-9.76	-9.32
InN	Wurtzite	(11 $\bar{2}$ 0)	-12.13	-11.38

and vacuum regions. The calculated results of ΔV for different compounds are demonstrated in Table 3.3 and 3.4 for selected metal oxides and metal nitrides, respectively. These values were then added to such levels of each compound obtained from bulk calculation to align them with respect to vacuum level. The aligned VBM and CBM for metal oxides and metal nitrides were demonstrated in Figure 3.7 and 3.8, respectively. In addition, the aligned $\varepsilon(0/-)$ level of N_o defect in metal oxides

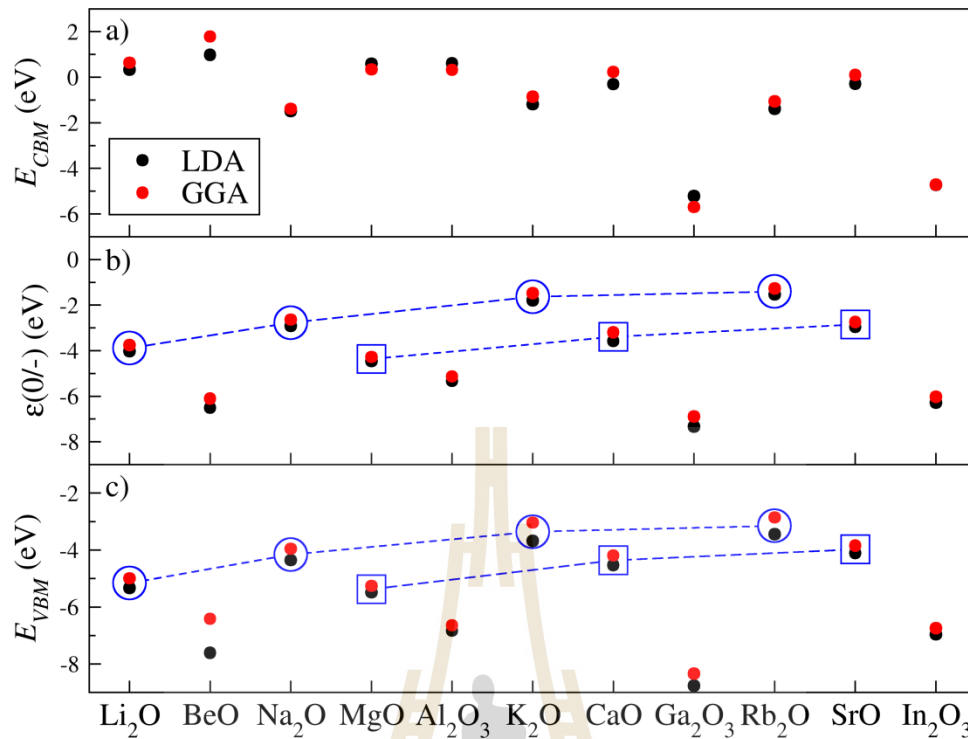


Figure 3.7 The illustrations of (a) CBM, (b) defect transition level $\epsilon(0/-)$, and (c) VBM aligned with the vacuum level for selected metal oxides obtained from LDA (black filled circles) and GGA (red filled circles) functionals. The blue circles represent group I oxides (Li₂O, Na₂O, K₂O, and Rb₂O) having the same antifluorite structure and the blue squares represent group II oxides (MgO, CaO, and SrO) having the same rocksalt structure.

are also illustrated in Figure 3.7. Considering metal oxides having the same crystal structure in Figure 3.7 enclosed by the blue circles and squares for group I and II oxides, respectively, VBM and $\epsilon(0/-)$ positions are increased when increasing metal's atomic size. However, there is no trend for group III oxides (Al₂O₃, Ga₂O₃, and In₂O₃) because these oxides crystallize in different structure. Similarly, in Figure 3.8, the group II and III nitrides having the same crystal structure are enclosed by blue

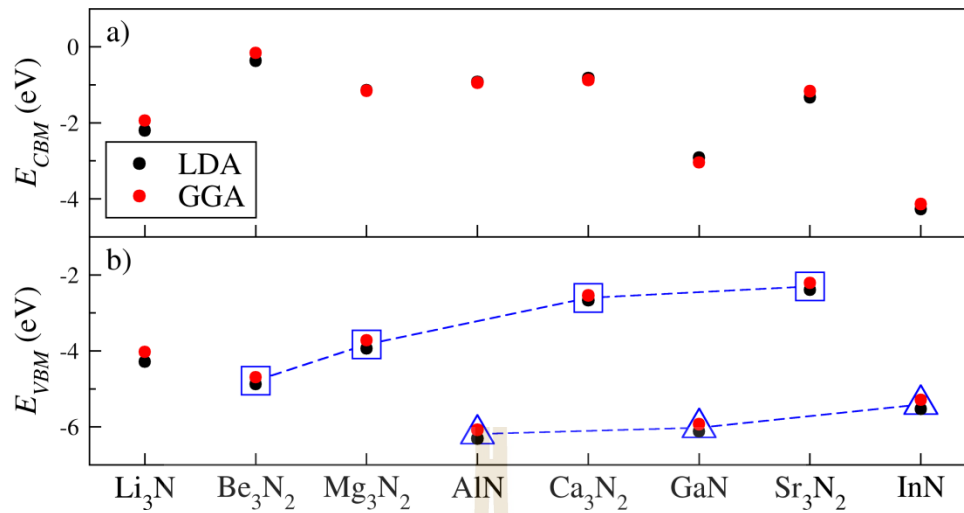


Figure 3.8 The illustrations of (a) CBM and (b) VBM positions aligned with the vacuum level for selected metal nitrides obtained from LDA (black filled circles) and GGA (red filled circles) functionals. The blue squares represent group II nitrides (Be_3N_2 , Mg_3N_2 , Ca_3N_2 , and Sr_3N_2) having the same antibixbyite structure and the blue triangles represent group III nitrides (AlN , GaN , and InN) having the same wurtzite structure.

squares and triangles, respectively, VBM positions also show the same behavior as found in the case of metal oxides. Note that the defect transition levels $\varepsilon(+/0)$ of O_N defect are not depicted because they lie above CBM.

Finally, the effect of different functionals (LDA and GGA) on the electronic levels, including VBM, CBM, and $\varepsilon(0/-)$ level, was investigated and found that such levels after aligned are not sensitive to the functional used in the calculations. It seems that the such levels obtained from the GGA functional yield a bit higher positions than those obtained from the LDA functional.

3.4 Conclusions

In this work, the electrical properties of N_O and O_N defects in various selected metal oxides and metal nitrides, respectively, were systematically investigated by using first-principles DFT calculations with two different functionals, i.e., the LDA and GGA functionals. The results obtained from both LDA and GGA functionals are in good agreement with the experiments for lattice parameters. The calculated heat of formations for metal oxides obtained from LDA functional are much better than those obtained from GGA functional when comparing with the experimental values, especially for group III oxide. In opposite, in metal nitrides, the calculated heat of formations obtained from GGA functional are more in good agreement with the experiments than those obtained from LDA functional.

With regard to metal oxides, N_O defect always acts as a deep acceptor of which the defect transition level lie far away from VBM. Therefore, N_O defect cannot be a cause of the observed *p*-type conductivity in metal oxides. For metal nitrides, O_N defect always acts as a shallow donor defect, which is stable only in a single positive charge state. Therefore, the O_N defect could be responsible for the observed unintentional *n*-type conductivity in metal nitrides.

Finally, the electronic levels obtained from LDA and GGA functionals after aligned with the vacuum level are nearly identical. By considering the electronic levels of the compounds having the same crystal structure: group I oxides (antifluorite structure), group II oxide (rocksalt structure except BeO which has a wurtzite structure), group II nitrides (antibixbyite structure), and group III nitride (wurtzite structure), the VBM (and $\epsilon(0/-)$ for metal oxides only) positions are increased with increasing metal's atomic sizes.

3.5 References

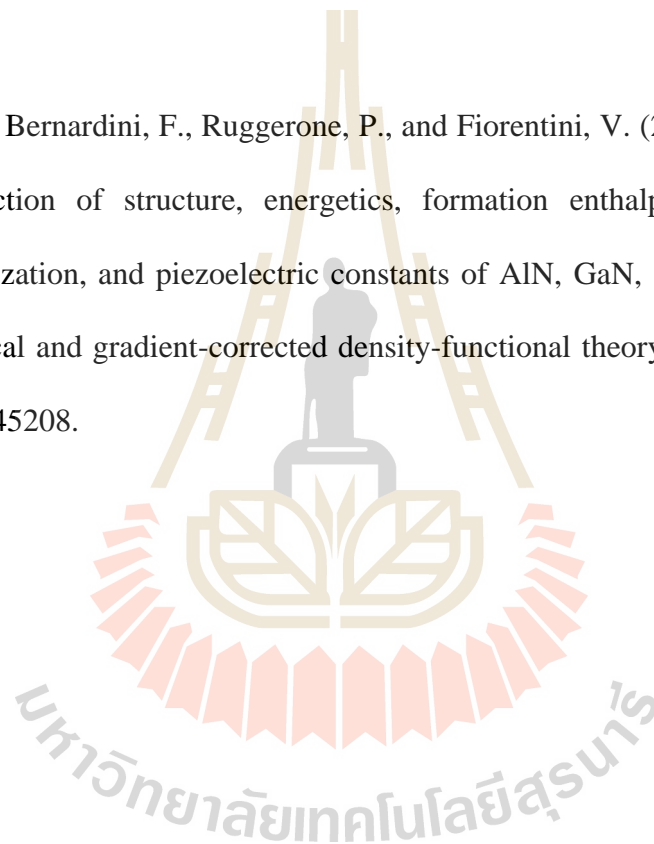
- Ágoston, P., Albe, K., Nieminen, R. M., and Puska, M. J. (2009). Intrinsic *n*-type behavior in transparent conducting oxides: A comparative hybrid-functional study of In₂O₃, SnO₂, and ZnO. **Physical Review Letters** 103: 245501.
- Baumeier, B., Krüger, P., and Pollmann, J. (2007). Atomic and electronic structure of BeO and the BeO(1010) surface: An *ab initio* investigation. **Physical Review B** 75: 045323.
- Blöchl, P. E. (1994). Projector augmented-wave method. **Physical Review B** 50: 17953.
- Boguslawski, P., Briggs, E. L., and Bernholc, J. (1995). Native defects in gallium nitride. **Physical Review B** 51: 17255.
- Brimblecombe, P. (1995). **Air composition and chemistry**. Cambridge: Cambridge University Press.
- Cui, S., Feng, W., Hu, H., Feng, Z., and Wang, Y. (2009). Structural transition of Li₃N under high pressure: A first-principles study. **Solid State Communications** 149: 612.
- de la Cruz, W., Soto, G., and Yubero, F. (2004). Beryllium nitride: an alternative material to beryllium for extreme ultraviolet and soft x-ray uses. **Optical Materials** 25: 39.
- Doll, K., Dolg, M., and Stoll, H. (1996). Correlation effects in MgO and CaO: Cohesive energies and lattice constants. **Physical Review B** 54: 13529.
- Eithiraj, R. D., Jaiganesh, G., and Kalpana, G. (2007). Electronic structure and ground-state properties of alkali-metal oxides–Li₂O, Na₂O, K₂O and Rb₂O: A first-principles study. **Physica B: Condensed Matter** 396: 124.

- Finger, L. W. and Hazen, R. M. (1978). Crystal structure and compression of ruby to 46 kbar. **Journal of Applied Physics** 49: 5823.
- Grüneis, A., Kresse, G., Hinuma, Y., and Oba, F. (2014). Ionization potentials of solids: The importance of vertex corrections. **Physical Review Letters** 112: 096401.
- He, H., Orlando, R., Blanco, M. A., Pandey, R., Amzallag, E., Baraille, I., and Rérat, M. (2006). First-principles study of the structural, electronic, and optical properties of Ga₂O₃ in its monoclinic and hexagonal phases. **Physical Review B** 74: 195123.
- Heyns, A. M., Prinsloo, L. C., Range, K.-J., and Stassen, M. (1998). The vibrational spectra and decomposition of α -calcium nitride (α -Ca₃N₂) and magnesium nitride (Mg₃N₂). **Journal of Solid State Chemistry** 137: 33.
- Hossain, M. A., Islam, A. K. M. A., and Islam, F. N. (2009). Elastic properties of α - and β -phases of Li₃N. **2009** 1: 10.
- Ichikawa, T., Isobe, S., Hanada, N., and Fujii, H. (2004). Lithium nitride for reversible hydrogen storage. **Journal of Alloys and Compounds** 365: 271.
- Körber, C., Krishnakumar, V., Klein, A., Panaccione, G., Torelli, P., Walsh, A., Da Silva, J. L. F., Wei, S. H., Egdell, R. G., and Payne, D. J. (2010). Electronic structure of In₂O₃ and Sn-doped In₂O₃ by hard x-ray photoemission spectroscopy. **Physical Review B** 81: 165207.
- Kresse, G. and Furthmüller, J. (1996). Efficiency of ab-initio total energy calculations for metals and semiconductors using a plane-wave basis set. **Computational Materials Science** 6: 15.

- Kresse, G. and Hafner, J. (1994). Norm-conserving and ultrasoft pseudopotentials for first-row and transition elements. **Journal of Physics: Condensed Matter** 6: 8245.
- Kresse, G. and Joubert, D. (1999). From ultrasoft pseudopotentials to the projector augmented-wave method. **Physical Review B** 59: 1758.
- Liu, H., Avrutin, V., Izyumskaya, N., Özgür, Ü., and Morkoç, H. (2010). Transparent conducting oxides for electrode applications in light emitting and absorbing devices. **Superlattices and Microstructures** 48: 458.
- Madelung, O., Broser, I., Broser, R., Finkenrath, H., Galazka, R. R., Gumlich, H. E., Hoffmann, A., Kossut, J., Mollwo, E., and Nelkowski, H. (1982). **Physics of II-VI and I-VII Compounds, Semimagnetic Semiconductors / Physik der II-VI und I-VII-Verbindungen, semimagnetische Halbleiter Elemente.** Springer Berlin Heidelberg.
- Moakafi, M., Khenata, R., Bouhemadou, A., Khachai, H., Amrani, B., Rached, D., and Rérat, M. (2008). Electronic and optical properties under pressure effect of alkali metal oxides. **The European Physical Journal B** 64: 35.
- Moreno Armenta, M. G., Reyes-Serrato, A., and Avalos Borja, M. (2000). *Ab initio* determination of the electronic structure of beryllium-, aluminum-, and magnesium-nitrides: A comparative study. **Physical Review B** 62: 4890.
- Moses, P. G., Miao, M., Yan, Q., and Walle, C. G. V. d. (2011). Hybrid functional investigations of band gaps and band alignments for AlN, GaN, InN, and InGaN. **The Journal of Chemical Physics** 134: 084703.
- Nicollian, E. H. and Brews, J. R. (1982). **MOS (metal oxide semiconductor) physics and technology.** Wiley.

- Pandey, R., Jaffe, J. E., and Kunz, A. B. (1991). *Ab initio* band-structure calculations for alkaline-earth oxides and sulfides. **Physical Review B** 43: 9228.
- Payne, M. C., Teter, M. P., Allan, D. C., Arias, T. A., and Joannopoulos, J. D. (1992). Iterative minimization techniques for ab initio total-energy calculations: molecular dynamics and conjugate gradients. **Reviews of Modern Physics** 64: 1045.
- Perdew, J. P. and Wang, Y. (1992). Accurate and simple analytic representation of the electron-gas correlation energy. **Physical Review B** 45: 13244.
- Perdew, J. P. and Zunger, A. (1981). Self-interaction correction to density-functional approximations for many-electron systems. **Physical Review B** 23: 5048.
- Piprek, J. (2007). **Nitride Semiconductor Devices: Principles and Simulation**. Wiley.
- Römer, S. R., Dörfler, T., Kroll, P., and Schnick, W. (2009). Group II element nitrides M_3N_2 under pressure: a comparative density functional study. **Physica Status Solidi (b)** 246: 1604.
- Shi, G. A., Saboktakin, M., Stavola, M., and Pearton, S. J. (2004). “Hidden hydrogen” in as-grown ZnO. **Applied Physics Letters** 85: 5601.
- Slater, J. C. (1964). Atomic radii in crystals. **The Journal of Chemical Physics** 41: 3199.
- Sommer, C., Krüger, P., and Pollmann, J. (2012). Quasiparticle band structure of alkali-metal fluorides, oxides, and nitrides. **Physical Review B** 85: 165119.
- Van de Walle, C. G. (2000). Hydrogen as a cause of doping in zinc oxide. **Physical Review Letters** 85: 1012.

- Van de Walle, C. G. and Martin, R. M. (1987). Theoretical study of band offsets at semiconductor interfaces. **Physical Review B** 35: 8154.
- Van de Walle, C. G. and Neugebauer, J. (2003). Universal alignment of hydrogen levels in semiconductors, insulators and solutions. **Nature** 423: 626.
- Walle, C. G. V. d. and Neugebauer, J. (2004). First-principles calculations for defects and impurities: Applications to III-nitrides. **Journal of Applied Physics** 95: 3851.
- Zoroddu, A., Bernardini, F., Ruggerone, P., and Fiorentini, V. (2001). First-principles prediction of structure, energetics, formation enthalpy, elastic constants, polarization, and piezoelectric constants of AlN, GaN, and InN: Comparison of local and gradient-corrected density-functional theory. **Physical Review B** 64: 045208.



CHAPTER IV

LOCAL STRUCTURES OF MAGNESIUM IN MAGNESIUM ZINC OXIDE ALLOY

4.1 Introduction

Magnesium zinc oxide ($\text{Mg}_x\text{Zn}_{1-x}\text{O}$ or MZO) alloy is an alloy between zinc oxide (ZnO) and magnesium oxide (MgO). Due to a wide difference in the band gaps of wurtzite (WZ) ZnO and rocksalt (RS) MgO, i.e., 3.3 eV (Özgür et al., 2005) and 7.8 eV (Roessler and Walker, 1967), respectively, the bandgap of MZO can be tuned and controlled to any value in the range of 3.3 - 7.8 eV depending on the Mg composition (x) (Capasso, 1987; Makino et al., 2001). This technique, called the band gap engineering, makes MZO appropriate from blue to ultraviolet in optoelectronic applications (Sharma et al., 1999; Zhu et al., 2011). MZO thin films and nanostructures can be synthesized by several techniques such as molecular beam epitaxy (Shibata et al., 2007), metal organic vapor-phase epitaxy (Zeng et al., 2007), pulsed laser deposition (Ohtomo et al., 1998), radio frequency (RF) sputtering (Cong et al., 2006), and chemical based methods (Ghosh and Basak, 2007). Because the electronic as well as optoelectronic applications of MZO are mostly concerned with changing the alloy composition, the local crystal structure along with alloy composition is an important factor that controls such properties.

Because of the difference in the microscopic structures between WZ-ZnO and RS-MgO, the microscopic structures of MZO are generally believed to be a mixture

of these two structures, depending on the Mg concentration. Previous studies (Bendersky et al., 2005) has analyzed the microscopic structures of the MZO by using the x-ray diffraction (XRD) technique and shown that the structure of MZO is WZ when $x < 0.40$. For $0.40 < x < 0.60$, MZO contains a mixture of WZ and RS structures. For $x > 0.60$, the structure of MZO completely transforms to RS. However, the traditional XRD technique requires long-range ordering and this technique is not elemental selective. Therefore only the average crystal structure can be detected. To investigate the local environments of the specific atom in the sample, the synchrotron x-ray absorption near edge structure (XANES) technique is more suitable than the XRD technique. Several groups have reported investigations of MZO alloy by using XANES technique (Mayes et al., 2015; Mizoguchi et al., 2007; Ogata et al., 2013). However, their results were based on the assumption that MZO alloys have either the WZ or RS structure.

In this work, the synchrotron XANES technique was performed to investigate the local environments of the specific cations in MZO alloy in various Mg compositions over the whole composition range. The fractions of Mg and Zn local structures in MZO alloy were analyzed to examine the miscibility between WZ and RS phases. In addition, first-principles density functional calculations are employed to investigate the most stable form of Mg defect in WZ-ZnO by considering the defect formation energy. To compare our calculated results with the experiment, some selected stable forms of Mg defect will be used to simulate the XANES spectra by using FEFF codes (Ankudinov et al., 1998; Rehr et al., 2009).

4.2 Experimental Details

MZO nanocrystal samples were synthesized based on an oxalate-based co-precipitation method (Risbud et al., 2003). Zinc acetate, magnesium acetate, and oxalic acid with selected ratios were used as precursors. Based on energy dispersive x-ray spectroscopy measurements, the Mg composition (x) in MZO samples are determined to be $x = 0.00, 0.01, 0.04, 0.10, 0.15, 0.25, 0.30, 0.35, 0.50, 0.70, 0.80, 0.90,$ and 1.00 consistent with the fractions used in the preparation process. The ultraviolet-visible absorption measurements have confirmed that the main absorption edges are blue shifted for MZO samples with higher Mg composition.

XANES spectra measurements were measured at beamline 8 of the Siam Photon Laboratory, Synchrotron Light Research Institute, Thailand. The storage ring was run at 1.2 GeV with a beam current of 80 - 120 mA during the measurements (Klysubun et al., 2007). The XANES measurements were collected in the fluorescence mode using KTP (011) and Ga (220) double crystal monochromators for Mg *K*-edge (1,303 eV) and Zn *K*-edge (9,659 eV), respectively. A 13-element Ge detector was used for detection of x-ray photons emitted from the sample. The x-ray transparent Kapton[®] tape was used to hold the samples. The absolute energies of Mg and Zn absorption edges were calibrated by using standard RS-MgO and WZ-ZnO powders and compared with the literatures (Kunisu et al., 2004; Luches et al., 2004; Tanaka et al., 2005). All spectra were collected at the energy step of 0.25 eV.

4.3 Computational Details

The first-principles calculations based on density functional theory (DFT) within the local density approximation (LDA) were used in this work (Stampfl and

Van de Walle, 1999). The electron-ion interactions were treated by the projector augmented-wave (PAW) method as implemented in the Vienna *ab initio* simulation package (VASP) codes (Blöchl, 1994; Kresse and Furthmüller, 1996; Kresse and Hafner, 1994; Kresse and Joubert, 1999). The energy cutoff of 500 eV was used for expanding the plane-wave basis set.

For Mg defects calculations, a supercell approach with 96-atom supercell was carried out. The Monkhorst-Pack scheme with the sampling mesh points of $2 \times 2 \times 2$ was used for k -space integration (Monkhorst and Pack, 1976). The stability and likelihood of defect formation could be determined by its formation energy. The formation energy of a defect D in charge state q is defined as (Van de Walle and Neugebauer, 2004)

$$E^f[D^q] = E_{\text{tot}}[D^q] - E_{\text{tot}}[\text{bulk}] - \sum_i n_i \mu_i + q(E_F + E_v), \quad (4.1)$$

where $E_{\text{tot}}[D^q]$ is the total energy of a supercell with defect D in a charge state q , $E_{\text{tot}}[\text{bulk}]$ is the total energy of a perfect supercell, n_i is the number of atoms species i ($i = \text{Mg}, \text{Zn}, \text{and O}$) being added to ($n_i > 0$) or removed from ($n_i < 0$) the supercell to create the defect D , μ_i is the corresponding atomic chemical potential, and E_F is the Fermi level referenced to the valence band maximum (E_v). To grow a single crystal ZnO under thermodynamic equilibrium, it is required that $\mu_{\text{ZnO}} = \mu_{\text{Zn}} + \mu_{\text{O}}$, where μ_{ZnO} is the total energy per molecular formula of WZ-ZnO. The upper limits of μ_{Zn} and μ_{O} are the energies per atom of metallic Zn and gaseous O_2 ($\mu_{\text{O}} = E_{\text{tot}}[\text{O}_2]/2$), respectively. For Mg defect, the chemical potential of Mg (μ_{Mg})

was limited by RS-MgO under both Zn- and O-rich growth conditions, i.e.,

$$\mu_{\text{Mg}} = \mu_{\text{MgO}} - \mu_{\text{O}}.$$

In addition, some defects created in a crystal might bind with other defect to form a complex defect. The stability of complex defect formation can be determined by (Van de Walle and Neugebauer, 2004)

$$E_b[\text{A-B}] = E^f[\text{A}] + E^f[\text{B}] - E^f[\text{A-B}], \quad (4.2)$$

where $E_b[\text{A-B}]$ is the binding energy of the complex defect between defect A and B, the first two terms on the right side are the formation energies of individual defect A and B, respectively, and $E^f[\text{A-B}]$ is the formation energy of the A-B complex defect. The higher the binding energy, the more the likelihood of complex formation could be obtained. In opposite, the negative binding energy means that the formation of such complex is unstable.

To compare our calculated results with the x-ray absorption measurement, the optimized structures obtained from VASP codes were used as an input for the FEFF codes to simulate the XANES spectrum. The FEFF codes utilize a full multiple scattering approach, which is based on *ab-initio* overlapping muffin-tin potentials (Slater, 1953). The muffin-tin potentials are obtained using self-consistent calculations with the Hedin-Lundqvist exchange-correlation function (Hedin and Lundqvist, 1971). All calculations were carried out within the cluster size of 10.00 Å. The self-consistent calculations included only the atoms being in the cluster radius of 5.50 Å. The full multiple scattering calculations including all possible paths were employed for the atoms being in the cluster radius of 8.40 Å.

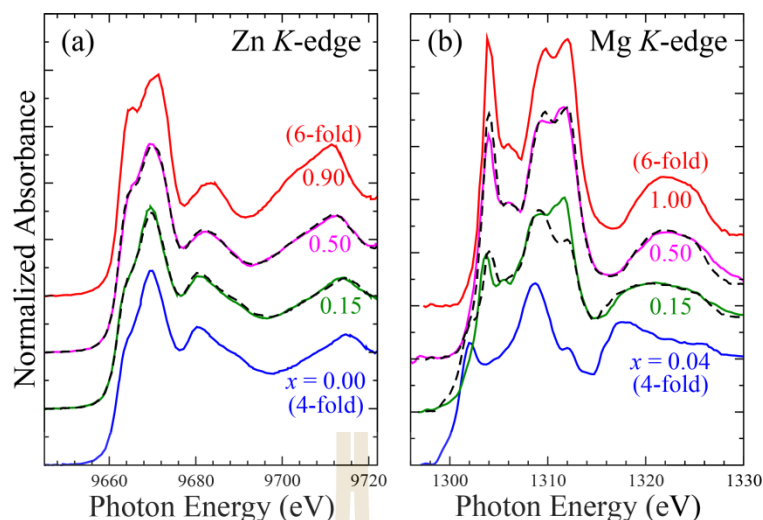


Figure 4.1 The measured (a) Zn *K*-edge and (b) Mg *K*-edge XANES spectra of MZO alloys. The number labeled on each spectrum is the Mg mole fraction (x). For the mixed phase ($x = 0.15$ and 0.50), the linear combination fits based on 4-fold WZ and 6-fold RS spectra for each cation species are shown using dashed lines.

4.4 Results and Discussion

4.4.1 Zn and Mg *K*-edge XANES measurements

The measured Zn *K*-edge and Mg *K*-edge XANES spectra from MZO alloy samples are shown in Figure 4.1(a) and (b), respectively. For the Zn *K*-edge XANES spectra, the spectrum of pure ZnO ($x = 0.00$) certainly represents the signature of Zn in 4-fold coordination, while the spectrum of nearly pure MgO ($x = 0.90$) almost represents the signature of Zn in 6-fold coordination, i.e., Zn substitution for Mg (Zn_{Mg}) in RS-MgO. Similarly, the Mg *K*-edge XANES spectrum of pure MgO ($x = 1.00$) certainly represents the signature of Mg in 6-fold coordination, while the spectrum of nearly pure ZnO ($x = 0.04$) represents the signature of Mg in 4-fold coordination, i.e., Mg substitution for Zn (Mg_{Zn}) in WZ-ZnO. Since Zn atom can

Table 4.1 The phase fractions of Mg (f_{Mg}) and Zn (f_{Zn}) in 6-fold coordination of $\text{Mg}_x\text{Zn}_{1-x}\text{O}$ alloys obtained by linear combination fits between 4-fold WZ and 6-fold RS spectra for each Mg and Zn K -edge XANES measurements. The RS phase fractions (F_{RS}) were obtained from Eq. (4.3).

x	f_{Mg}	f_{Zn}	F_{RS}
0.00	0.00	0.00	0.00
0.01	0.00	0.00	0.00
0.04	0.01	0.01	0.01
0.10	0.15	0.03	0.04
0.15	0.37	0.07	0.12
0.25	0.47	0.18	0.25
0.30	0.56	0.25	0.34
0.35	0.74	0.33	0.47
0.50	0.90	0.54	0.72
0.70	0.97	0.81	0.92
0.80	0.99	0.92	0.98
0.90	1.00	1.00	1.00
1.00	1.00	0.00	1.00

substitute for Mg in RS-MgO and, on the other hand, Mg atom can substitute for Zn in WZ-ZnO. For the mixed phase, the measured Zn or Mg K -edge XANES spectra should contain the features from both the 4-fold WZ and 6-fold RS coordinations and the linear combination method based on 4-fold WZ and 6-fold RS spectra could be used to identify the fraction of 4-fold and 6-fold coordinations in the samples. Table

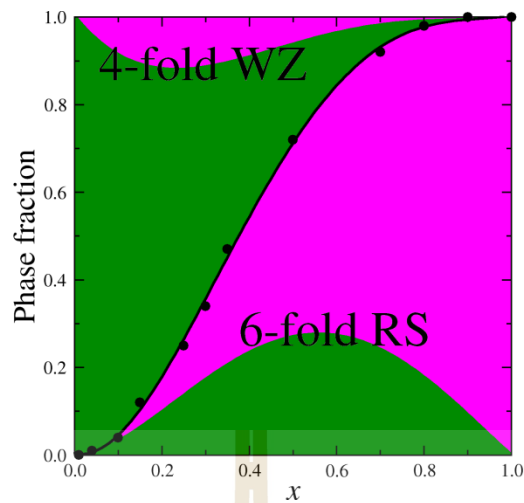


Figure 4.2 Phase fractions of $\text{Mg}_x\text{Zn}_{1-x}\text{O}$ alloy with different the Mg mole fraction (x) as determined by the linear combination fits from measured Zn and Mg K -edge XANES spectra (black circle). The area under (above) the black curve represents the fraction of 6-fold RS (4-fold WZ) phase. The cation compositions for each phase were represented by different color, magenta and green for Mg and Zn, respectively.

4.1 shows the fraction of Mg and Zn atoms with 6-fold coordination, f_{Mg} and f_{Zn} , respectively, obtained from linear combination fits based on the 4-fold WZ and 6-fold RS for each cation species. The RS phase fraction (F_{RS}) can then be determined by

$$F_{\text{RS}} = x f_{\text{Mg}} + (1-x) f_{\text{Zn}} \quad (4.3)$$

The plot of phase fraction as a function of the Mg composition (x) was shown in Figure 4.2. The area under the curve is associated with the RS phase and the area above the curve is associated with the WZ phase, which is $1 - F_{\text{RS}}$. Since the XANES analysis allows not only the determination of the phase fraction but also the individual contribution of each selected cation species, the contributions from each cation species was shown in different color, magenta and green for Mg and Zn, respectively.

These colors show that the majority cation contribution in RS phase is Mg while the majority cation contribution in WZ phase is Zn.

4.4.2 Computational Results

From previous section, the linear combination fits of the measured Zn *K*-edge XANES spectra based on the 4-fold WZ and 6-fold RS coordination well represent the measured XANES spectra of all intermediate phase MZO as illustrated in Figure 4.1(a). However, for Mg *K*-edge XANES spectra, the deficiency of the fitting results based on only two structures, i.e., 4-fold and 6-fold coordination can be detected for the intermediated alloy compositions as depicted in Figure 4.1(b). This suggests the existence of other form(s) of Mg in MZO samples and more additional base, beside the 4-fold WZ and 6-fold RS, should be included in the fitting. In this section, first-principles calculations were used to examine other plausible forms of Mg in the MZO alloy.

4.4.2.1 Intrinsic and Mg Defects in WZ-ZnO As mentioned in the section 4.3, the likelihood of defect formation, including intrinsic and Mg-related defects, could be investigated by calculating its formation energy. In addition, the results of intrinsic defects can be further used to compare with the previous works to check the reliability of our calculation method.

Figure 4.3 illustrates the formation energies of dominant native point defects in ZnO, i.e., Zn vacancy (V_{Zn}), O vacancy (V_O), Zn interstitial (Zn_i), and O interstitial (O_i) as a function of Fermi energy under Zn-rich and O-rich growth conditions. The calculated results are in a reasonable agreement with the previous work (Janotti and Van de Walle, 2007). For vacancy defects, V_{Zn} defect is a multicharge deep acceptor with two defect transition levels at $\epsilon(0/-) = 0.26$ eV and $\epsilon(-/2-) = 0.31$ eV, while V_O

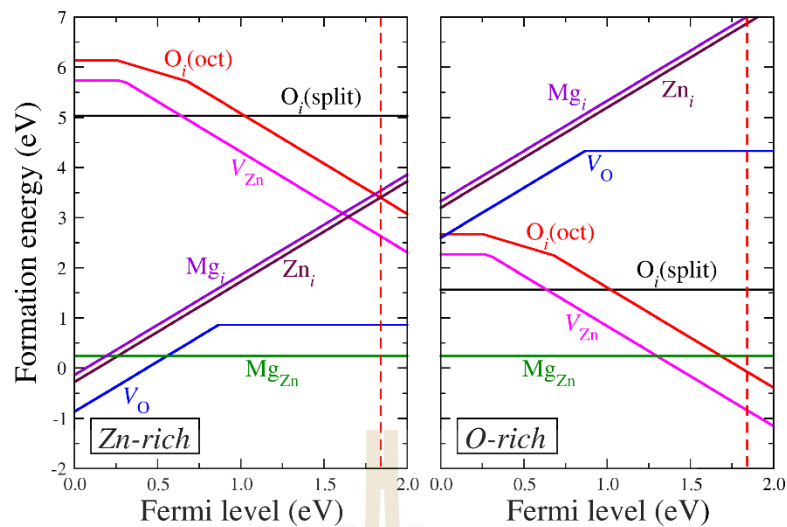


Figure 4.3 The illustration of formation energies of native defects and Mg defects in WZ-ZnO as a function of Fermi level calculated under Zn-rich (left panel) and O-rich (right panel) growth conditions. The slope of each line indicates the charge state of the defect. The Fermi level, referenced to the (special k -point) VBM of bulk, is shown up to the calculated band gap at the special k -point (the vertical dashed line).

defect is a deep double donor with a defect transition level at $\varepsilon(2+/0) = 0.87$ eV. For interstitial defect, Zn_i defect is a shallow donor without any defect transition level. For O_i defect, there are two possible configurations: (1) O_i binding with the host O atom forming O_2 -like molecule, named as $O_i(\text{split})$ and (2) O_i sitting in the octahedral site, named as $O_i(\text{oct})$. $O_i(\text{split})$ is a neutral defect without any defect transition level, but $O_i(\text{oct})$ is a deep multicharge acceptor with two defect transition levels at $\varepsilon(0/-) = 0.26$ eV and $\varepsilon(-/2-) = 0.68$ eV. Under Zn-rich growth condition, V_O has the lowest formation energy throughout the Fermi energy. However, under O-rich conditions, the formation energy of V_{Zn} is the lowest when the Fermi energy is above 0.6 eV, otherwise $O_i(\text{split})$ turns to be the lowest energy defect.

Regarding Mg defects, two plausible forms of Mg defects were investigated: (1) Mg substitution for Zn site (Mg_{Zn}) and (2) Mg interstitial defect in the octahedral site (Mg_i). The formation energies of Mg defects as a function of Fermi energy under Zn-rich and O-rich growth conditions are also shown in Figure 4.3. The results revealed that Mg_{Zn} is a neutral defect because Mg and Zn atoms are isovalent, whereas Mg_i is a shallow double donor defect without any defect transition level. It is clearly seen that under O-rich growth condition the formation energy of Mg_{Zn} is lower than that of Mg_i throughout the Fermi energy, but under Zn-rich growth condition Mg_i turns to be lower when the Fermi level is close to the VBM. In practice, as-grown WZ-ZnO is a *n*-type semiconductor, which means that the Fermi level is quite far from the VBM. Therefore, it is quite safe to conclude that Mg_{Zn} is the most stable form of Mg defects under both Zn- and O-rich growth conditions with quite low formation energy.

4.4.2.2 Formation of Complex Defects between Mg and Other Native Point Defects As described in section 4.3 and 4.4.2.1, Mg atom in WZ-ZnO is likely to be in the form of Mg_{Zn} defect. Therefore, the likelihood of a complex defect formation between Mg_{Zn} and dominant native point defects will be explored. From Eq. (4.2), the binding energies between Mg_{Zn} and V_O or V_{Zn} defects are all negative. In addition, the binding energy between Mg_{Zn} and Mg_i defects are also negative. This implies that Mg_{Zn} is unlikely to bind with other native point defects. Therefore, these results can help us to rule out the formation of such complex defects as a missing form in the fitting of measured Mg *K*-edge XANES spectra as described in section 4.3.

4.4.2.3 Clustering of Mg_{Zn} in WZ-ZnO In this section, the likelihood of

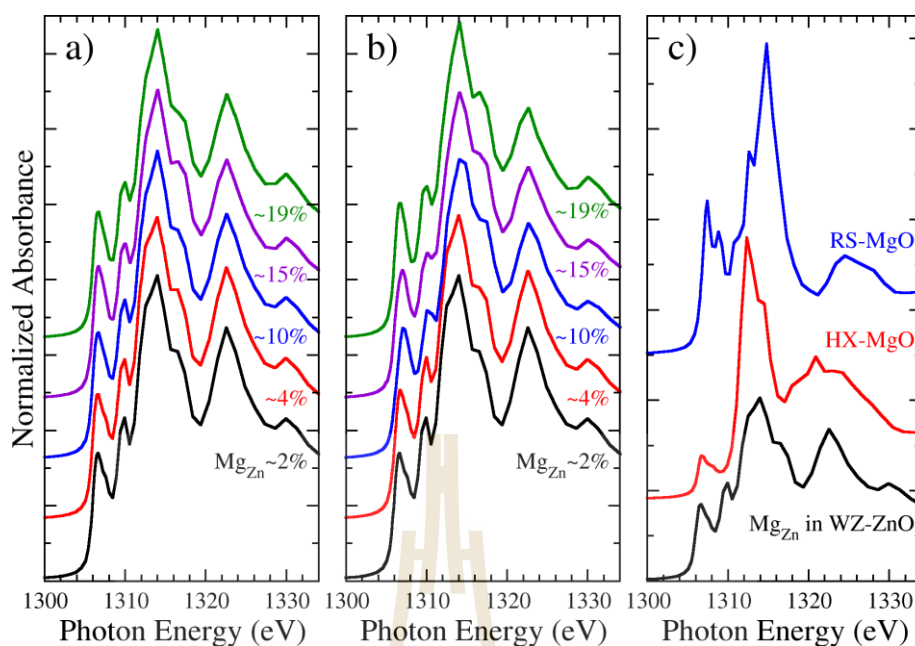


Figure 4.4 Calculated Mg *K*-edge XANES spectra of Mg_{Zn} in WZ-ZnO (a) with random configurations and (b) with cluster configurations at different Mg concentrations. (c) Calculated Mg *K*-edge XANES spectrum of HX-MgO structure compared to that of RS-MgO (upper curve) and Mg_{Zn} in WZ-ZnO (lower curve).

formation of Mg clusters in MZO alloy, the calculations in two sets were carried out: (1) Zn atoms were randomly replaced by Mg atoms and (2) Zn atoms were intentionally replaced by Mg atoms to form a cluster. For each calculation set, the calculations with different Mg concentrations in ZnO, i.e., 2%, 4%, 10%, 15%, and 19% were performed to replicate the Mg concentrations in the experiment. By comparing the total energy for each set of calculations, the results showed that the first case (random) give lower total energy than the second case (cluster). This suggests that Mg_{Zn} cluster is unlikely to form in WZ-ZnO.

Although the calculated results reveal that Mg_{Zn} prefers to stay away from each other as well as away from other native defects, it is still interesting to see how

the Mg cluster affects the features of XANES spectrum. The calculated Mg *K*-edge XANES spectra of Mg_{Zn} in two cases are depicted in Figure 4.4(a) and (b) for random and cluster, respectively. As expected, the calculated spectra from both random and cluster cases are very similar because the local structures around Mg atoms in difference cases are all similar.

4.4.2.4 The 5-fold Mg_{Zn} By using first-principles total energy calculations on homogeneous phase transformation between WZ-MgO and RS-MgO, S. Limpijumnong and W. Lambrecht found a meta stable phase of MgO called unbuckled wurtzite (HX) phase under certain tensile stress conditions (Limpijumnong and Lambrecht, 2001). If one starts the calculation from the WZ-MgO and keeps the volume fixed (so that the structure would not spontaneously relax back to the denser RS phase) but allows full cell shape relaxation, all the buckled [0001] planes would turn to a flat plane; making the Mg atom form 5-fold bonding with the surrounding O atoms and the *c/a* ratio reduces from ~ 1.63 of the WZ structure to ~ 1.20 of the HX structure. Therefore, it is highly plausible that Mg substituting in WZ-ZnO might form a 5-fold coordination. To calculate the XANES spectrum of Mg in 5-fold coordination, the HX-MgO structure was optimized by using the VASP codes. After that, FEFF codes were performed to calculate the Mg *K*-edge XANES spectrum using the optimized crystal structure obtained from VASP codes. The calculated XANES spectrum is illustrated in Figure 4.4(c). It is clearly seen that the features of HX spectrum significantly differ from that of 4-fold (WZ) and 6-fold (RS) coordinations with a distinctive peak (at $\sim 1,314$ eV) centering at the position in between the main peaks of the 4-fold and 6-fold Mg. Looking back at the fit results in Figure 4.1(b) of MZO with $x = 0.15$, the main deficiency (the disagreement between the actual

measurement and the fit) appears at $\sim 1,312$ eV or between the main peaks of the 4-fold and 6-fold spectra. Therefore, a big improvement can be expected by including the spectrum of 5-fold Mg as an additional base in the fit. However, there is currently no experimental XANES spectrum of HX structure for using in the actual fit. Nevertheless, these results serve as compelling evidence that the missing form of Mg phase in the fit might be 5-fold Mg.

4.5 Conclusions

In this research, the synchrotron XANES measurement was employed to determine the local structures of Mg and Zn atoms in MZO alloy samples. The results showed that the MZO alloy composes of mixture between WZ and RS phases. In addition, Zn atom is more soluble in the RS phase than Mg atoms in the WZ phase. The measured Zn *K*-edge XANES spectra of MZO alloy at intermediate alloy compositions can be described well by using 4-fold and 6-fold coordination as bases in the fitting model. However, the deficiency of the fitting results can be detected in the measured Mg *K*-edge XANES spectra. This suggests other forms of Mg in the sample and additional bases should be included in the fit. The first-principles density functional calculations were performed to find the plausible forms of Mg in MZO alloy. The calculated results revealed that (1) the Mg substituted for Zn (Mg_{Zn}), i.e., 4-fold coordination, is the most stable form, (2) Mg_{Zn} does not prefers to bind with any native point defects, and (3) Mg_{Zn} prefers to stay away from each other, i.e., does not prefers to form Mg clusters. The measured Mg *K*-edge XANES spectra indicate another form of Mg beside the 4-fold and 6-fold coordinations and the missing form of Mg in 5-fold coordination is suggested. This is because the 5-fold coordinated Mg

is the normal cation coordination in HX or unbuckled WZ structure. The calculated Mg *K*-edge XANES spectrum of Mg in 5-fold coordination gives the main peak that nicely fits with the missing part of the measured XANES spectra and should be included as one of bases in the linear combination fits to describe the phase fraction of Mg in MZO alloy.

4.6 References

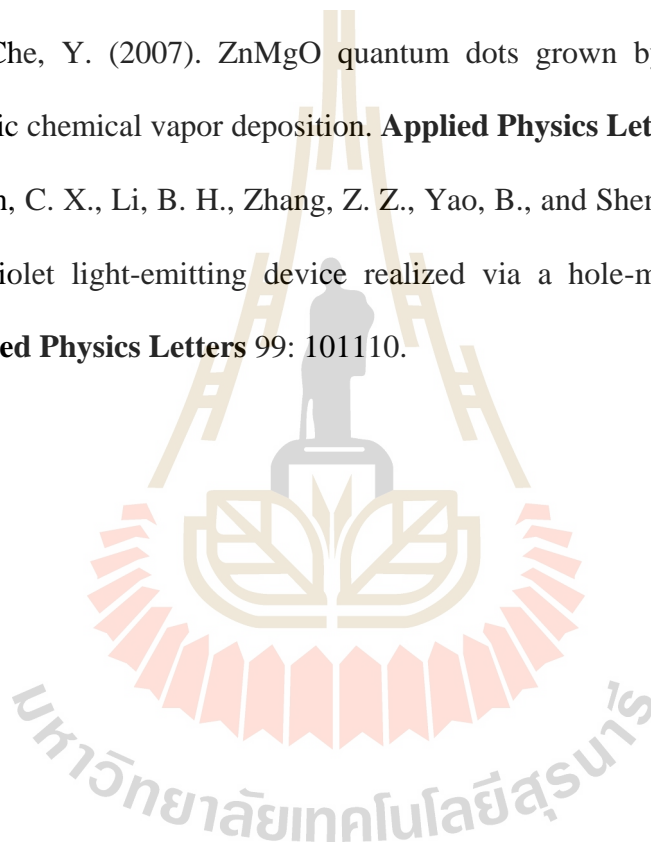
- Ankudinov, A. L., Ravel, B., Rehr, J. J., and Conradson, S. D. (1998). Real-space multiple-scattering calculation and interpretation of x-ray-absorption near-edge structure. **Physical Review B** 58: 7565.
- Bendersky, L. A., Takeuchi, I., Chang, K.-S., Yang, W., Hullavarad, S., and Vispute, R. D. (2005). Microstructural study of epitaxial $Zn_{1-x}Mg_xO$ composition spreads. **Journal of Applied Physics** 98: 083526.
- Blöchl, P. E. (1994). Projector augmented-wave method. **Physical Review B** 50: 17953.
- Capasso, F. (1987). Band-Gap engineering: From physics and materials to new semiconductor devices. **Science** 235: 172.
- Cong, C. X., Yao, B., Xing, G. Z., Xie, Y. P., Guan, L. X., Li, B. H., Wang, X. H., Wei, Z. P., Zhang, Z. Z., Lv, Y. M., Shen, D. Z., and Fan, X. W. (2006). Control of structure, conduction behavior, and band gap of $Zn_{1-x}Mg_xO$ films by nitrogen partial pressure ratio of sputtering gases. **Applied Physics Letters** 89: 262108.

- Ghosh, R. and Basak, D. (2007). Composition dependence of electrical and optical properties in sol-gel $Mg_xZn_{1-x}O$ thin films. **Journal of Applied Physics** 101: 023507.
- Hedin, L. and Lundqvist, B. I. (1971). Explicit local exchange-correlation potentials. **Journal of Physics C: Solid State Physics** 4: 2064.
- Janotti, A. and Van de Walle, C. G. (2007). Native point defects in ZnO. **Physical Review B** 76: 165202.
- Klysubun, W., Sombunchoo, P., Wongprachanukul, N., Tarawarakarn, P., Klinkhieo, S., Chaiprapa, J., and Songsiriritthigul, P. (2007). Commissioning and performance of x-ray absorption spectroscopy beamline at the Siam Photon Laboratory. **Nuclear Instruments & Methods in Physics Research Section a-Accelerators Spectrometers Detectors and Associated Equipment** 582: 87.
- Kresse, G. and Furthmüller, J. (1996). Efficiency of ab-initio total energy calculations for metals and semiconductors using a plane-wave basis set. **Computational Materials Science** 6: 15.
- Kresse, G. and Hafner, J. (1994). Norm-conserving and ultrasoft pseudopotentials for first-row and transition elements. **Journal of Physics: Condensed Matter** 6: 8245.
- Kresse, G. and Joubert, D. (1999). From ultrasoft pseudopotentials to the projector augmented-wave method. **Physical Review B** 59: 1758.
- Kunisu, M., Tanaka, I., Yamamoto, T., Suga, T., and Mizoguchi, T. (2004). The formation of a rock-salt type ZnO thin film by low-level alloying with MgO. **Journal of Physics: Condensed Matter** 16: 3801.

- Limpijumnong, S. and Lambrecht, W. R. L. (2001). Theoretical study of the relative stability of wurtzite and rocksalt phases in MgO and GaN. **Physical Review B** 63: 104103.
- Luches, P., D'Addato, S., Valeri, S., Groppo, E., Prestipino, C., Lamberti, C., and Boscherini, F. (2004). X-ray absorption study at the Mg and O *K* edges of ultrathin MgO epilayers on Ag(001). **Physical Review B** 69: 045412.
- Makino, T., Segawa, Y., Kawasaki, M., Ohtomo, A., Shiroki, R., Tamura, K., Yasuda, T., and Koinuma, H. (2001). Band gap engineering based on $\text{Mg}_x\text{Zn}_{1-x}\text{O}$ and $\text{Cd}_y\text{Zn}_{1-y}\text{O}$ ternary alloy films. **Applied Physics Letters** 78: 1237.
- Mayes, E. L. H., McCulloch, D. G., and Partridge, J. G. (2015). Structural characterisation of energetically deposited $\text{Zn}_{1-x}\text{Mg}_x\text{O}$ films. **Journal of Crystal Growth** 412: 116.
- Mizoguchi, T., Seko, A., Yoshiya, M., Yoshida, H., Yoshida, T., Ching, W. Y., and Tanaka, I. (2007). X-ray absorption near-edge structures of disordered $\text{Mg}_{1-x}\text{Zn}_x\text{O}$ solid solutions. **Physical Review B** 76: 195125.
- Monkhorst, H. J. and Pack, J. D. (1976). Special points for Brillouin-zone integrations. **Physical Review B** 13: 5188.
- Ogata, K., Kozub, M., Koike, K., Sasa, S., Inoue, M., Yano, M., and Tamenori, Y. (2013). Local structure analysis of $\text{Zn}_{1-x}\text{Mg}_x\text{O}$ thin films by soft x-ray absorption spectroscopy. **Physica Status Solidi (c)** 10: 1573.
- Ohtomo, A., Kawasaki, M., Koida, T., Masubuchi, K., Koinuma, H., Sakurai, Y., Yoshida, Y., Yasuda, T., and Segawa, Y. (1998). $\text{Mg}_x\text{Zn}_{1-x}\text{O}$ as a II–VI widegap semiconductor alloy. **Applied Physics Letters** 72: 2466.

- Özgür, Ü., Alivov, Y. I., Liu, C., Teke, A., Reshchikov, M. A., Doğan, S., Avrutin, V., Cho, S.-J., and Morkoç, H. (2005). A comprehensive review of ZnO materials and devices. **Journal of Applied Physics** 98: 041301.
- Rehr, J. J., Kas, J. J., Prange, M. P., Sorini, A. P., Takimoto, Y., and Vila, F. (2009). Ab initio theory and calculations of x-ray spectra. **Comptes Rendus Physique** 10: 548.
- Risbud, A. S., Spaldin, N. A., Chen, Z. Q., Stemmer, S., and Seshadri, R. (2003). Magnetism in polycrystalline cobalt-substituted zinc oxide. **Physical Review B** 68: 205202.
- Roessler, D. M. and Walker, W. C. (1967). Electronic Spectrum and Ultraviolet Optical Properties of Crystalline MgO. **Physical Review** 159: 733.
- Sharma, A. K., Narayan, J., Muth, J. F., Teng, C. W., Jin, C., Kvit, A., Kolbas, R. M., and Holland, O. W. (1999). Optical and structural properties of epitaxial $\text{Mg}_x\text{Zn}_{1-x}\text{O}$ alloys. **Applied Physics Letters** 75: 3327.
- Shibata, H., Tampo, H., Matsubara, K., Yamada, A., Sakurai, K., Ishizuka, S., Niki, S., and Sakai, M. (2007). Photoluminescence characterization of $\text{Zn}_{1-x}\text{Mg}_x\text{O}$ epitaxial thin films grown on ZnO by radical source molecular beam epitaxy. **Applied Physics Letters** 90: 124104.
- Slater, J. C. (1953). An augmented plane wave method for the periodic potential problem. **Physical Review** 92: 603.
- Stampfl, C. and Van de Walle, C. G. (1999). Density-functional calculations for III-V nitrides using the local-density approximation and the generalized gradient approximation. **Physical Review B** 59: 5521.

- Tanaka, I., Mizoguchi, T., and Yamamoto, T. (2005). XANES and ELNES in ceramic science. **Journal of the American Ceramic Society** 88: 2013.
- Van de Walle, C. G. and Neugebauer, J. (2004). First-principles calculations for defects and impurities: Applications to III-nitrides. **Journal of Applied Physics** 95: 3851.
- Zeng, Y. J., Ye, Z. Z., Lu, Y. F., Lu, J. G., Sun, L., Xu, W. Z., Zhu, L. P., Zhao, B. H., and Che, Y. (2007). ZnMgO quantum dots grown by low-pressure metal organic chemical vapor deposition. **Applied Physics Letters** 90: 012111.
- Zhu, H., Shan, C. X., Li, B. H., Zhang, Z. Z., Yao, B., and Shen, D. Z. (2011). Deep-ultraviolet light-emitting device realized via a hole-multiplication process. **Applied Physics Letters** 99: 101110.



CHAPTER V

GALLIUM ACCEPTOR DEFECTS IN TIN DIOXIDE

REVISITED: A HYBRID FUNCTIONAL STUDY

5.1 Introduction

Tin dioxide (SnO_2), known as cassiterite in the mineral form, is one of the most interesting ceramics because of its wide band gap, good transparency, high thermal/chemical resistances, and low cost (Jarzebski and Marton, 1976; Jarzebski and Morton, 1976). Due to its large direct band gap of ~ 3.60 eV (Reimann and Steube, 1998), SnO_2 has been widely applied in various applications, such as transparent conductive oxides (TCOs), solar cells, and solid state gas sensing materials (Advani and Jordan, 1980; Batzill and Diebold, 2005; Yates et al., 2012). The crystal structure of SnO_2 at room temperature is tetragonal rutile, in which the Sn and O atoms are six-fold and three-fold coordinated, respectively (Das and Jayaraman, 2014). Usually, as-grown SnO_2 exhibits *n*-type conductivity with a high carrier concentration, which has been attributed to the intrinsic or extrinsic defects (Fonstad and Rediker, 1971; Masahiro and Shigeo, 1971; Samson and Fonstad, 1973; Stjerna et al., 1990). There are experimentally reports showing that the electrical conductivity strongly depends on the oxygen availability during the crystal growth process (Masahiro and Shigeo, 1971; Samson and Fonstad, 1973). Therefore, the origin of *n*-type conductivity in SnO_2 was assigned to intrinsic defects, especially the

oxygen vacancies (V_o) (Fonstad and Rediker, 1971; Samson and Fonstad, 1973). However, there is no direct evidence to support this assignment.

In order to make SnO_2 usable for a wide range of electronic devices, SnO_2 must be able to be doped into both n - and p -types. However, the inherent n -type conductivity in SnO_2 is an obstacle for making it into p -type semiconductor. In addition, an effective p -type dopant for SnO_2 has not been identified. In principle, substitution of group-III elements for Sn site could make it p -type and there are many literatures studying the feasibility of making p -type SnO_2 (Scanlon and Watson, 2012; Singh et al., 2008; Varley et al., 2009). Singh et al. have used density functional theory (DFT) calculations with GGA+ U method to study SnO_2 doped with group-III elements (Singh et al., 2008). They reported that p -type SnO_2 could be achieved by replacing Sn atom with Al (Al_{Sn}), Ga (Ga_{Sn}), or In (In_{Sn}) atom. Further, Varley et al. have repeated Singh's calculations by using DFT calculations with more accurate hybrid functional proposed by Heyd-Scuseria-Ernzerhof (HSE) with a default Hartree-Fock mixing parameter of 25% (Varley et al., 2009). Their results showed that Al_{Sn} , Ga_{Sn} , and In_{Sn} defects in SnO_2 could act as a shallow acceptor in agreement with Singh's results. However, Scanlon and Watson have reinvestigated the possibility of making p -type SnO_2 by using the PBE0 hybrid functional (Perdew et al., 1996) and revealed that these defects could not act as shallow accepters contradicting to previous results (Scanlon and Watson, 2012). In addition, they found that Ga_{Sn} defect is amphoteric with two defect transition levels $\varepsilon(+/0) = 0.54$ eV and $\varepsilon(0/-) = 1.05$ eV. This conflict is interesting and should be clarified. In this work, the Ga_{Sn} defect in SnO_2 is revisited by using DFT calculations with HSE hybrid functional.

The results showed that Ga_{Sn} actually is a deep acceptor with defect transition level $\varepsilon(0/-) = 0.79 \text{ eV}$.

To find a way to enhance the acceptor concentration, i.e., making the acceptor level shallower, the effects of crystal strain on the acceptor level were studied. It has been illustrated that for the case of Na-doped ZnO, applying the compressive strain can make the acceptor level shallower (Sun et al., 2014). To make it more practical, the compressive strain could be introduced by alloying the host material with an isovalent element that has the same crystal structure but with a smaller lattice constant (Ryu et al., 2006). Here, the compressive strain in SnO_2 is introduced by alloying SnO_2 with Si. Both SiO_2 and SnO_2 have rutile structure, but different lattice parameters, i.e., $a = 4.18 \text{ \AA}$ and $c = 2.66 \text{ \AA}$ for SiO_2 (Baur and Khan, 1971) and $a = 4.74 \text{ \AA}$ and $c = 3.19 \text{ \AA}$ for SnO_2 (Baur, 1956). Our results show that applying compressive strain through alloying does not sufficiently shift the acceptor level to a usable value.

5.2 Computational Details

First-principles calculations based on density functional theory (DFT) were used within a plane-wave basis set as implemented in the VASP code (Kresse and Furthmüller, 1996; Kresse and Hafner, 1994; Kresse and Joubert, 1999). The electron-ion interactions were described by the projector augmented-wave (PAW) method (Blöchl, 1994). The Sn $4d$ and Ga $3d$ states were treated as valence electrons. For the exchange-correlation energy, both generalized gradient approximation (GGA) parameterized by Perdew, Burke, and Ernzerhof (PBE) (Perdew et al., 1996) and hybrid functional proposed by Heyd, Scuseria, and Ernzerhof (HSE) (Heyd et al.,

Table 5.1 The calculated lattice parameters (a and c), internal parameter (u), and cell volume (Ω) of SnO₂ and SiO₂ in the tetragonal rutile structure by using the GGA-PBE and HSE functionals accompanied with the corresponding experimental values.

	GGA-PBE				HSE				Exp.			
	a	c	u	Ω	a	c	u	Ω	a	c	u	Ω
	(Å)	(Å)		(Å ³)	(Å)	(Å)		(Å ³)	(Å)	(Å)		(Å ³)
SnO ₂	4.77	3.22	0.306	73.21	4.74	3.18	0.306	71.55	4.74	3.19	0.307	71.47 ^a
SiO ₂	4.19	2.68	0.306	47.12	4.16	2.66	0.306	46.12	4.18	2.66	0.306	46.54 ^b

^a (Baur, 1956)

^b (Baur and Khan, 1971)

2003) with a mixing parameter of 0.32 were used. The latter yields the calculated band gap of 3.61 eV in agreement with the experimental value of 3.60 eV (Reimann and Steube, 1998). The energy cutoff for expanding the plane wave basis set was set at 306 eV (Kresse and Furthmüller, 1996). The spin polarization was treated for all cases with unpaired electrons. For bulk calculations, the Γ -centered grid scheme was used for k -space integration with a sampling mesh point of $3 \times 3 \times 5$. The calculated lattice parameters for SnO₂ obtained from both GGA-PBE and HSE are summarized in Table 5.1. They are in good agreement with the experimental values. For defect calculations, a supercell approach was employed using a supercell size of 72-atom, i.e., a $2 \times 2 \times 3$ repetition of the 6-atom primitive cell. All atoms in the supercell were allowed to relax until the residue force on each atom became less than 0.025 eV/Å. The chance of Ga substitution for Sn (Ga_{Sn}) could be determined from its formation energy, which is defined by (Janotti and Van de Walle, 2007):

$$E^f(\text{Ga}_{\text{Sn}}^q) = E_{\text{tot}}(\text{Ga}_{\text{Sn}}^q) - E_{\text{tot}}(\text{SnO}_2) + \mu_{\text{Sn}} - \mu_{\text{Ga}} + q(E_F + E_{\text{VBM}}), \quad (5.1)$$

where $E_{\text{tot}}(\text{Ga}_{\text{Sn}}^q)$ is the calculated total energy of a supercell with Ga substitution for Sn in charge state q , $E_{\text{tot}}(\text{SnO}_2)$ is the calculated total energy of a perfect supercell, μ_{Sn} and μ_{Ga} are the atomic chemical potentials described below, and E_F is the Fermi energy referenced to the valence band maximum (VBM) of the perfect cell.

To grow SnO₂ crystal under the thermodynamic equilibrium, it is required that $\mu_{\text{SnO}_2} = \mu_{\text{Sn}} + 2\mu_{\text{O}}$, where μ_{SnO_2} is the total energy of SnO₂ per formula unit, μ_{Sn} and μ_{O} are the atomic chemical potentials for Sn and O, respectively. To prevent the formation of the undesired phases, such as metallic α -Sn and gaseous O₂, the chemical potentials of Sn and O (μ_{Sn} and μ_{O}) are limited to the energy per formula unit of metallic α -Sn and half of the energy of gaseous O₂ molecule ($\mu_{\text{O}} = E_{\text{tot}}(\text{O}_2)/2$), respectively. For the calculations of Ga defects, the chemical potential of Ga (μ_{Ga}) is limited by β -Ga₂O₃ phase to prevent the formation of gallium oxide phase.

For the formation-energy calculations of charged defect by the supercell approach, there is a fictitious interaction arising from the neighboring cells due to periodic boundary conditions. This error can be reduced by applying a finite-size correction to the defect formation energy defined in Eq. (5.1). Here, the finite-size correction scheme was applied (Makov and Payne, 1995);

$$E_{\text{correct}}^f(\text{Ga}_{\text{Sn}}^q) = E^f(\text{Ga}_{\text{Sn}}^q) + \frac{q^2 \alpha}{2\epsilon L}, \quad (5.2)$$

where $E^f(\text{Ga}_{\text{Sn}}^q)$ is the calculated formation energy obtained from Eq. (5.1). The last term on the right hand side is the Madelung energy, where α is the Madelung

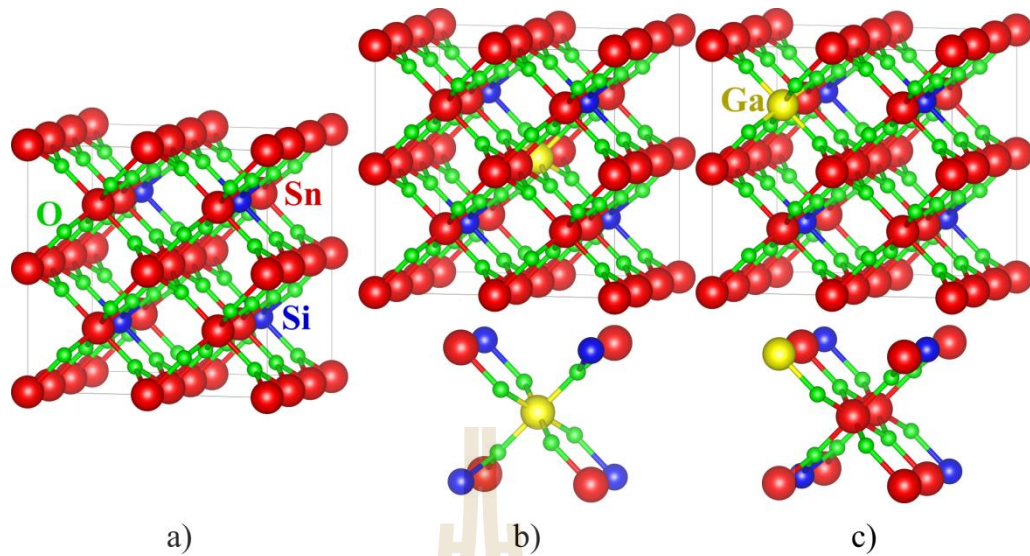


Figure 5.1 Schematic illustration of the structures for $\text{Si}_x\text{Sn}_{1-x}\text{O}_2$ alloy (a), Ga_{Sn} in $\text{Si}_x\text{Sn}_{1-x}\text{O}_2$ alloy at *inside* (b) and *outside* (c) Si-cluster configurations. The red, green, blue, and yellow balls represent Sn, O, Si, and Ga atoms, respectively.

constant, ϵ is the static dielectric constant of material, and L is the linear dimension of the supercell (i.e., $L \sim \Omega^{1/3}$, where Ω is the supercell volume). α and ϵ were set to 2.84 (Leslie and Gillan, 1985) and 12.33 (Young and Frederikse, 1973), respectively. This gives the calculated Madelung energy for a single charge state ($q = -1$ and $+1$) of Ga_{Sn} defect in the 72-atom SnO_2 supercell to be about 0.17 eV. After applying the finite-size correction as mentioned above, the defect transition level associated with the defect in two different charge states, i.e., q_1 and q_2 , could be determined. This level is actually defined as the Fermi-level position at which the formation energies of the defect in the two charge states are equal, i.e.,

$$e(q_1 / q_2) = \frac{E_{\text{correct}}^f(\text{Ga}_{\text{Sn}}^{q_2}) - E_{\text{correct}}^f(\text{Ga}_{\text{Sn}}^{q_1})}{q_2 - q_1}. \quad (5.3)$$

To investigate the effect of compressive strain on the defect transition level associated with Ga_{Sn} defect in SnO_2 , four Sn atoms in a bulk 72-atom SnO_2 supercell were replaced with Si atoms to create $\text{Si}_x\text{Sn}_{1-x}\text{O}_2$ alloy with $x \sim 0.17$. While there are many ways to replace four Sn atoms with Si, in this work, four Si atoms were symmetrically substituted on the Sn's sites, as depicted in Figure 5.1(a). The cell volume of the $\text{Si}_x\text{Sn}_{1-x}\text{O}_2$ alloy was fully optimized. Then, the Ga_{Sn} defect in this alloy was investigated in two different configurations, as illustrated in Figure 5.1(b) and 5.1(c) for the Ga *inside* and *outside* Si-cluster configurations, respectively.

5.3 Results and Discussion

The lattice parameters obtained from both GGA-PBE and HSE functionals are tabulated in Table 5.1 in comparison with the experimental lattice parameters. It can be clearly seen that the calculations with HSE functional give better results when comparing with the experimental values. In addition, the calculated band gap and the heat of formation obtained from HSE functional are 3.61 eV and -6.09 eV, respectively, which are in good agreement with the experimental values of 3.60 eV (Reimann and Steube, 1998) and -5.99 eV (Lavut et al., 1981). However, the calculations with HSE functional take much more computational resources compared to the calculations with GGA-PBE functional. Note that the calculated band gap with GGA-PBE functional is only 1.27 eV, which is much lower than the experimental value due to the well-known DFT problems. Moreover, the VBM and conduction

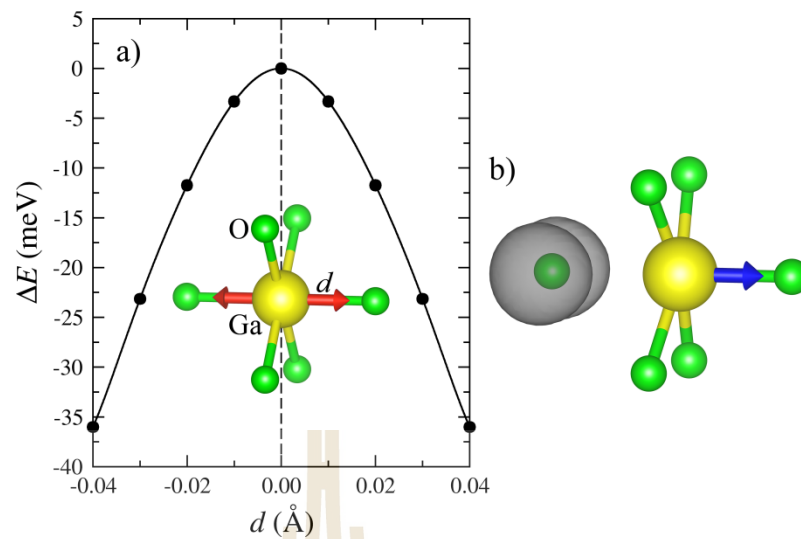


Figure 5.2 (a) The total energy (ΔE) of Ga_{Sn}^0 in bulk SnO_2 as a function of the Ga's displacement (d) near the saddle point. The total energy of the Ga_{Sn}^0 at the *on-center* configuration ($d = 0.00$ Å) is set to be zero and the vertical dashed line marks the mirror symmetry point. (b) Ga atom is moved along the Ga-O bond, as indicated by the blue arrow, until one Ga-O bond appears broken and the total energy is reduced by 0.5 eV. The localized hole states on the oxygen atom nearby Ga_{Sn} are depicted as a gray color.

band minimum positions obtained from GGA-PBE functional are known to be incorrect. Therefore, the HSE functional will be used for further study.

To revisit the study of *p*-type conductivity in Ga-doped SnO_2 , a Ga substitution for Sn (Ga_{Sn}) defects in SnO_2 were reinvestigated. Because Ga has one less valence electron compared to Sn, Ga_{Sn} is expected to be stable in a negative charge state ($\text{Ga}_{\text{Sn}}^{-1}$) and/or neutral charge state (Ga_{Sn}^0) depending on the electron Fermi energy. For $\text{Ga}_{\text{Sn}}^{-1}$, Ga atom prefers to stay on the Sn site surrounded by six

oxygen atoms similar to the geometry of Sn-O bonds in bulk SnO₂. This configuration is called *on-center* configuration. The six Ga-O bond lengths are 2% shorter than the Sn-O bond lengths in the bulk SnO₂. For Ga_{Sn}⁰, Ga in the *on-center* configuration is not the lowest-energy configuration. The formation energy can be lowered by breaking a Ga-O bond and shifting the Ga atom from the *on-center* site. The potential energy curve near the saddle point is illustrated in Figure 5.2(a). The new configuration with five Ga-O bonds is called *off-center* configuration as illustrated in Figure 5.2(b). The energy different between the *on-* and *off-center* configurations is 0.5 eV; indicating that Ga_{Sn}⁰ clearly stables in the *off-center* configuration, or a small-polaron configuration.

When taking into account the proper structural relaxation as explained above, the defect transition level $\epsilon(0/-)$ associated with Ga_{Sn} is ~0.79 eV above the VBM. In addition, the hole states localized on the oxygen atom nearby Ga_{Sn} (see Figure 5.2(b)) also reveal the deep characteristic. This means Ga_{Sn} is indeed a deep acceptor which is in agreement with the result of Scanlon and Watson (Scanlon and Watson, 2012). Based on our results, Ga_{Sn} cannot be a source of *p*-type carriers in SnO₂.

Recently, it has been proposed that compressive strain could shift the deep acceptor levels to shallower values (Sun et al., 2014). It was shown that by applying (hydrostatic) compressive strain to ZnO, the acceptor level of Na_{Zn} became shallower and can be used to improve the *p*-type conductivity. For the case of Ga in SnO₂, the bond compression in the -1 charge state and the configuration distortion in the neutral charge state clearly suggest that the center around Ga prefers compressive strain. In addition, the structural distortion of the neutral charge state (from *on-center* to *off-*

Table 5.2 The calculated parameters of 72-atom SnO₂ with and without alloying with Si atom. L_x , L_y , and L_z are the expanded cell dimensions in relative to the primitive cell parameters, where $L_x = L_y = 2a$ and $L_z = 3c$. The parameters for the alloy are explicitly calculated only for the GGA-PBE case. For HSE calculations, the compression ratio obtained from the GGA-PBE case (−6.22%) is used to calculate the alloy parameters relative to bulk SnO₂ (the cell shape of the alloy is approximated to be a cube, i.e., $L_x = L_y = L_z = \Omega^{1/3}$).

	GGA-PBE		HSE	
	SnO ₂	Si _x Sn _{1-x} O ₂	SnO ₂	Si _x Sn _{1-x} O ₂
$L_x = L_y$ (Å)	9.54	9.37(44)	9.48	9.30
L_z (Å)	9.65	9.37(49)	9.55	9.30
Ω (Å ³)	878.51	823.86	858.62	805.20
$\Delta\Omega$ (%)		−6.22		−6.22

center) results in the energy lowering by 0.5 eV. This energy lowering is partially responsible for the very deep acceptor level. In principle, without this structural relaxation, the acceptor level can be 0.5 eV shallower. By analyzing the structure, application of the compressive strain into the SnO₂ host helps shifting the O neighbors closer to the Ga atom (reducing the strain for the −1 charge state) and at the same time might be sufficient to stop the neutral charge state from distorting to the *off-center* configuration (avoiding the structural distortion energy). Therefore, the compressive strain was applied into SnO₂ by adding another element that crystalizes in the same crystal structure as the host, but with a smaller unit cell volume. Since SiO₂ also has a tetragonal rutile structure with a smaller unit cell volume than that of

SnO₂ as shown in Table 5.1. Therefore, Si atoms were added into SnO₂ forming Si_xSn_{1-x}O₂ alloy by symmetrically replacing four Sn atoms in the SnO₂ supercell by four Si atoms as illustrated in Figure 5.1(a) and re-optimized the cell volume of Si_xSn_{1-x}O₂ alloy. The alloy's volume is explicitly calculated using the GGA-PBE functional. The volume of the alloy is 6.22% smaller than that of SnO₂ as shown in Table 5.2. After alloying, the tetragonal-SnO₂ has the supercell shape transformed into an almost perfect cubic-Si_xSn_{1-x}O₂. As shown in Table 5.1, the ratio between the unit cell volume of pure SnO₂ and pure SiO₂ obtained using the GGA-PBE and HSE functional are almost exactly the same, i.e., ~1.55. Therefore, the same compression ratio, i.e., ~6.22% compression from bulk SnO₂, was assumed for the HSE calculations of Si_xSn_{1-x}O₂ alloy.

To study the effects of compressive strain on the defect transition level associated with Ga_{Sn}, one Sn atom in Si_xSn_{1-x}O₂ alloy was substituted by Ga atom. To test different Sn sites in the alloy, two different configurations were studied; (1) Ga_{Sn} *inside* Si-cluster (Ga_{Sn}ⁱⁿ) and (2) Ga_{Sn} *outside* Si-cluster (Ga_{Sn}^{out}) as shown in Figure 5.1(b) and 5.1(c), respectively. The results showed that the relaxations of the neutral Ga_{Sn} remains the same as the non-strain case and the defect transition levels are still very deep. The levels associated with Ga_{Sn}ⁱⁿ and Ga_{Sn}^{out} are 0.87 eV and 0.71 eV above the VBM, respectively. This indicates that the strain effect is not sufficient to enhance the *p*-type carrier for Ga-doped SnO₂. Even the best case, the acceptor level is reduced by only ~0.1 eV.

Further, to investigate whether the change in the transition levels is mainly due to the effect of compressive strain or the effect of atomic Si, the cell volume of SnO₂

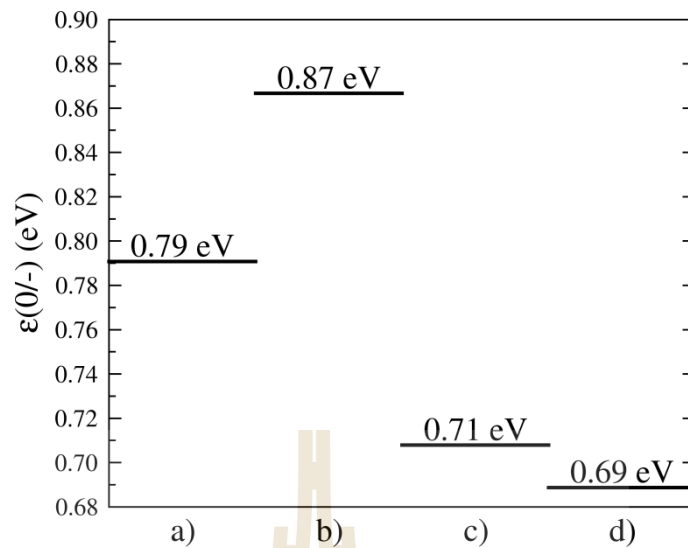


Figure 5.3 Defect transition levels $\epsilon(0/-)$ associated with Ga_{Sn} in four configurations, i.e., (a) bulk SnO_2 , (b) $\text{Si}_x\text{Sn}_{1-x}\text{O}_2$ alloy with *inside* configuration, (c) $\text{Si}_x\text{Sn}_{1-x}\text{O}_2$ with *outside* configuration, and (d) 6.22% compressed bulk SnO_2 . In the plot, the valence band maximum for each configuration is set to be zero.

was directly compressed with the same ratio as mentioned before without alloying with Si and then replaced one Sn atom with Ga to create Ga_{Sn} defect. The results showed that under the compression, the defect transition level is 0.69 eV above VBM. This is about 0.1 eV lower than the uncompressed case. The compressive strain helps to make the acceptor level shallower as expected. However, the effect is too small to be useful as the level remains too deep. The defect transition levels associated with Ga_{Sn} defect in bulk SnO_2 , $\text{Si}_x\text{Sn}_{1-x}\text{O}_2$ alloy, and compressed bulk SnO_2 are shown in Figure 5.3. Because the acceptor levels in all cases remain deep, it can be concluded that Ga_{Sn} cannot be a source of hole carrier in SnO_2 .

5.4 Conclusions

First-principles calculations with GGA-PBE and HSE functionals were performed to study Ga_{Sn} defects in SnO_2 with and without compressive strain. The results revealed that Ga_{Sn} defect acts as a deep acceptor in SnO_2 with the ionization energy of ~ 0.8 eV. Moreover, the compressive strain effect on the acceptor level was investigated. The results showed that by applying the strain of $\sim 6\%$ either by direct compression or alloying with smaller cations (Si), the acceptor level can be lowered but by only about 0.1 eV and the acceptor level still too deep to be useful. Therefore, that Ga could not be the source of hole carriers in SnO_2 .

5.5 References

- Advani, G. N. and Jordan, A. G. (1980). Thin films of SnO_2 as solid state gas sensors. **Journal of Electronic Materials** 9: 29.
- Batzill, M. and Diebold, U. (2005). The surface and materials science of tin oxide. **Progress in Surface Science** 79: 47.
- Baur, W. (1956). Über die verfeinerung der kristallstrukturbestimmung einiger vertreter des rutiltyps: TiO_2 , SnO_2 , GeO_2 und MgF_2 . **Acta Crystallographica** 9: 515.
- Baur, W. H. and Khan, A. A. (1971). Rutile-type compounds. IV. SiO_2 , GeO_2 and a comparison with other rutile-type structures. **Acta Crystallographica Section B** 27: 2133.
- Blöchl, P. E. (1994). Projector augmented-wave method. **Physical Review B** 50: 17953.

- Das, S. and Jayaraman, V. (2014). SnO₂: A comprehensive review on structures and gas sensors. **Progress in Materials Science** 66: 112.
- Fonstad, C. G. and Rediker, R. H. (1971). Electrical properties of high-quality stannic oxide crystals. **Journal of Applied Physics** 42: 2911.
- Heyd, J., Scuseria, G. E., and Ernzerhof, M. (2003). Hybrid functionals based on a screened Coulomb potential. **The Journal of Chemical Physics** 118: 8207.
- Janotti, A. and Van de Walle, C. G. (2007). Native point defects in ZnO. **Physical Review B** 76: 165202.
- Jarzebski, Z. M. and Marton, J. P. (1976a). Physical properties of SnO₂ materials: II. Electrical properties. **Journal of The Electrochemical Society** 123: 299C.
- Jarzebski, Z. M. and Morton, J. P. (1976b). Physical properties of SnO₂ materials: III. Optical properties. **Journal of The Electrochemical Society** 123: 333C.
- Kresse, G. and Furthmüller, J. (1996). Efficiency of ab-initio total energy calculations for metals and semiconductors using a plane-wave basis set. **Computational Materials Science** 6: 15.
- Kresse, G. and Hafner, J. (1994). Norm-conserving and ultrasoft pseudopotentials for first-row and transition elements. **Journal of Physics: Condensed Matter** 6: 8245.
- Kresse, G. and Joubert, D. (1999). From ultrasoft pseudopotentials to the projector augmented-wave method. **Physical Review B** 59: 1758.
- Lavut, E. G., Timofeyev, B. I., Yuldasheva, V. M., Lavut, E. A., and Galchenko, G. L. (1981). Enthalpies of formation of tin (IV) and tin (II) oxides from combustion calorimetry. **The Journal of Chemical Thermodynamics** 13: 635.

- Leslie, M. and Gillan, N. J. (1985). The energy and elastic dipole tensor of defects in ionic crystals calculated by the supercell method. **Journal of Physics C: Solid State Physics** 18: 973.
- Makov, G. and Payne, M. C. (1995). Periodic boundary conditions in *ab initio* calculations. **Physical Review B** 51: 4014.
- Masahiro, N. and Shigeo, S. (1971). Properties of oxidized SnO₂ single crystals. **Japanese Journal of Applied Physics** 10: 727.
- Perdew, J. P., Ernzerhof, M., and Burke, K. (1996). Rationale for mixing exact exchange with density functional approximations. **The Journal of Chemical Physics** 105: 9982.
- Reimann, K. and Steube, M. (1998). Experimental determination of the electronic band structure of SnO₂. **Solid State Communications** 105: 649.
- Ryu, Y. R., Lee, T. S., Lubguban, J. A., Corman, A. B., White, H. W., Leem, J. H., Han, M. S., Park, Y. S., Youn, C. J., and Kim, W. J. (2006). Wide-band gap oxide alloy: BeZnO. **Applied Physics Letters** 88: 052103.
- Samson, S. and Fonstad, C. G. (1973). Defect structure and electronic donor levels in stannic oxide crystals. **Journal of Applied Physics** 44: 4618.
- Scanlon, D. O. and Watson, G. W. (2012). On the possibility of *p*-type SnO₂. **Journal of Materials Chemistry** 22: 25236.
- Singh, A. K., Janotti, A., Scheffler, M., and Van de Walle, C. G. (2008). Sources of electrical conductivity in SnO₂. **Physical Review Letters** 101: 055502.
- Stjerna, B., Granqvist, C. G., Seidel, A., and Häggström, L. (1990). Characterization of rf-sputtered SnO_x thin films by electron microscopy, Hall-effect

measurement, and Mössbauer spectrometry. **Journal of Applied Physics** 68: 6241.

Sun, Y. Y., Abtew, T. A., Zhang, P., and Zhang, S. B. (2014). Anisotropic polaron localization and spontaneous symmetry breaking: Comparison of cation-site acceptors in GaN and ZnO. **Physical Review B** 90: 165301.

Varley, J. B., Janotti, A., Singh, A. K., and Van de Walle, C. G. (2009). Hydrogen interactions with acceptor impurities in SnO₂: First-principles calculations. **Physical Review B** 79: 245206.

Yates, H. M., Evans, P., Sheel, D. W., Nicolay, S., Ding, L., and Ballif, C. (2012). The development of high performance SnO₂:F as TCOs for thin film silicon solar cells. **Surface and Coatings Technology** 213: 167.

Young, K. F. and Frederikse, H. P. R. (1973). Compilation of the static dielectric constant of inorganic solids. **Journal of Physical and Chemical Reference Data** 2: 313.

CHAPTER VI

CONCLUSIONS AND FUTURE RESEARCHS

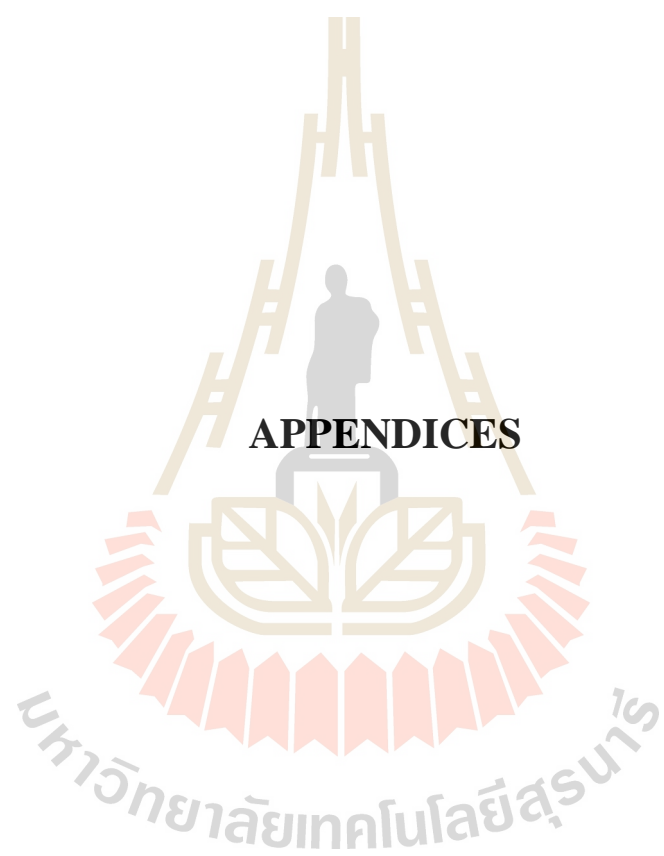
In this thesis, brief theoretical backgrounds related to density functional theory and some approximations are presented in Chapter II. The substitutional defects on both anion's (in Chapter III) and cation's (in Chapter IV and V) sites were thoroughly investigated. In Chapter III, N_O and O_N defects in several metal oxides and metal nitrides were systematically studied to determine the relation of these defects in different metal's group. The calculated results obtained from both LDA and GGA functionals are almost consistent. Our results reveal that these defects can easily incorporate into the host materials under metal-rich growth conditions. In addition, N_O defect in all selected metal oxides always acts as a deep acceptor. Consequently, N_O defect cannot be a source of *p*-type conductivity in metal oxides. In opposite, O_N defect in selected metal nitrides always acts as a shallow donor; donating an electron to the conduction band resulting in an unintentional *n*-type conductivity in metal nitrides. The positions of VBM and defect transition level in the different compounds, in which the metal's cation are in the same group, tend to increase when increasing the metal's atomic size.

For anion substitutional defects, the local structures of the Mg in $Mg_xZn_{1-x}O$ alloy were investigated as reported in Chapter IV. A combination of first-principles calculations and x-ray absorption measurements was used to analyze the Mg environment in the alloy. The deficiency of the fitting results detected in the

measured Mg *K*-edge XANES spectra can be explained by the formation of Mg in other phase having 5-fold coordination called HX structure. The calculated Mg *K*-edge XANES spectrum of the HX structure produces the main peak that nicely fits with the missing part of the measured XANES spectra and should be considered as one of bases of the linear combination fits to determine the phase fraction of Mg in this alloy.

In Chapter V, the Ga acceptor substitutional defects in SnO₂ were revisited to compare the results with the previous literatures. The results revealed that Ga_{Sn} defect acts as a deep acceptor in uncompressed SnO₂. The compressive strain on SnO₂ applied by alloying with Si or reducing the cell volume of SnO₂ cannot make this level shallower. Therefore, doping with Ga cannot produce hole carriers in SnO₂.

Finally, in the future, the electrical and optical properties of various kinds of defects in oxide materials are planned to study by using more accurate hybrid functional for enhancing or improving their properties.



APPENDIX A

THE ASSOCIATED CRYSTAL STRUCTURES OF THE SELECTED METAL OXIDES AND METAL NITRIDES

In Chapter III, for metal oxides, the crystal structures of the alkali metal (group I) oxides, i.e., Li_2O , Na_2O , K_2O , and Rb_2O , are all the antifluorite structure, as shows in Figure A.1(a), in which the positions of the cations and anions are reversed compare to their positions in CaF_2 . The crystal structures of the alkali earth metal (group II) oxides are the wurtzite structure (Figure A.1(b)) for BeO and the rocksalt structure (Figure A.1(c)) for MgO , CaO , and SrO . The crystal structures of the group III metal oxides are the corundum structure (Figure A.1(d)) for Al_2O_3 , the monoclinic structure (Figure A.1(e)) for Ga_2O_3 , and the bixbyite structure (Figure A.1(f)) for In_2O_3 .

For metal nitrides, the crystal structure of Li_3N , which is the only one stable group I nitride, is hexagonal structure (α - Li_3N phase) as shows in Figure A.1(g). The crystal structures of the group II nitrides, i.e., Be_3N_2 , Mg_3N_2 , Ca_3N_2 , and Sr_3N_2 , are all antibixbyite structure as shows in Figure A.1(h) in which similar to Mn_2O_3 but the positions of the cations and anions are reversed. The crystal structures of the group III nitrides are all the wurtzite, similar to BeO structure.

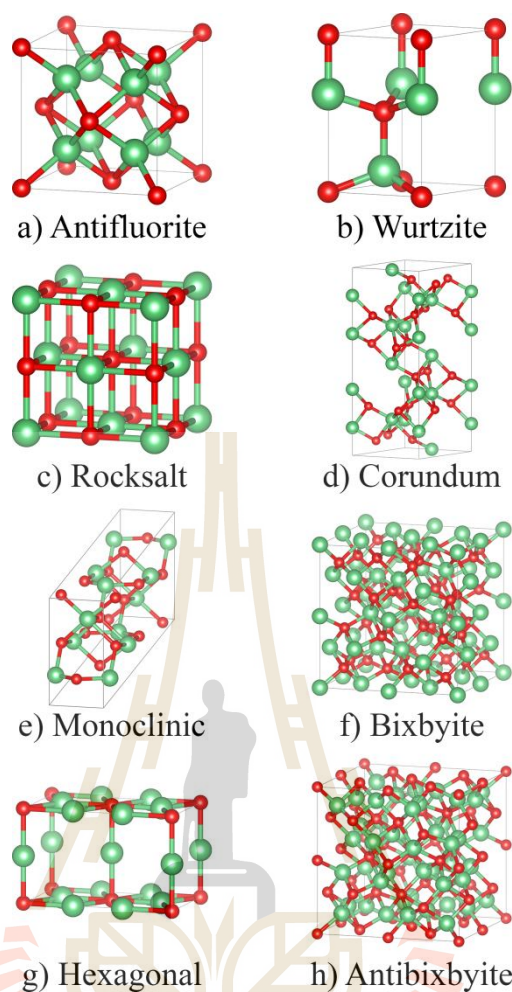


Figure A.1 The associated crystal structures of the selected metal-oxides/nitrides, i.e., (a) the antifluorite structure for Li_2O , Na_2O , K_2O , and Rb_2O , (b) the wurtzite structure for BeO , AlN , GaN , and InN , (c) the rocksalt structure for MgO , CaO , and SrO , (d) the corundum structure for Al_2O_3 , (e) the monoclinic structure for Ga_2O_3 , (f) the bixbyite structure for In_2O_3 , (g) the hexagonal structure for Li_3N , and (h) the antibixbyite structure for Be_3N_2 , Mg_3N_2 , Ca_3N_2 , and Sr_3N_2 . The green (larger) and red (smaller) balls represent the cations (metal atoms) and anions (O for metal oxides and N for metal nitrides) positions, respectively.

APPENDIX B

PUBLICATIONS AND PRESENTATIONS

1. List of publications

Limpijumng, S., Jutimoosik, J., Palakawong, N., Klysubun, W., Nukeaw, J., Du, M. -H., and Rujirawat, S. (2011). Determination of miscibility in MgO-ZnO nanocrystal alloys by x-ray absorption spectroscopy. **Appl. Phys. Lett.** 99: 261901.

Palakawong, N., Jutimoosik, J., T-Thienprasert, J., Rujirawat, S., and Limpijumng, S. (2014). Effect of Mg local structure on Mg *K*-edge XANES spectra of Mg_xZn_{1-x}O alloy: A first-principles study. **Integr. Ferroelectr.** 156: 72.

Pimsorn, P., Palakawong, N., T-Thienprasert, J., Boonchun, A., Reunchan, P., and Limpijumng, S. (2017). Reassignment of O-related infrared absorption peaks in CdSe. **Ceram. Int.** 43: S359.

Palakawong, N., Sun, Y. Y., T-Thienprasert, J., Zhang, S. B., and Limpijumng, S. (2017). Ga acceptor defects in SnO₂ revisited: A hybrid functional study. **Ceram. Int.** 43: S364.

2. List of presentations (oral)

Palakawong, N., T-Thienprasert, J., and Limpijumng, S. (May 2012). First principles study of oxygen defects in AlN. In **Siam Physics Congress 2012**. Phra Nakhon Si Ayutthaya, Thailand: Thai Physics Society.

Palakawong, N., T-Thienprasert, J., and Limpijumnong, S. (March 2013). Nitrogen and oxygen defects in group III (Al, Ga, and In) oxides and nitrides: First-principles calculations. In **Siam Physics Congress 2013**. Chiang Mai, Thailand: Thai Physics Society.

Palakawong, N. and Limpijumnong, S. (April 2013). Concentration effects on XANES of $Mg_xZn_{1-x}O$ alloy: First-principles study. In **RGJ-Ph.D. Congress XIV**. Chon Buri, Thailand: The Thailand Research Fund.

3. List of presentations (poster)

Palakawong, N., Jutimoosik, J., T-Thienprasert, J., Rujirawat, S., and Limpijumnong, S. (July 2011). First principles study of Mg-doped ZnO. In **The 26th International Conference on Defects in Semiconductors**. Nelson, New Zealand: University of Canterbury.

Palakawong, N., T-Thienprasert, J., and Limpijumnong, S. (November 2013). First principles study of oxygen substitutional defect in group III nitrides. In **The 3rd Academic Conference on Natural Science for Master and PhD Students from ASEAN Countries**. Phnom Penh, Cambodia: Royal University of Phnom Penh.

Palakawong, N., Sun, Y. Y., T-Thienprasert, J., Zhang, S. B., and Limpijumnong, S. (December 2016). Ga acceptor defects in SnO_2 revisited: A hybrid functional study. In **The 10th Asian Meeting on Electroceramics**. Taipei, Taiwan: Taiwan Ceramic Society. (the outstanding poster presentation award).

Determination of miscibility in MgO-ZnO nanocrystal alloys by x-ray absorption spectroscopy

Sukit Limpijumnong,^{1,2,3} Jaru Jutimoosik,^{1,2} Nirawith Palakawong,^{1,2} Wantana Klysubun,^{2,4} Jiti Nukeaw,^{4,5} Mao-Hua Du,³ and Saroj Rujirawat^{1,2,4,a)}

¹School of Physics, Suranaree University of Technology, Nakhon Ratchasima 30000, Thailand

²Synchrotron Light Research Institute, Nakhon Ratchasima 30000, Thailand

³Oak Ridge National Laboratory, Oak Ridge, Tennessee 37831, USA

⁴Thailand Center of Excellence in Physics (TheEP Center), Commission on Higher Education, Bangkok 10400, Thailand

⁵College of KMITL Nanotechnology, King Mongkut's Institute of Technology Ladkrabang, Bangkok 10520, Thailand

(Received 17 September 2011; accepted 5 December 2011; published online 27 December 2011)

The local structure of $\text{Mg}_x\text{Zn}_{1-x}\text{O}$ nanocrystals is studied using synchrotron x-ray absorption near edge structures (XANES) over the full range of composition, from $x=0$ to 1. Mg and Zn K -edges XANES measurements allow us to selectively study the local environments around Mg and Zn atoms in these nanocrystalline samples. Our results indicate that, for MgO-ZnO alloys, Zn is highly miscible in the rocksalt domain (i.e., up to ~ 50 at. %) while the miscibility of Mg in the wurtzite domain is much less but is still substantial (i.e., up to ~ 20 at. %). The simulated XANES spectra, based on first principles methods, are consistent with the observed spectra, confirming our finding. Because it is short-ranged and element-specific, the technique is useful for local structure and crystal phase determination of nanostructures, quantum dots, and mixed-phase alloys in general. © 2011 American Institute of Physics. [doi:10.1063/1.3671987]

ZnO in the wurtzite (WZ) structure has a bandgap of ~ 3.3 eV, and MgO in the rocksalt (RS) structure has a bandgap of ~ 7.7 eV. In principle, $\text{Mg}_x\text{Zn}_{1-x}\text{O}$ (MZO) could be engineered to achieve any bandgap in the range of 3.3–7.7 eV, i.e., from blue to UV in optoelectronic applications.¹ MZO thin films and nanostructures can be synthesized by several techniques such as molecular beam epitaxy,² metal organic vapor-phase epitaxy,³ pulsed laser deposition,⁴ RF sputtering,⁵ and chemical based methods.⁶ Reliable characterization of these nanocrystals, which requires modern techniques, is essential for the development of nanoelectronics devices. Advanced functional applications of electronic and optoelectronic materials often require precise tuning of optical and electrical properties. Local crystal structure, along with alloy composition, is an important factor⁷ that determines such properties.

Because the parent compounds of MZO have different natural crystal structures, a structural transition should occur at some critical composition. When the alloys are in polycrystal or nanocrystal forms, the WZ and RS phases can co-exist. These mixed phase MZO alloys exhibit broad band edges and multiple luminescence peaks.^{8,9} Optical and electronic properties of MZO are largely determined by local crystal structure, so, a non-destructive technique to effectively probe the local structure in MZO is needed for engineering these alloys. Since a given atom sees a different local environment in each crystal phase, the mixed phase alloys present a particular challenge to local structure analysis.

The synchrotron x-ray absorption near edge structure (XANES) technique is one of the leading techniques that can provide element-specific information about the local envi-

ronments in nanomaterials.¹⁰ Several groups have reported XANES investigations of MZO alloys.¹¹ However, most of the works have analyzed their results based on the assumption that alloys have either the wurtzite or rocksalt structure. In this letter, the local structure of MZO nanocrystal alloys at various compositions (sampling over the whole composition range) is studied by XANES supported by theoretical simulations, with mixed-phase characteristics fully included. This work applies XANES measurements and element-selective local structure analysis to MZO nanocrystals in particular, while demonstrating the power of the procedure for studying nanostructures in general.

MZO nanocrystal samples were synthesized based on an oxalate-based co-precipitation method.¹² Zinc acetate dehydrate, magnesium acetate tetrahydrate, and oxalic acid dehydrate were used as precursors. First, aqueous solutions of zinc and magnesium acetates were mixed in oxalic acid solution with selected ratios to achieve mixed oxalate precursors $\text{Mg}_x\text{Zn}_{1-x}(\text{C}_2\text{O}_4) \cdot 2\text{H}_2\text{O}$. After that, the precipitates were (1) washed with de-ionized water, (2) dried at 60 °C for 4 h, and (3) heated in air at 550 °C for 24 h. Finally, the resulting MZO nanocrystal samples were kept in a humidity-controlled cabinet at room temperature before characterization. Based on energy dispersive spectroscopy (EDS) measurements (not shown), the Mg mole fractions in our MZO samples are determined to be $x = 0.00, 0.01, 0.04, 0.06, 0.10, 0.15, 0.25, 0.30, 0.35, 0.50, 0.70, 0.80,$ and 0.90, consistent with the fractions used in the preparation process. The UV-Vis absorption measurements have confirmed that the main absorption edges are blue shifted for MZO samples with higher Mg mole fractions.

To gain information about the average crystal structures, samples were first characterized by a traditional x-ray powder diffraction (XRD) technique using BRUKER X-ray

^{a)}Author to whom correspondence should be addressed. Electronic mail: saroj@sut.ac.th.

diffractometer model D 5005 with a Cu K_α source. For the samples with $x \leq 0.06$, only the diffraction peaks associated with WZ structure are observed. For the samples with $x \geq 0.90$, only RS peaks are observed. For compositions in between, peaks of both phases are seen. The wide range of mixed phase nanocrystals has been previously reported.¹³ By using the area under the diffraction peaks, $A(\text{RS})$ and $A(\text{WZ})$, the RS phase fraction $F_{\text{XRD}} = A(\text{RS}) / [A(\text{RS}) + A(\text{WZ})]$, can be estimated for each sample.¹⁴ Broad XRD peaks, indicative of nanometer-sized MZO crystals, were found. From the transmission electron microscope (TEM) micrographs (not shown), the samples with $x \leq 0.06$ contain WZ nanocrystals of size ~ 50 – 100 nm with small phase segregated RS nanocrystals of size ~ 10 nm. The signal from these small RS nanocrystals is overshadowed by the stronger WZ signal in the XRD spectrum, which makes the RS contribution difficult to observe. Another limitation of traditional diffraction techniques, which are not element-selective, is that only the average crystal structure can be studied. The crucial local structures of Mg and Zn atoms cannot be identified via XRD.

To complicate matters, the mixed WZ/RS phase observed in MZO nanocrystals is not merely a phase separation of pure MgO and pure ZnO pure compounds. Rather, Zn atoms can substitute for Mg in RS-MgO, and Mg atoms can substitute for Zn in WZ-ZnO. In contrast to the general belief that MZO alloys prefer to form phase separation into WZ-ZnO and RS-MgO, both WZ and RS sub-nano domains of our samples contain a substantial fraction of Mg and Zn substitutes. Despite these difficulties, we find that XANES techniques, which are sensitive to the local structure surrounding a selected element, are capable of quantitatively determining the local structure of each cation. This suggests that the technique is well-suited for nanostructural characterizations in general.

XANES spectra were obtained at beamline 8 of the Siam Photon Laboratory, Synchrotron Light Research Institute, Thailand, with the storage ring running at 1.2 GeV and with a beam current of 80–120 mA during the measurements.¹⁵ XANES measurements were made in the fluorescence mode using KTP (011) and Ge (220) double crystal monochromators for Mg K -edge (1303 eV) and Zn K -edge (9659 eV), respectively. A 13-element Ge detector was used for detection of x-ray photons emitted from the sample. The x-ray transparent Kapton[®] tape was used to mount the samples. The absolute energy of absorption edges was calibrated by using standard RS MgO and WZ ZnO powders and compared with the literature.¹⁶ All spectra were collected using an energy step of 0.25 eV.

The measured Mg K -edge and Zn K -edge XANES spectra from our MZO nanocrystal samples are shown in Figs. 1(a) and 1(b), respectively. For the Mg K -edge, spectra show a progression from one distinct spectrum ($x = 1.00$) to another ($x = 0.04$). The spectrum of pure MgO ($x = 1.00$) certainly represents the signature of Mg in 6-fold coordination. Because there are only two crystal structures in the samples (WZ and RS), the other distinctive spectrum of the alloy, which is found for nearly pure ZnO ($x = 0.04$, only 4% Mg), must represent the signature of Mg in 4-fold coordination, i.e., Mg substitution for Zn in WZ ZnO. Similarly, the

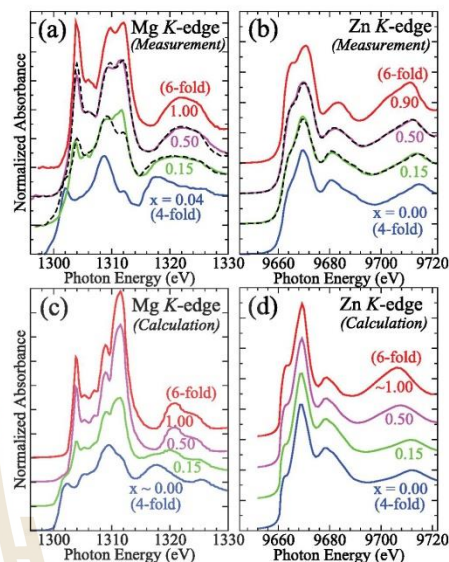


FIG. 1. (Color online) Measured (a) Mg K -edge, (b) Zn K -edge XANES spectra of MZO nanocrystals and simulated (c) Mg K -edge, (d) Zn K -edge XANES spectra of MZO. The number labeled on each spectrum is the Mg mole fraction (x). For the measured spectra of the mixed phase samples, the linear combination fits are shown using dashed lines.

Zn K -edge spectrum of pure ZnO ($x = 0.00$) certainly represents the signature of 4-fold Zn while the other distinctive spectrum, observed for nearly pure MgO ($x = 0.90$, 10% Zn), must represent the signature of 6-fold Zn, i.e., Zn substitution for Mg in RS MgO. Taken together, these XANES spectra seem to give strong evidence that Mg can substitute for Zn site in the WZ phase, and Zn can substitute for Mg site in the RS phase. To test this interpretation, we performed *ab initio* calculations.

We used the FEFF code (version 8.2)¹⁷ to calculate both Mg and Zn K -edges XANES spectra. For the WZ structures, the lattice parameters $a = 3.24$ Å and $c = 5.19$ Å (Ref. 18) are used. For the RS structures, the parameter $a = 4.21$ Å (Ref. 19) is used. Based on our test calculations, variation of metal-oxygen bond lengths by a few percent does not change qualitative spectral features. Therefore, lattice relaxations were not considered in this study. For Zn K -edge calculations, a cluster of 42 atoms (radius of 5.0 Å around the central Zn atom) is used to calculate the self-consistent field (SCF) muffin-tin atomic potentials within the Hedin-Lundqvist exchange potential, and a 144-atom cluster (radius of 7.5 Å) is used for the full multiple scattering (FMS) calculation. For Mg K -edge, the parameters are SCF radius = 7.5 Å (203 atoms) and FMS radius = 8.5 Å (257 atoms). We found that the larger cluster for Mg calculations was needed to obtain reliable results. Also, with this cluster, one avoids the need to introduce an unphysical $Z + 1$ scheme on top of core-hole corrections.²⁰ The calculated spectra for

pure RS MgO (Mg *K*-edge) and WZ ZnO (Zn *K*-edge) are shown as the topmost curve in Fig. 1(c) and bottommost curve in Fig. 1(d), respectively. These spectra compare favorably with the corresponding measured spectra and with available literature. To calculate a 6-fold Zn spectrum (topmost curve in Fig. 1(d)), a calculation of RS MgO is repeated with the absorber Mg atom replaced by a Zn atom. Similarly, a 4-fold Mg spectrum [bottommost curve in Fig. 1(c)] was calculated by substituting the Zn absorber in the WZ ZnO framework by an Mg atom. The calculated spectra are in good agreement with the corresponding measured spectra obtained from the diluted samples; this supports the assumption that (1) Mg atoms in diluted Mg MZO are 4-fold substitutes for Zn atoms in WZ ZnO structure and (2) Zn atoms in diluted Zn MZO are 6-fold substitutes for Mg atoms in RS MgO.

For the mixed phase samples, the measured XANES spectra of each cation can be understood as a linear combination of 4-fold WZ and 6-fold RS spectra of this species. For example, at $x = 0.50$, the sample contains Zn and Mg atoms with an equal molar fraction. The Zn *K*-edge XANES measurement of the sample collectively records the absorption of all Zn atoms in the sample, i.e., both 4-fold and 6-fold Zn atoms. As a result, the spectrum contains features from both the 4-fold and 6-fold Zn spectra. A linear combination fit [dashed curves in Figs. 1(a) and 1(b)] of the spectrum, using the spectra of 4-fold and 6-fold Zn as a basis, reveals the fraction of Zn atoms in the normal 4-fold WZ (0.46) and miscible Zn in 6-fold RS structure (0.56). Table I shows f_{Zn} , which is the fraction of Zn atoms with 6-fold coordination, obtained from the fit for each sample. The exercise can be repeated for the Mg *K*-edge XANES where the contributions of Mg atoms in the normal 6-fold RS and 4-fold WZ structures are obtained. The values of f_{Mg} , the fraction of Mg atoms that have 6-fold coordination, are also shown in Table I. The RS phase fraction based on XANES measurements can be determined from $F_{XANES} = x f_{Mg} + (1 - x) f_{Zn}$. The plots of F_{XANES} and F_{XRD} as a function of Mg content (x) in the sample are shown as solid and dashed curves in Fig. 2, respectively. For the low- and high- x regions, the RS phase

TABLE I. Rocksalt phase fractions of $Mg_xZn_{1-x}O$ nanocrystal alloys obtained by XANES (F_{XANES}) and XRD (F_{XRD}). f_{Mg} and f_{Zn} are the partial phase fractions of Mg and Zn in 6-fold coordination, indicating the fraction of Mg and Zn in RS phase, measured by using Mg and Zn *K*-edge XANES, respectively.

x	f_{Mg}	f_{Zn}	F_{XANES}	F_{XRD}
0.01	0.00	0.00	0.00	0.00
0.04	0.01	0.01	0.01	0.00
0.10	0.15	0.03	0.04	0.05
0.15	0.37	0.07	0.12	0.11
0.25	0.47	0.18	0.25	0.22
0.30	0.56	0.25	0.34	0.34
0.35	0.74	0.33	0.47	0.42
0.50	0.90	0.54	0.72	0.60
0.70	0.97	0.81	0.92	0.84
0.80	0.99	0.92	0.98	0.95
0.90	1.00	1.00	1.00	1.00
1.00	1.00	1.00	1.00	1.00

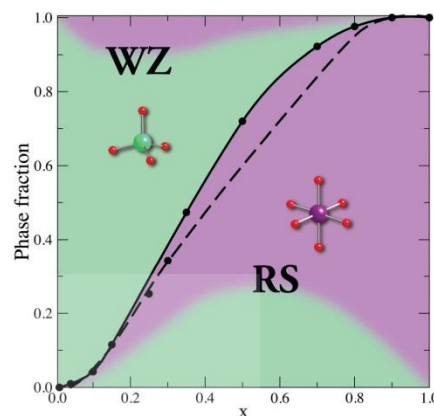


FIG. 2. (Color online) Phase fractions of samples with different Mg contents (x) as determined by XANES (solid curve) and XRD (dashed curve). The area under (above) the thick black curve represents the fraction of RS (WZ) determined by XANES. For example, at $x = 0.50$, the RS fraction is 0.72 and WZ is 0.28. The shadings indicate the cation compositions (magenta (darker) = Mg and green (lighter) = Zn) in each phase.

fraction determined by using XANES and XRD is in a good agreement. However, in the mixed phase region, where there is a substantial amount of miscible Zn atoms (Zn atoms in the RS structure), the phase fraction determined by XANES and XRD is quite different. The phase fractions measured by XRD can only be deemed reliable for large crystals with full phase separation (no Zn in RS and no Mg in WZ). When a large amount of miscibility takes place, the long range periodicity of the crystals is affected. In this case, the values determined by XANES, which is sensitive to only a few neighbors, are expected to be much more reliable.

The area under the curve is associated with the RS phase and the area above the curve (up to 1.00), which is $1 - F_{XANES}$, with the WZ phase. Because the XANES analysis allows not only the determination of the RS fraction but also the individual contribution of each cation species, we are able to show the contributions from each cation species using pattern colors (magenta for Mg and green for Zn). These colors show that the majority cation contribution to the RS phase is Mg while that to the WZ phase is Zn. In finer detail, we can see that Zn atoms are quite miscible in the RS phase (a substantial amount of Zn atoms contributes in the RS phase for x in the mixed phase region) while Mg atoms are much less miscible in the WZ phase. This is consistent with the fact that ZnO has a rather small WZ-RS transformation pressure of 8.22 GPa (Ref. 21) while MgO has a rather large RS-WZ transformation pressure of (negative) 16.2 GPa.²² Each nanocrystal phase with compositions deviating from the global composition would result in different sets of broad optical absorption edges observed in various experiments.^{9,23} These are consistent with the observed abnormal optical band edges with both blue and red shifted from the value interpolated from the trend line. The theoretical counterparts of the mixed phase samples in Figs. 1(c) and

Manuscript published in Applied Physics Letters

261901-4 Limpijumnong *et al.*Appl. Phys. Lett. **99**, 261901 (2011)

1(d) were generated using linear combination of RS and WZ theoretical spectra based on the fitted phase fractions f_{Mg} and f_{Zn} . The prominent features and trends in experimental spectra are well reproduced by the calculated spectra.

In summary, synchrotron XANESs were employed to selectively probe Mg and Zn local structures in MgO-ZnO nanocrystal alloys that contain both WZ and RS crystal structures. We showed that the technique can be used to measure the detailed phase composition of WZ/RS. We did this by first determining the fractions of Mg (or Zn) atoms that are 4-fold and 6-fold coordinated, respectively, and then using this to infer the fractions of Mg (or Zn) atoms that reside in the WZ and RS phases, respectively. In our samples, Zn atoms are more soluble in the RS phase than Mg atoms in the WZ phase, consistent with the relatively small WZ/RS energy difference in ZnO compared to MgO. The experimental finding is well-supported by first principles calculations. The technique, because of its short range and elemental selectivity, can be useful for local structure and crystal phase determination of nanostructures, quantum dots, and mixed-phase alloys in general.

We thank M. F. Smith for proofreading the manuscript. This work is supported by NANOTEC (NN-B-22-DI2-20-51-09) and U.S. Department of Energy, Division of Materials Sciences and Engineering. One of the authors (N.P.) acknowledges the scholarship from the Royal Golden Jubilee Ph.D. Program (Grant No. PHD/0180/2552).

- ¹T. Makino, Y. Segawa, M. Kawasaki, A. Ohtomo, R. Shiroki, K. Tamura, T. Yasuda, and H. Koinuma, *Appl. Phys. Lett.* **78**, 1237 (2001); D. C. Look, *Mater. Sci. Eng., B* **80**, 383 (2001).
²H. Shibata, H. Tampo, K. Matsubara, A. Yamada, K. Sakurai, S. Ishizuka, S. Niki, and M. Sakai, *Appl. Phys. Lett.* **90**, 124104 (2007).
³Y. J. Zeng, Z. Z. Ye, Y. F. Lu, J. G. Lu, L. Sun, W. Z. Xu, L. P. Zhu, B. H. Zhao, and Y. Che, *Appl. Phys. Lett.* **90**, 012111 (2007); W. I. Park, G.-C. Yi, and H. M. Jang, *ibid.* **79**, 2022 (2001).
⁴A. Ohtomo, M. Kawasaki, T. Koida, K. Masubuchi, H. Koinuma, Y. Sakurai, Y. Yoshida, T. Yasuda, and Y. Segawa, *Appl. Phys. Lett.* **72**, 2466 (1998).
⁵C. X. Cong, B. Yao, G. Z. Xing, Y. P. Xie, L. X. Guan, B. H. Li, X. H. Wang, Z. P. Wei, Z. Z. Zhang, Y. M. Lv, D. Z. Shen, and X. W. Fan, *Appl. Phys. Lett.* **89**, 262108 (2006).

- ⁶R. Ghosh and D. Basak, *J. Appl. Phys.* **101**, 023507 (2007); Z. K. Heiba and L. Arda, *Cryst. Res. Technol.* **44**, 845 (2009).
⁷T. Thienprasert, J. Nukeaw, A. Sunghong, S. Porntheeraphat, S. Singkarat, D. Onkaw, S. Rajirawat, and S. Limpijumnong, *Appl. Phys. Lett.* **93**, 051903 (2008); S. Limpijumnong and W. R. L. Lambrecht, *Phys. Rev. Lett.* **86**, 91 (2001).
⁸K. W. Liu, D. Z. Shen, C. X. Shan, J. Y. Zhang, D. Y. Jiang, Y. M. Zhao, B. Yao, and D. X. Zhao, *J. Phys. D: Appl. Phys.* **41**, 125104 (2008); I. Takeuchi, W. Yang, K. S. Chang, M. A. Aronova, T. Venkatesan, R. D. Vispute, and L. A. Bendersky, *J. Appl. Phys.* **94**, 7336 (2003).
⁹S. Choojun, R. D. Vispute, W. Yang, R. P. Sharma, T. Venkatesan, and H. Shen, *Appl. Phys. Lett.* **80**, 1529 (2002).
¹⁰C. Lamberti, *Surf. Sci. Rep.* **53**, 1 (2004); M. F. Smith, K. Setwong, R. Tongpool, D. Onkaw, S. Na-phattalung, S. Limpijumnong, and S. Rajirawat, *Appl. Phys. Lett.* **91**, 142107 (2007); S. Limpijumnong, M. F. Smith, and S. B. Zhang, *ibid.* **89**, 222113 (2006).
¹¹T. Mizoguchi, A. Seko, M. Yoshiya, H. Yoshida, T. Yoshida, W. Y. Ching, and I. Tanaka, *Phys. Rev. B* **76**, 195125 (2007); J. W. Chiou, H. M. Tsai, C. W. Pao, K. P. K. Kumar, S. C. Ray, F. Z. Chien, W. F. Pong, M. H. Tsai, C. H. Chen, H. J. Lin, J. J. Wu, M. H. Yang, S. C. Liu, H. H. Chiang, and C. W. Chen, *Appl. Phys. Lett.* **89**, 043121 (2006); J. W. Chiou, H. M. Tsai, C. W. Pao, F. Z. Chien, W. F. Pong, C. W. Chen, M. H. Tsai, J. J. Wu, C. H. Ko, H. H. Chiang, H. J. Lin, J. F. Lee, and J. H. Guo, *J. Appl. Phys.* **104**, 013709 (2008).
¹²Y.-I. Kim, K. Page, and R. Seshadri, *Appl. Phys. Lett.* **90**, 101904 (2007); A. S. Risbud, N. A. Spaldin, Z. Q. Chen, S. Stemmer, and R. Seshadri, *Phys. Rev. B* **68**, 205202 (2003).
¹³G. Lu, I. Lieberwirth, and G. Wegner, *J. Am. Chem. Soc.* **128**, 15445 (2006).
¹⁴D. Brandon and W. D. Kaplan, *Microstructural Characterization of Materials* (John Wiley & Sons, Ltd, Hoboken, NJ, 2008), pp. i.
¹⁵W. Klysubun, P. Sombunchoo, N. Wongprachanukul, P. Tarawarakarn, S. Klinkhieo, J. Chairapra, and P. Songsiririthigul, *Nucl. Instrum. Methods Phys. Res. A* **582**, 87 (2007).
¹⁶P. Luches, S. D'Addato, S. Valeri, E. Groppo, C. Prestipino, C. Lamberti, and F. Boscherini, *Phys. Rev. B* **69**, 045412 (2004); I. Tanaka, T. Mizoguchi, and T. Yamamoto, *J. Am. Ceram. Soc.* **88**, 2013 (2005); M. Kunisu, I. Tanaka, T. Yamamoto, T. Suga, and T. Mizoguchi, *J. Phys.: Condens. Matter* **16**, 3801 (2004).
¹⁷A. L. Ankudinov, B. Ravel, J. J. Rehr, and S. D. Conradson, *Phys. Rev. B* **58**, 7565 (1998).
¹⁸F. Decremps, F. Datchi, A. M. Saitta, A. Polian, S. Pascarelli, A. Di Cicco, J. P. Itié, and F. Baudelet, *Phys. Rev. B* **68**, 104101 (2003).
¹⁹A. R. Oganov, M. J. Gillan, and G. D. Price, *J. Chem. Phys.* **118**, 10174 (2003).
²⁰K. Nakanishi and T. Ohta, *J. Phys.: Condens. Matter* **21**, 104214 (2009).
²¹S. Limpijumnong and S. Jungthawan, *Phys. Rev. B* **70**, 054104 (2004).
²²S. Limpijumnong and W. R. L. Lambrecht, *Phys. Rev. B* **63**, 104103 (2001).
²³J. L. Morrison, J. Huso, H. Hoek, E. Casey, J. Mitchell, L. Bergman, and M. G. Norton, *J. Appl. Phys.* **104**, 123519 (2008).

Effects of Mg Local Structure on Mg K-edge XANES Spectra of $\text{Mg}_x\text{Zn}_{1-x}\text{O}$ Alloy: A First-principles Study

NIRAWITH PALAKAWONG,^{1,2} JARU JUTIMOOSIK,¹
 JIRAROJ T-THIENPRASERT,^{2,3} SAROJ RUJIRAWAT,^{1,2}
 AND SUKIT LIMPIJUMNONG^{1,2,*}

¹School of Physics and NANOTEC-SUT Center of Excellence on Advanced Functional Nanomaterials, Suranaree University of Technology, Nakhon Ratchasima 30000, Thailand

²Thailand Center of Excellence in Physics, Commission on Higher Education, Bangkok 10400, Thailand

³Department of Physics, Kasetsart University, Bangkok 10900, Thailand

Previously, the measured synchrotron x-ray absorption near-edge spectroscopy (XANES) spectra of $\text{Mg}_x\text{Zn}_{1-x}\text{O}$ alloy (MZO) samples were fitted by using two crystal structure models, i.e., four-fold wurtzite and six-fold rocksalt, with limited success [Appl. Phys. Lett. 99, 261901 (2011)]. For Zn K-edge, the two bases were sufficient for fitting the XANES spectra of intermediate alloy compositions; indicating that majority of the Zn atoms are either four-fold or six-fold coordinated. However, for Mg K-edge, clear deficiency of the fitting can be detected for the intermediate alloy compositions. In this work, first-principles calculations based on density functional theory were carried out to examine other plausible forms of Mg in the alloy. Based on our results, we suggested that the deficiency of the fitting results on Mg K-edge could be attributed to the formation of an unbuckled wurtzite (HX) structure, where Mg atoms are five-fold coordinated. For pure MgO, the HX structure was predicted to be stable under certain tensile strain conditions [Phys. Rev. B 77, 024104 (2008)].

Keywords $\text{Mg}_x\text{Zn}_{1-x}\text{O}$ alloy (MZO); XANES spectra; first-principles calculations

1. Introduction

$\text{Mg}_x\text{Zn}_{1-x}\text{O}$ alloy (MZO) is an alloy between zinc oxide (ZnO) and magnesium oxide (MgO). MZO has been widely studied due to its special optical properties [1–3]. Due to a wide difference in the bandgap of wurtzite (WZ) ZnO and rocksalt (RS) MgO, i.e., ~ 3.3 eV and ~ 7.8 eV [4], respectively, the bandgap of this alloy can be tuned to any value in the range of 3.3–7.8 eV, depending on the Mg mole fraction (x) [5, 6]. Because of the difference in the microscopic structures of WZ-ZnO versus RS-MgO, the microscopic structures of MZO are generally believed to be a mixture of the two structures, depending on the mole

Received July 23, 2013; in final form January 12, 2014.

*Corresponding authors. E-mail: sukit@sut.ac.th

Color versions of one or more of the figures in the article can be found online at www.tandfonline.com/ginf.

Manuscript published in Integrated Ferroelectrics

Mg K-edge XANES Spectra of Mg_xZn_{1-x}O

[229]/73

fraction. Previous studies [7] shown that the structure of MZO is WZ when $x < 0.40$. For $0.40 < x < 0.60$, MZO contains a mixture of WZ and RS structures. For $x > 0.60$, the structure of MZO is completely changed to RS.

Our previously work [8] showed that the Zn *K*-edge x-ray absorption near-edge spectroscopy (XANES) spectra of MZO at all compositions can be described well using only two local structure models, *i.e.*, four-fold coordinated from the WZ structure and six-fold coordinated from the RS structure. This indicates that majority of the Zn atoms are either four-fold or six-fold coordinated. However, for Mg *K*-edge XANES, the deficiency of the fitting results using two local structure models, *i.e.*, four- and six-fold coordinated Mg, can be detected. This suggested other form(s) of Mg in the sample and additional bases, beside the four- and six-fold Mg, should be included in the fit. There are several potential reasons that the two bases of Mg are insufficient to fit the MZO XANES. (1) There might be other favorable forms of Mg defects beside Mg substitute for Zn (Mg_{Zn}). (2) Mg_{Zn} might prefer to bind with specific native defect(s); forming complex defects that have different XANES features from an isolated Mg_{Zn}. (3) Above the diluted limit, Mg_{Zn} in WZ-ZnO might prefers to cluster and the XANES features of clustered Mg_{Zn} could be different from the diluted Mg_{Zn}. (4) In the WZ structure, Mg could form a five-fold coordinated local structure known as unbuckled WZ or HX structure [8].

In this work, first-principles density functional calculations were employed to investigate above mentioned potential reasons. Based on the formation energy calculations, the clustering of Mg_{Zn}, other potential forms of Mg defects, and the formation of complex defects between Mg_{Zn} and native defects were investigated. The interested Mg structures were used to generate the calculated XANES using first principles XAS software called FEFF [9, 10].

2. Computational Details

We used first-principles calculations based on density functional theory (DFT) within the local density approximation (LDA) [11]. The electron-ion interactions were treated by the projector augmented wave (PAW) method as implemented in the Vienna *ab initio* simulation package (VASP) codes [12–14]. The energy cutoff of 500 eV for the plane-wave basis set was used. The calculated lattice parameters ($a = 3.21$ Å, $c = 5.15$ Å, and $u = 0.38$) of WZ-ZnO are in good agreement with the experimental values ($a = 3.25$ Å, $c = 5.21$ Å, and $u = 0.38$) [15]. For bulk calculations, our calculated bandgap of WZ-ZnO is 1.84 eV obtained at the special *k*-point. This value is lower than the experimental bandgap of 3.30 eV due to the well-known problem in LDA approximation.

For defect calculations, a supercell approach with a 96-atom supercell was performed. The Monkhorst-Pack scheme with the sampling mesh points of $2 \times 2 \times 2$ was used for *k*-space integration [16]. The potential existence of a specific defect could be determined by its formation energy, which is defined by:

$$E^f(D, q) = E_{tot}(D, q) - E_{tot}(0) + \sum \Delta n_x \mu_x + q(E_F + E_{VBM}), \quad (1)$$

where $E_{tot}(D, q)$ is the calculated total energy of a supercell with defect *D* in a charge state *q*, $E_{tot}(0)$ is the calculated total energy of a perfect supercell, Δn_x is the number of atoms from the species *x* ($x = \text{Mg}, \text{Zn}, \text{and O}$) being added to a supercell, from its respective reservoir with chemical potential μ_x , to form the defect cell, E_F is the Fermi level referenced to the valence band maximum (E_{VBM}) at the special *k*-point (following

Ref. [17]). To grow a single crystal ZnO in the thermodynamic equilibrium, it is required that $\mu_{\text{ZnO}} = \mu_{\text{Zn}} + \mu_{\text{O}}$, where μ_{ZnO} is the total energy of WZ-ZnO per molecular formula. The upper limits for μ_{Zn} and μ_{O} are the energies per atom of metallic Zn and gaseous O_2 ($\mu_{\text{O}} = E_{\text{tot}}[\text{O}_2]/2$). For defects involving Mg, the chemical potential of Mg (μ_{Mg}) was limited by RS-MgO under both Zn- and O-rich growth conditions, *i.e.*, $\mu_{\text{Mg}} = \mu_{\text{MgO}} - \mu_{\text{O}}$.

To simulate XANES spectra, the optimized structure, relaxed based on first principles calculation using the VASP codes, were used as an input for the FEFF codes. The FEFF codes utilize a full multiple scattering approach, which is based on *ab-initio* overlapping muffin-tin potentials. The muffin-tin potentials were obtained using self-consistent calculations with the Hedin-Lundqvist exchange-correlation function [18]. The self-consistent calculations were performed including all atoms within the sphere radius 5.50 Å around the selected absorber atom. The full multiple scattering calculations including all possible paths were employed for all atoms within the larger cluster radius of 8.40 Å.

3. Results and Discussion

3.1 Native Defects and Mg Defects in WZ-ZnO

As mentioned in the previous section, the existence of defects, including both native and Mg-related defects, depends on their formation energies that can be calculated using the supercell approach. In addition, for native defects, we could compare our results with the literatures to give an insight on the reliability of our calculations.

For simplification, in Fig. 1, we show only the important native defects in ZnO, *i.e.*, Zn vacancy (V_{Zn}), O vacancy (V_{O}), Zn interstitial (Zn_i), and O interstitial (O_i). Our calculated results are in a reasonable agreement with the previous work [19]. As can be seen from the slopes of the formation energy plots in Fig. 1, V_{Zn} is a multicharge deep acceptor with two transition levels at $\varepsilon(0/1^-) = 0.26$ eV and $\varepsilon(1-/2^-) = 0.31$ eV, V_{O} is a deep double donor with the 2+/0 transition level at $\varepsilon(2+/0) = 0.87$ eV, and Zn_i is a shallow donor. For O_i , there are two possible configurations: (1) O_i binding with the host O atom to form O_2 -like molecule, called $\text{O}_i(\text{split})$ and (2) O_i sitting in the octahedral site, called $\text{O}_i(\text{oct})$ as described in Ref. [19]. While $\text{O}_i(\text{split})$ is a neutral defect without any transition level, $\text{O}_i(\text{oct})$ is a deep multicharge acceptor with two transition levels at $\varepsilon(0/1^-) = 0.26$ eV and $\varepsilon(1-/2^-) = 0.68$ eV. Under Zn-rich conditions, V_{O} has the lowest formation energy throughout the entire possible Fermi energy range. Under O-rich conditions, the formation energy of V_{Zn} is the lowest for the Fermi energy above 0.6 eV and $\text{O}_i(\text{split})$ becomes the lowest energy defect for the Fermi energy below 0.6 eV. These suggest that V_{O} , V_{Zn} and $\text{O}_i(\text{split})$ are potential defects that could form under those specific growth conditions.

For Mg defects in WZ-ZnO, we paid special attentions to two forms of Mg, *i.e.*, (1) Mg substitution on the Zn site (Mg_{Zn}) and (2) interstitial Mg (Mg_i). The calculations showed that Mg_{Zn} is a neutral defect whereas Mg_i , where the Mg atom prefers the octahedral site in a similar way as Zn_i , is a shallow double donor. As can be seen in Fig. 1, the formation energy of Mg_{Zn} is lower than that of Mg_i at all Fermi energies except under Zn-rich growth condition where Mg_i turns lower for the Fermi level near the VBM. Because WZ-ZnO is known to be *n*-type semiconductor, which means that the Fermi-level is always near the CBM, it is quite safe to conclude that Mg_{Zn} is the most stable form of Mg defects under both Zn- and O-rich growth conditions with a very low formation energy. Based on these results, Mg_i is unlikely to be the missing form of Mg observed in the XANES measurements of MZO.

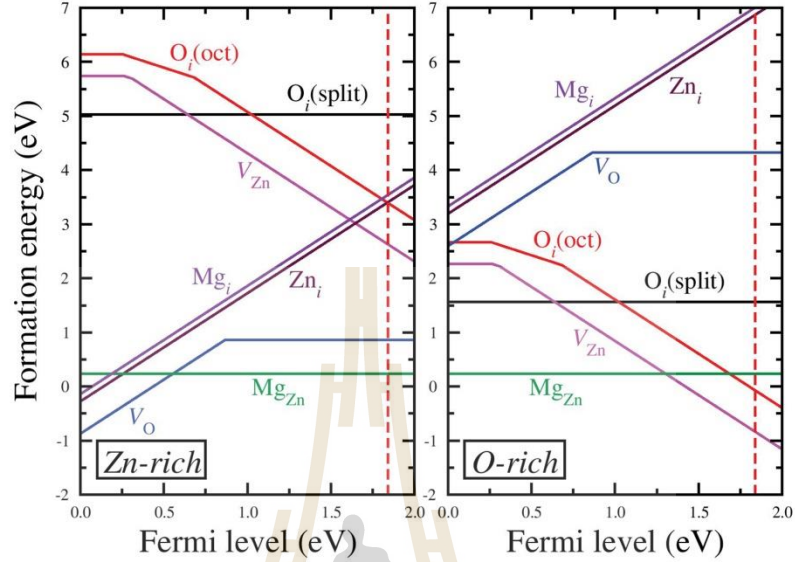


Figure 1. The illustration of formation energies of native defects and Mg defects in ZnO as a function of Fermi level calculated under Zn-rich (left panel) and O-rich (right panel) growth conditions. The slope of each line indicates the charge state of the defect. The Fermi level, referenced to the (special k -point) VBM of bulk, is shown up to the calculated band gap at the special k -point (the vertical dashed line).

3.2 Formation of Defect Complexes between Mg Defects and Native Defects in WZ-ZnO

As described above, Mg prefers to form Mg_{Zn} . The next step is to evaluate whether Mg_{Zn} can bind with another native defect to form a complex defect, for examples, $Mg_{Zn}-V_O$, $Mg_{Zn}-V_{Zn}$, and $Mg_{Zn}-Mg_i$. The binding energy of a complex defect is defined as

$$E_b(Mg_{Zn} - D) = [E^f(Mg_{Zn}) + E^f(D)] - E^f(Mg_{Zn} - D), \quad (2)$$

where $E_b(Mg_{Zn} - D)$ is the binding energy of the complex defect between Mg_{Zn} and defect D , the first two terms are the formation energies of individual Mg_{Zn} and defect D , and $E^f(Mg_{Zn} - D)$ is the formation energy of the complex between Mg_{Zn} and defect D . Here, D can be V_O , V_{Zn} , or Mg_i . The minimum requirement for the complex defect to form is $E_b(Mg_{Zn} - D)$ has to be positive. Based on our calculations (not shown here), we found that the binding energies between Mg_{Zn} and above mentioned native defects (V_O , V_{Zn} , and Mg_i) are all negative, in other words, they are not bound. Therefore, we can rule out the complex defects between Mg_{Zn} and native defects as the missing form of Mg observed in the XANES measurements of MZO.

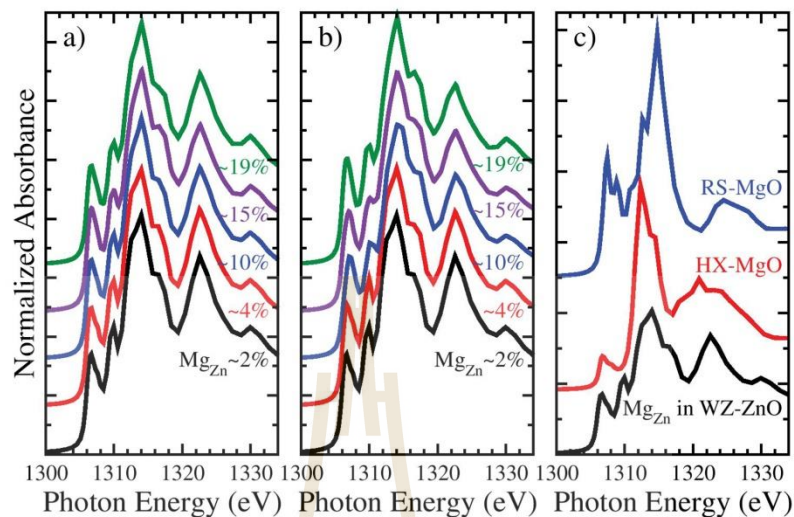


Figure 2. Calculated Mg *K*-edge XANES spectra of Mg_{Zn} in WZ-ZnO (a) with random configurations and (b) with cluster configurations at different Mg concentrations. (c) Calculated Mg *K*-edge XANES spectrum of MgO in the HX structure compared to that of MgO in the RS structure (upper curve) and Mg_{Zn} in WZ-ZnO (lower curve).

3.3 Clustering of Mg_{Zn} in WZ-ZnO

It is possible that Mg_{Zn} might prefer to cluster together. To evaluate the formation of Mg clusters in MZO, we performed two sets of calculations. Starting from pure ZnO, (1) we randomly replace Zn atoms by Mg atoms in WZ-ZnO and (2) we intentionally replace Zn atoms by Mg atoms in WZ-ZnO to form Mg_{Zn} cluster, *i.e.*, placed Mg_{Zn} next to each other. Then, we calculate the total energies from these two cases and compare to determine which one is more stable. We found that the random cases always give lower formation energy than the corresponding clustered cases. This means that Mg_{Zn} cluster is not preferable to form in WZ-ZnO. We performed our calculations using different Mg concentrations, *i.e.*, 2%, 4%, 10%, 15%, and 19%.

Although, our calculated formation energies shown that Mg_{Zn} prefers to stay away from each other as well as away from other native defects, it is still interesting to see how the clustering, which places other Mg atoms as second neighbors, affects the XANES features. The calculated XANES spectra of Mg_{Zn} in the cluster form (average all Mg in the cluster) comparing with the diluted case (single Mg_{Zn} in ZnO) is shown in Fig. 2. As expected, all spectra either in the random cases or the cluster cases at all concentrations are very similar. This is because of the analogous in the local structure around Mg atoms and the differences between them take place only at the second neighbors and beyond.

These calculations showed that Mg_{Zn} are not preferred to cluster and even if they are clustered their XANES features would still be more or less the same as the diluted case.

3.4 The Five-fold Mg_{zn}

Previous first principles total energy calculations on homogeneous phase transformation between WZ and RS MgO have revealed that the HX phase is another stable form of MgO under certain tensile stress conditions [20]. If one starts the calculation from the WZ MgO and keep the volume fixed (so that the structure would not spontaneously relax back to the denser RS phase) but allow full cell shape relaxation, all the buckled [0001] planes would turn to a flat plane; making the Mg atom form five-fold bonding with the surrounding O atoms and the c/a ratio reduces from ~ 1.63 of the WZ structure to ~ 1.2 of the HX structure. Therefore, it is highly plausible that, when Mg substitutes for Zn in WZ ZnO, Mg might form a five-fold coordination local structure with the surrounding O. To calculate the XANES spectrum of five-fold Mg, we calculate the HX MgO using the VASP codes and optimized the structure (our calculated crystal parameters are in good agreement with the literature [20]). After that, we use FEFF to calculate the Mg K -edge XANES spectrum using the crystal structure obtained from VASP. The calculated XANES spectrum is illustrated in Fig. 2c. The features of HX spectrum are significantly differed from that of four- and six-fold Mg with a distinctive peak (at ~ 1314 eV) centering at the position in between the main peaks of the four- and six-fold Mg. Looking back at the fit results (Fig. 1a of Ref. 8) of MZO with $x = 0.15$, we can see that the main deficiency (the disagreement between the actual measurement and the fit) appears at ~ 1312 eV or between the main peaks of the four- and six-fold spectra. Therefore, a big improvement can be expected by including the spectrum of five-fold Mg in the fit. However, there is currently no experimental XANES spectrum of HX structure for using in the actual fit. Nevertheless, we believe that our results served as compelling evidence that the missing Mg in the previous fit should be five-fold Mg.

4. Conclusions

Using first-principles calculations, Mg defects and native defects in wurtzite (WZ) ZnO have been studied to find the plausible forms of Mg in $Mg_xZn_{1-x}O$ alloy (MZO) beside the four-fold and six-fold coordinated Mg that are the normal cation coordination in WZ and rocksalt (RS) structures, respectively. The calculated formation energies confirmed that, in WZ-ZnO, the Mg substituted for Zn (Mg_{zn}), *i.e.*, four-fold Mg, is the most stable form and interstitial Mg (Mg_i) has a high formation energy; making it unlikely to form. Moreover, our total energy calculations shown that Mg_{zn} is an electrically neutral defect and does not prefer to bind with any of the native defects. In addition, Mg_{zn} prefers to stay separated from each other, *i.e.*, they do not want to form Mg clusters. For the measured Mg K -edge XANES spectra, which indicate another form of Mg beside the four-fold and six-fold coordinated Mg, we assigned the missing form of Mg to a five-fold Mg. The five-fold Mg is the normal cation coordination in HX or unbuckled WZ structure. The calculated Mg K -edge XANES spectrum of the five-fold Mg gives the main peak that nicely fits with the missing part of the measured XANES.

Funding

This work was partially supported by NANOTEC, NSTDA (Thailand) through its Center of Excellence Network program. One of the authors (NP) was supported by the Thailand Research Fund through the Royal Golden Jubilee Ph. D. Program (Grant No. PHD/0180/2552).

References

1. A. Ohtomo, M. Kawasaki, T. Koida, K. Masubuchi, H. Koinuma, Y. Sakurai, Y. Yoshida, T. Yasuda, and Y. Segawa, $\text{Mg}_x\text{Zn}_{1-x}\text{O}$ as a II-VI widegap semiconductor alloy. *Appl. Phys. Lett.* **72**, 2466 (1998).
2. G.-h. Ning, X.-p. Zhao, and J. Li, Structure and optical properties of $\text{Mg}_x\text{Zn}_{1-x}\text{O}$ nanoparticles prepared by sol-gel method. *Opt. Mater.* **27**, 1 (2004).
3. N. B. Chen, and C. H. Sui, Recent progress in research on $\text{Mg}_x\text{Zn}_{1-x}\text{O}$ alloys. *Mat. Sci. Eng. B* **126**, 16 (2006).
4. W. Yang, R. D. Vispute, S. Choopun, R. P. Sharma, T. Venkatesan, and H. Shen, Ultraviolet photoconductive detector based on epitaxial $\text{Mg}_{0.34}\text{Zn}_{0.66}\text{O}$ thin films. *Appl. Phys. Lett.* **78**, 2787 (2001).
5. F. Capasso, Band-Gap Engineering: From Physics and Materials to New Semiconductor Devices. *Science* **235**, 172 (1987).
6. T. Makino, Y. Segawa, M. Kawasaki, A. Ohtomo, R. Shiroki, K. Tamura, T. Yasuda, and H. Koinuma, Band gap engineering based on $\text{Mg}_x\text{Zn}_{1-x}\text{O}$ and $\text{Cd}_y\text{Zn}_{1-y}\text{O}$ ternary alloy films. *Appl. Phys. Lett.* **78**, 1237 (2001).
7. L. A. Bendersky, I. Takeuchi, K. S. Chang, W. Yang, S. Hullavarad, and R. D. Vispute, Microstructural study of epitaxial $\text{Zn}_{1-x}\text{Mg}_x\text{O}$ composition spreads. *J. Appl. Phys.* **98**, 083526 (2005).
8. S. Limpijumong, J. Jutimoosik, N. Palakawong, W. Klysubun, J. Nukeaw, M.-H. Du, and S. Rujirawat, Determination of miscibility in MgO-ZnO nanocrystal alloys by x-ray absorption spectroscopy. *Appl. Phys. Lett.* **99**, 261901 (2011).
9. A. L. Ankudinov, B. Ravel, J. J. Rehr, and S. D. Conradson, Real-space multiple-scattering calculation and interpretation of x-ray-absorption near-edge structure. *Phys. Rev. B* **58**, 7565 (1998).
10. A. L. Ankudinov, C. E. Bouldin, J. J. Rehr, J. Sims, and H. Hung, Parallel calculation of electron multiple scattering using Lanczos algorithms. *Phys. Rev. B* **65**, 104107 (2002).
11. C. Stampfl, and C. G. Van de Walle, Density-functional calculations for III-V nitrides using the local-density approximation and the generalized gradient approximation. *Phys. Rev. B* **59**, 5521 (1999).
12. P. E. Blochl, Projector augmented-wave method. *Phys. Rev. B* **50**, 17953 (1994).
13. G. Kresse, and J. Furthmüller, Efficiency of ab-initio total energy calculations for metals and semiconductors using a plane-wave basis set. *Comp. Mater. Sci.* **6**, 15 (1996).
14. G. Kresse, and D. Joubert, From ultrasoft pseudopotentials to the projector augmented-wave method. *Phys. Rev. B* **59**, 1758 (1999).
15. O. Madelung, *Semiconductors - Basic Data*, Springer (1996).
16. H. J. Monkhorst, and J. D. Pack, Special points for Brillouin-zone integrations. *Phys. Rev. B* **13**, 5188 (1976).
17. C. G. Van de Walle, and J. Neugebauer, First-principles calculations for defects and impurities: Applications to III-nitrides. *J. Appl. Phys.* **95**, 3851 (2004).
18. L. Hedin, and B. I. Lundqvist, Explicit local exchange-correlation potentials. *J. Phys. C: Solid State* **4**, 2064 (1971).
19. A. Janotti, and C. G. Van de Walle, Native point defects in ZnO . *Phys. Rev. B* **76**, 165202 (2007).
20. S. Limpijumong, and W. R. L. Lambrecht, Theoretical study of the relative stability of wurtzite and rocksalt phases in MgO and GaN . *Phys. Rev. B* **63**, 104103 (2001).



Reassignment of O-related infrared absorption peaks in CdSe



Pimpika Pimsorn^{a,b,c}, Nirawith Palakawong^{a,b,c}, Jiraroj T-Thienprasert^{c,d,*}, Adisak Boonchun^d, Pakpoom Reunchan^d, Sukit Limpijumong^{a,b,c}

^a School of Physics and NANOTEC-SUT Center of Excellence on Advanced Functional Nanomaterials, Suranaree University of Technology, Nakhon Ratchasima 30000, Thailand

^b Synchrotron Light Research Institute, Nakhon Ratchasima 30000, Thailand

^c Thailand Center of Excellence in Physics (ThEP Center), Commission on Higher Education, Bangkok 10400, Thailand

^d Department of Physics, Faculty of Science, Kasetsart University, Bangkok 10900, Thailand

ARTICLE INFO

Keywords:

First-principles calculations

DFT

Defect

LVM

ABSTRACT

Upon their observation in 2008, the IR absorption peaks at 1094.11, 1107.45, and 1126.33 cm^{-1} of O-doped wurtzite-CdSe sample have been proposed to associate with the local vibrational modes (LVM) of oxygen – vacancy Cd complex defect ($\text{O}_{\text{Se}}-\text{V}_{\text{Cd}}$) (Chen et al., 2008) [8]. Later, first principles calculations by T-Thienprasert et al. reveal that the LVMs of the $\text{O}_{\text{Se}}-\text{V}_{\text{Cd}}$ complex defect are actually at 223, 507 and 517 cm^{-1} not in the 1000 cm^{-1} range (T-Thienprasert et al., 2012) [14]; suggesting that the assignment has to be revised. Bastin et al. identified the source of the modes to be a sulfur-oxygen defect complex (Bastin et al., 2014) [11] by intentionally varied the amount of S and analyzed the isotope abundances of S and O from the measurements. In this work, sulfur-oxygen defect complexes in wurtzite-CdSe were studied by first principles calculations. It is found that SO_2 energetically prefers to substitute on the Se site accompanied by a Cd vacancy (V_{Cd}); forming a $\text{SO}_2-\text{V}_{\text{Cd}}$ complex defect. According to the crystal symmetry of CdSe, there are two different V_{Cd} surrounding the Se site that SO_2 occupied. In addition, there are various different orientations of SO_2 relative to the V_{Cd} . The lowest energy configuration is identified. Its local vibrational modes along with the modes of other possible orientations can explain the observed values both in terms of the frequencies and the dipole orientations. Further, our nudged elastic band calculations showed that the rotation barrier of the SO_2 in the complex is quite low; indicating the molecule can rotate at reasonable temperature. This is consistent with the experimental observation that the peaks are broadened and merged into one at high temperatures.

1. Introduction

Electronic and optical properties of materials are significantly affected by the presence of defects or impurities in materials. In case of light impurities (compare to the host atoms), for instance hydrogen, oxygen, nitrogen and sulfur defects, infrared (IR) absorption spectroscopy technique has been shown to be a powerful tool for identifying the local structures of such defects in crystals. When the mass of impurity atoms are significantly lighter than that of the host atoms the local vibrational modes (LVMs) associated with them are clearly separated from the host's crystal phonon. The LVM associated with each defect has unique vibrational frequencies depending on the type and local environments. Therefore, LVMs can serve as a fingerprint for identifying each defect in crystals. However, it is difficult to identify the local structure of defects based solely on experimental LVMs. Independent first-principles calculation is usually needed to aid the identification. A combination of first-principles calculations and IR

absorption spectroscopy has been shown to successfully identify the local structure of various defects in crystals, for instance hydrogen-related defects in SrTiO_3 [1,2], H- and N-related defects in ZnO [3–5], and O-related defects in CdTe [6,7].

During 2006–2008, G. Chen et al. nicely observed the LVMs of oxygen-related defects in oxygen-doped CdTe and CdSe by using polarized Fourier transform IR (FTIR) absorption spectroscopy [8–10]. For oxygen-doped CdTe samples, at low temperature, they found a low-frequency LVM at 349.79 cm^{-1} accompanied by two higher-frequency LVMs at 1096.78 and 1108.35 cm^{-1} [10]. They found that the two high-frequency modes merge into a broad peak at $\sim 1104.49 \text{ cm}^{-1}$ when the temperature is increased above $\sim 300 \text{ K}$. The low frequency mode was assigned to the LVM of an oxygen substituting for Te atom (O_{Te}), while the two high frequency modes were assigned to the LVMs of a complex defect between O_{Te} and Cd vacancy ($\text{O}_{\text{Te}}-\text{V}_{\text{Cd}}$). For oxygen-doped CdSe samples, at low temperature they again found two strong absorption peaks at $\gamma_1 = 1094.11$ and $\gamma_2 =$

* Corresponding author at: Department of Physics, Faculty of Science, Kasetsart University, Bangkok 10900, Thailand.

E-mail addresses: pimpika14@gmail.com (P. Pimsorn), fsiewt@ku.ac.th (J. T-Thienprasert), sukit@sut.ac.th (S. Limpijumong).

<http://dx.doi.org/10.1016/j.ceramint.2017.05.231>

Available online 26 May 2017

0272-8842/ © 2017 Elsevier Ltd and Techna Group S.r.l. All rights reserved.

1107.45 cm^{-1} with one additional peak at $\gamma_3 = 1126.33 \text{ cm}^{-1}$ [8]. They attributed this additional peak to the lower symmetry of wurtzite structure (CdSe) compared to zincblende structure (CdTe). These three high LVMS also merge into a single broad peak at the temperature above 560 K. They assigned these high-frequency modes to the LVMS of a complex defect between oxygen substituting for Se and Cd vacancy ($\text{O}_{\text{Se}}\text{-V}_{\text{Cd}}$).

Our group recently calculated and confirmed that Chen et al.'s observed value of 348.79 cm^{-1} is indeed consistent with the LVM associated with the O_{Te} in CdTe (the calculated LVM of 338 cm^{-1}) [7]. However, for the $\text{O}_{\text{Te}}\text{-V}_{\text{Cd}}$ complex defect, the calculated values are only 467 and 197 cm^{-1} [7], which are quite far from the observed values in the 1000 cm^{-1} region. Similarly, for CdSe, our group calculated the LVM of $\text{O}_{\text{Se}}\text{-V}_{\text{Cd}}$ complex defect and obtained the LVMS of 223, 507, and 512 cm^{-1} [7]. Therefore, the observed high-frequency modes in the 1000 cm^{-1} region should come from other O-related defects, not the $\text{O}_{\text{Se}}\text{-V}_{\text{Cd}}$ complexes.

Recently, Lavrov's group reinvestigated the LVMS of oxygen-related defect in oxygen-doped CdTe and CdSe [11–13]. They found the same LVMS in CdTe and CdSe samples as observed in G. Chen's works [8,10]. However, in their work they intentionally added not only oxygen but also sulfur into both CdTe and CdSe samples. In addition to the modes observed by Chen's group, they also carefully looked and found the corresponding modes that are the results of minority S natural isotopes (^{33}S and ^{34}S). Therefore they claimed that the observed LVMS at $\sim 1100 \text{ cm}^{-1}$ in CdTe and CdSe samples involve sulfur-oxygen (SO) complex. For CdTe, T-Thienprasert et al. revealed that SO_2 prefers to substitute for Te and binds with a Cd vacancy; forming a $\text{SO}_2\text{-V}_{\text{Cd}}$ complex defect with two possible configurations. The calculated vibrational frequencies are ~ 1094.9 and 1097.4 cm^{-1} in good agreement with the observed values [14]. In addition, SO_2 in such complex defects can rotate from the metastable configuration to the stable configuration at high temperature. This explains the experimental observation that the two frequencies merged into one at high temperature. For CdSe, which has lower crystal symmetry, the SO complex model is more complicated.

One might wonder why unintentionally doped CdSe samples contain sulfur. Se is a rare element that are naturally found in sulfide minerals of copper iron and lead [15]. That is why S is a common impurity in CdSe. Although, both Chen et al. [8–10] and Bastin et al. [11–13] did not report the concentration of defect responsible for the 1100 cm^{-1} modes, low temperature infrared spectroscopy as used by them are known to highly sensitive to even a trace element. The defects with distinctive LVMS with the concentrations as low as 10^{14} cm^{-3} for thick samples (or 10^{18} cm^{-3} for thin films) can be detected [16].

In this work, we employed first-principles calculations to investigate the SO-related defects in CdSe to seek out the energetically stable configurations and their LVMS that fit experimental observed IR absorption peaks in the $\sim 1100 \text{ cm}^{-1}$ region. To calculate the LVMS, the frozen-phonon approach, which is based on a harmonic approximation, is used. We found that SO_2 in wurtzite-CdSe prefers to bind with V_{Cd} becoming $\text{SO}_2\text{-V}_{\text{Cd}}$ complex defect. There are, however, more possible structures and orientations due to the lower symmetry of wurtzite-CdSe when comparing with the complex in zincblende-CdTe. Their calculated vibrational frequencies are presented and compared with available IR absorption results.

2. Computational method

We used first-principles calculations based on density functional theory (DFT) within local density approximation (LDA) to study sulfur-oxygen related defects in wurtzite-CdSe. The projector augmented wave potentials [17] as implemented in VASP codes [18,19] were employed to describe the electron-ion interactions. The energy cutoff for expanding the plane wave basis set was set at 500 eV and the Monkhorst-Pack scheme [20] with a sampling k -point mesh of $9 \times 9 \times 9$ was used for

primitive cell calculations. The calculated lattice parameters of bulk wurtzite-CdSe are $a = 4.288 \text{ \AA}$ and $c/a = 1.620$, which are in good agreement with the experimental values of $a = 4.302 \text{ \AA}$ and $c/a = 1.630$ [21]. For defect calculations, we used a so-called supercell approach with a supercell size of 96 atoms. The stability and possibility of defect formation could be investigated by calculating the defect formation energy, which is defined by

$$\Delta H_f(D) = E_{\text{tot}}(D^q) - E_{\text{tot}}(\text{bulk}) + \sum_X n_X \mu_X + q(E_F + E_{\text{VBM}} + \Delta V), \quad (1)$$

where $E_{\text{tot}}(D^q)$ and $E_{\text{tot}}(\text{bulk})$ are the total energy of the supercell containing the defect D in charge state q and that of the supercell without any defect (perfect cell), n_X represents the number of atoms which is added to (removed from, if negative) a supercell to create the defect with the corresponding atomic chemical potential μ_X described below, E_F is the Fermi energy referenced to the valence band maximum (E_{VBM}), and the last term represents the correction term for charged defect [22].

To grow a single crystal wurtzite-CdSe under thermodynamic equilibrium, the following condition must be satisfied

$$E_{\text{tot}}(\text{CdSe}) = \mu_{\text{Cd}} + \mu_{\text{Se}}, \quad (2)$$

where $E_{\text{tot}}(\text{CdSe})$ is the total energy per formula unit of CdSe, μ_{Cd} and μ_{Se} are the atomic chemical potentials of Cd and Se, respectively. If μ_{Cd} is limited by the total energy per formula unit of metallic Cd for preventing the existence of such phase in a crystal, we can simply obtain μ_{Se} from Eq. (2). This condition is called Cd-rich growth condition. In opposite, if μ_{Se} is limited by total energy per formula unit of metallic Se, we can again determine μ_{Cd} from Eq. (2). This is called Se-rich growth condition. For the computations of supercell containing S and O, the phase precipitations produced by S and O, such as CdO, CdSO₄, CdS, SeO₂, and SO₂, have to be avoided by limiting the chemical potentials of S and O. We found that under Cd-rich growth condition μ_{O} and μ_{S} are limited by CdO and CdS phases, respectively. Under Se-rich growth condition, μ_{O} and μ_{S} are limited by CdSO₄ and SO₂ phases, respectively.

To compare with the observed IR absorption peaks, we calculated the vibrational modes by constructing a full dynamical matrix. The matrix is constructed by calculating the force acting on each atom in each direction (x , y , and z) as it is perturbed to be slightly shifted from its equilibrium position [7]. The eigenvalues and eigenvectors obtained from the dynamical matrix are the vibrational frequencies and vibrational modes, respectively. To test our calculated approach, we calculated the vibrational frequencies of the SO_2 free-molecule and compared with the corresponding experimental values [23] as illustrated in Table 1. The calculated values are in agreement with the experimental values with the errors of less than 4%.

3. Results and discussions

The local structure of bulk wurtzite-CdSe is depicted in Fig. 1(a). In wurtzite structure, each Cd (as well as Se) atom is four-fold coordinated. All three bond distances between Cd and Se atoms lying near the basal plane (perpendicular to the c axis) are equivalent but are slightly differed from that on the c axis. To investigate the SO-related defects in wurtzite-CdSe, we first studied the behavior of isolated S defect by considering two most stable forms, i.e., substitution for Se site (S_{Se}) and interstitial site (S_i). To determine their stability, we calculated the defect formation energies as a function of Fermi-energy under both Cd-rich and Se-rich growth conditions (Fig. 2). We found that S_{Se} and S_i defects are stable in the neutral charge state with the formation energy of S_i substantially higher than that of S_{Se} defect under both Cd-rich and Se-rich growth conditions. This indicates that the majority of S atom is likely to exist in the form of S_{Se} defect as shown in Fig. 1(b). We further studied a SO-defect by introducing an oxygen atom near S_{Se} defect; forming (SO)_{Se} defect. We found that O atom prefers to bind with the S

P. Pimsorn et al.

Ceramics International 43 (2017) S359–S363

Table 1

The calculated vibrational frequency associated with a free SO₂ molecule and SO₂-related defects in wurtzite-CdSe in comparison with the experimental measured infrared spectroscopy peaks.

Type	Relative Energy (eV)	Mode ¹	Calculated frequency (cm ⁻¹)	Observed frequency (cm ⁻¹)
SO ₂ (molecule)		Sym.	1122.55	1151.4 ²
		Anti-Sym.	1312.91	1361.8 ²
		Bending	499.48	517.7 ²
SO ₂ ⁻		Sym.	827.08	
		Anti-Sym.	937.15	
[SO ₂ ⁻ -V _{Cd}] ⁺	0.12	Sym.	951.12	$\nu_1 = 1094.11^3$
		Anti-Sym.	1046.09	
[SO ₂ ⁻ -V _{Cd}] ⁰	0.00	Sym.	1007.08	$\nu_2 = 1107.45^3$
		Anti-Sym.	1095.39	
[SO ₂ ⁻ -V _{Cd}] ²⁻	0.00	Sym.	1017.99	$\nu_3 = 1126.33^3$
		Anti-Sym.	1103.25	
[SO ₂ ⁻ -V _{Cd}] ³⁻	0.24	Sym.	991.04	
		Anti-Sym.	1122.97	

¹ Sym = Symmetric stretching mode; Anti-Sym. = Anti-Symmetric stretching mode.

² Ref. [8,23].

³ Ref. [8,23].

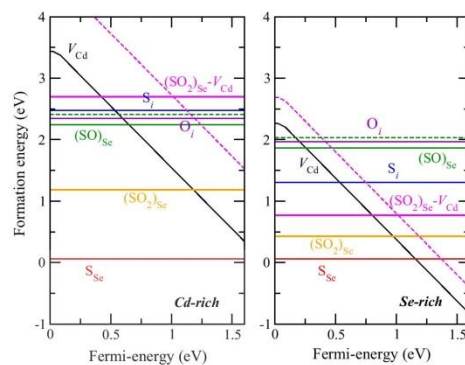


Fig. 2. Defect formation energies as a function of Fermi energy under Cd-rich (left panel) and Se-rich (right-panel) growth conditions. The slope of each line indicates the charge of each defect. The Fermi-energy is plotted from the valence band maximum of CdSe up to the calculated band gap at the special *k*-point to reduce the well-known DFT band gap underestimation.

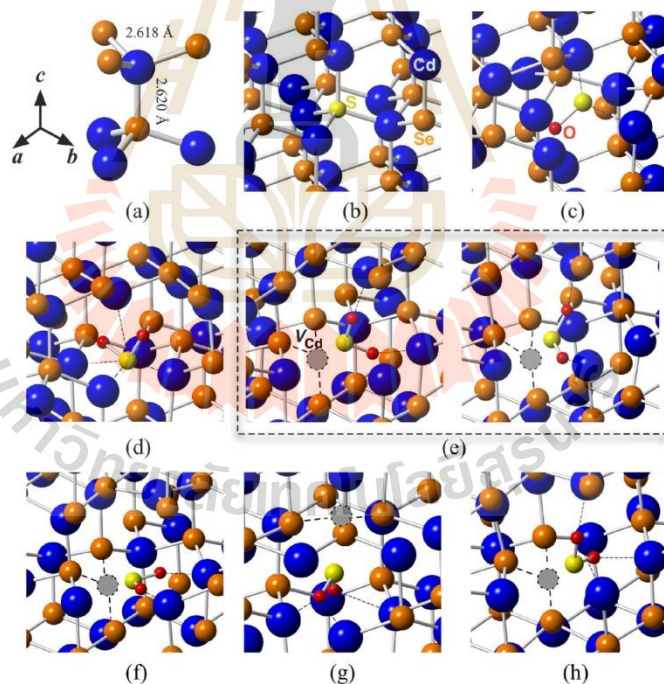


Fig. 1. Schematic illustration of (a) bulk CdSe, (b) S_{Se}, (c) (SO₂)_{Se}, (d) SO₂⁻, (e) [SO₂⁻-V_{Cd}]⁺, (f) [SO₂⁻-V_{Cd}]⁰, (g) [SO₂⁻-V_{Cd}]⁺ and (h) [SO₂⁻-V_{Cd}]³⁻. The blue, brown, red, and yellow spheres represent Cd, Se, O, and S atoms, respectively. (For interpretation of the references to color in this figure legend, the reader is referred to the web version of this article).

atom forming a dumbbell-like structure as shown in Fig. 1(c). The calculation shows that $(\text{SO})_{\text{Se}}$ is also stable in the neutral charge state. However, the formation energy of $(\text{SO})_{\text{Se}}$ is quite high under both Cd-rich and Se-rich growth conditions. The binding energy of $(\text{SO})_{\text{Se}}$ is calculated based on the difference between the sum of the formation energy of isolated defects ($\Delta H_f(\text{S}_{\text{Se}}) + \Delta H_f(\text{O}_i)$) and the formation energy of $(\text{SO})_{\text{Se}}$. In Fig. 2, the two energies are shown using dashed and filled green lines, respectively. Note that O_i defect is charge neutral. Both S and O prefer to form bonds with host Cd atoms and share the Se site. The binding energy of $(\text{SO})_{\text{Se}}$ is only ~ 0.16 eV, which is quite low, indicating that $(\text{SO})_{\text{Se}}$ could form in a low concentration. If another oxygen is added to $(\text{SO})_{\text{Se}}$, the SO_2^+ defect can be formed as shown in Fig. 1(d). Note that, the star symbol “*” is used to distinguish it from the SO_2 free-molecule. This SO_2^+ is also charge neutral and it looks similar to SO_2 free-molecule. Interestingly, the formation energy of SO_2^+ defect is quite low, especially under Se-rich growth condition. The binding energy of SO_2^+ defect is 3.41 eV, which is very high. This indicates that S atom prefers to bond with two oxygen atoms to form SO_2^+ .

We directly calculated the vibrational modes of SO_2^+ . The calculated vibrational frequencies of SO_2^+ are 827 and 937 cm^{-1} for the symmetric and anti-symmetric stretching modes, respectively. (Note that the observed IR peaks should relate to anti-symmetric stretching modes. The symmetric stretching mode has a very weak oscillator strength for infrared spectroscopy.) These calculated values are significantly lower than the observed IR peaks at ~ 1100 cm^{-1} . This suggests that SO_2^+ is not the origin of the observed peaks at ~ 1100 cm^{-1} in CdSe sample. We further investigated complex defects between SO_2^+ and other dominant native defects to seek out the source of the 1100 cm^{-1} mode. Vacancy defects are generally abundant native defects in most materials. In this case, we found that a Cd next to SO_2^+ can be removed; forming $\text{SO}_2^+-\text{V}_{\text{Cd}}$ complex defects. Removing a Cd atom helps relieve the strain near SO_2^+ , which could effectively increase the vibrational frequencies of SO_2^+ . As shown in Fig. 1(d), there are two distinct Cd atoms which could be removed to create the $\text{SO}_2^+-\text{V}_{\text{Cd}}$ complex defects, i.e., beside or above SO_2^+ defect as shown in Fig. 1(e)–(g). In addition, there are many possible orientations of SO_2^+ in each complex structure. In Fig. 1(e) and (f), we illustrate the most stable structures of $\text{SO}_2^+-\text{V}_{\text{Cd}}$ complexes for two nonequivalent configurations that we named them $[\text{SO}_2^+-\text{V}_{\text{Cd}}]^{b1}$ and $[\text{SO}_2^+-\text{V}_{\text{Cd}}]^{b2}$, respectively, where the superscript “b” stands for “beside”. The energies of $[\text{SO}_2^+-\text{V}_{\text{Cd}}]^{b1}$ and $[\text{SO}_2^+-\text{V}_{\text{Cd}}]^{b2}$ are almost identical, indicating that they can co-exist in a comparable concentration. Note that there are two equivalent configurations for $[\text{SO}_2^+-\text{V}_{\text{Cd}}]^{b1}$ as shown in Fig. 1(e). In Fig. 1(g), we show the structure of $\text{SO}_2^+-\text{V}_{\text{Cd}}$ complex when V_{Cd} is created above SO_2^+ defect. This complex is named as $[\text{SO}_2^+-\text{V}_{\text{Cd}}]^a$, where the superscript “a” stands for “above”. The calculated relative energies for different $\text{SO}_2^+-\text{V}_{\text{Cd}}$ complexes are shown in Table 1. The formation energy of $[\text{SO}_2^+-\text{V}_{\text{Cd}}]^{b1/b2}$ is lower than $[\text{SO}_2^+-\text{V}_{\text{Cd}}]^a$, indicating that the former is more likely to form in CdSe sample. The $[\text{SO}_2^+-\text{V}_{\text{Cd}}]^{b1/b2}$ complexes are stable in the neutral charge state and have low formation energies, especially under the Se-rich growth condition. In order to determine the stability, we calculated the binding energy of the complex. In Fig. 2, the dashed pink line represents the sum of the formation energies of the parent isolated defects, i.e., $\Delta H_f(\text{SO}_2^+) + \Delta H_f(\text{V}_{\text{Cd}})$. The binding energy between the SO_2^+ and V_{Cd} to form $[\text{SO}_2^+-\text{V}_{\text{Cd}}]^{b1/b2}$ complex is the energy difference between the dashed and filled pink lines. The binding energy is high when the Fermi energy is in the bottom region of CdSe band gap (i.e., ~ 1 eV from the VBM). However, when the Fermi level is close to the conduction band edge the complex is unbound. In the crystal growth process [8], the CdSe sample was grown with the addition of SeO to provide oxygen and excess Se to suppress the formation of Se vacancy. In other words, the CdSe sample was grown under Se-rich condition. Under Se-rich condition, V_{Cd} defect, which is an acceptor, has low formation energy and becomes a major native defect. Therefore, the Fermi level of SO-doped CdSe sample should be near the VBM;

implying that $\text{SO}_2^+-\text{V}_{\text{Cd}}$ complex defects could exist in the sample.

The vibrational frequencies associated with the $\text{SO}_2^+-\text{V}_{\text{Cd}}$ complexes are calculated and compared with the observed values in Table 1. The vibrational frequencies of the anti-symmetric stretching vibrational modes associated with $[\text{SO}_2^+-\text{V}_{\text{Cd}}]^{b1}$ and $[\text{SO}_2^+-\text{V}_{\text{Cd}}]^{b2}$ complexes are 1095.39 and 1103.25 cm^{-1} , respectively. These are close to the most dominant observed peaks $\gamma_1 = 1094.11$ and $\gamma_2 = 1107.45$ cm^{-1} . The $[\text{SO}_2^+-\text{V}_{\text{Cd}}]^a$ complex gives a somewhat lower frequency than the observed values. As explained earlier, the symmetric stretch modes have small oscillator strengths and are unlikely to be observed in infrared spectroscopy measurement. Therefore, the observed vibrational frequencies γ_1 and γ_2 modes should belong to the vibrational modes of $[\text{SO}_2^+-\text{V}_{\text{Cd}}]^{b1}$ and $[\text{SO}_2^+-\text{V}_{\text{Cd}}]^{b2}$ complexes, respectively. The fact that the formation energy of $[\text{SO}_2^+-\text{V}_{\text{Cd}}]^a$ is higher than that of $[\text{SO}_2^+-\text{V}_{\text{Cd}}]^{b1/b2}$ also support this assignment. In experiment, by using polarized IR absorption measurement, the vibrational direction of γ_1 , γ_2 , and γ_3 modes are determined. It is found that the oscillator direction of γ_2 mode lies close to the basal plane (almost perpendicular to the \hat{c} axis). On the other hand, the oscillator directions of γ_1 and γ_3 modes are pointing by a significant angle ($> 45^\circ$) away from the basal plane. From our calculated results, the vibrational direction of S-O in $[\text{SO}_2^+-\text{V}_{\text{Cd}}]^{b2}$ (see Fig. 1(f)) is almost perpendicular to \hat{c} axis, while that of S-O in $[\text{SO}_2^+-\text{V}_{\text{Cd}}]^{b1}$ (see Fig. 1(e)) make some angle with respect to \hat{c} axis. Therefore, the calculated formation energies, vibrational frequencies and structures are all consistent to assign γ_1 and γ_2 modes to $[\text{SO}_2^+-\text{V}_{\text{Cd}}]^{b1}$ and $[\text{SO}_2^+-\text{V}_{\text{Cd}}]^{b2}$ complexes, respectively. However, the observed vibrational frequency γ_3 at 1126.33 cm^{-1} , which is a minority peak, is left unexplained.

We further explored other meta-stable structures by rotating SO_2^+ in both $[\text{SO}_2^+-\text{V}_{\text{Cd}}]^{b1}$ and $[\text{SO}_2^+-\text{V}_{\text{Cd}}]^{b2}$ complexes. If the SO_2^+ in $[\text{SO}_2^+-\text{V}_{\text{Cd}}]^{b1}$ is rotated away from the equilibrium position and it can be trapped in a metastable state as shown in Fig. 1(h). We will call this state $[\text{SO}_2^+-\text{V}_{\text{Cd}}]^{b3}$ complex. The total energy of this metastable state is 0.24 eV higher than the ground state $[\text{SO}_2^+-\text{V}_{\text{Cd}}]^{b1}$ complex. Therefore, it should exist in a low concentration compared to the ground state one. The calculated vibrational frequencies of $[\text{SO}_2^+-\text{V}_{\text{Cd}}]^{b3}$ are also tabulated in Table 1. The calculated anti-symmetric stretching vibrational frequency is in good agreement with the γ_3 mode. The $[\text{SO}_2^+-\text{V}_{\text{Cd}}]^{b3}$ complex is related with $[\text{SO}_2^+-\text{V}_{\text{Cd}}]^{b1}$ by a simple rotation of SO_2^+ and the orientation of SO_2^+ in these two complexes are quite similar [Fig. 1(e) and (h)].

The $[\text{SO}_2^+-\text{V}_{\text{Cd}}]^{b1}$, $[\text{SO}_2^+-\text{V}_{\text{Cd}}]^{b2}$, and $[\text{SO}_2^+-\text{V}_{\text{Cd}}]^{b3}$ complexes are related to each other by a simple rotation of the SO_2^+ . We have determined the rotational barriers separating each local minima by using a climbing nudge elastic band method [24–27] (cNEB) as implemented in VASP code. Fig. 3 shows the calculated relative energy as a function of configuration coordinate, where the total energy is

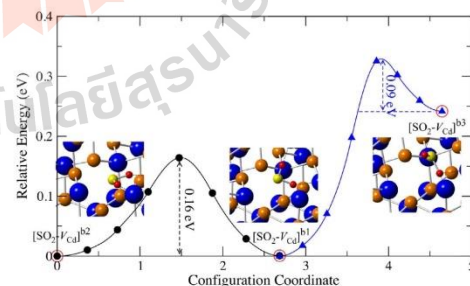


Fig. 3. Calculated energy of the $\text{SO}_2^+-\text{V}_{\text{Cd}}$ complex as SO_2^+ in the complex is rotate to form three different configurations. The total energy on the y axis is referenced to that of the $[\text{SO}_2^+-\text{V}_{\text{Cd}}]^{b1}$ complex.

referred to that of $[\text{SO}_2\text{-V}_{\text{Cd}}]^{b1}$ complex. Based on our calculated results, we found that the migration barrier for rotating SO_2^* between $[\text{SO}_2\text{-V}_{\text{Cd}}]^{b1}$ and $[\text{SO}_2\text{-V}_{\text{Cd}}]^{b2}$ complexes and that between $[\text{SO}_2\text{-V}_{\text{Cd}}]^{b1}$ and $[\text{SO}_2\text{-V}_{\text{Cd}}]^{b3}$ complexes are only 0.16 and 0.09 eV, respectively. These low migration barriers indicate that SO_2^* could rotate and populate the three structures at reasonably low temperatures. At a reasonably high temperature the meta-stable configuration $[\text{SO}_2\text{-V}_{\text{Cd}}]^{b3}$ can also be populated and the configuration is trapped after cooled down; resulting in a minority peak γ_3 . The experiment results also showed that the three sharp peaks at $\sim 1100 \text{ cm}^{-1}$ at very low temperature of 5 K are broadened and merged into one when increasing the temperature [8,9]. This is consistent with the rather low rotation barriers we calculated. Based on our calculated results, the γ_1 , γ_2 , and γ_3 modes are consistent with the vibrational modes of $[\text{SO}_2\text{-V}_{\text{Cd}}]^{b1}$, $[\text{SO}_2\text{-V}_{\text{Cd}}]^{b2}$, and $[\text{SO}_2\text{-V}_{\text{Cd}}]^{b3}$, respectively.

4. Conclusion

Using first-principles DFT calculations, we investigated the origin of the observed IR absorption peaks at $\gamma_1 = 1094.11$, $\gamma_2 = 1107.45 \text{ cm}^{-1}$, and $\gamma_3 = 1126.33 \text{ cm}^{-1}$, which are proposed to be related to the SO_2 complex defects in wurtzite-CdSe. We found that SO_2 prefers to substitute on the Se-site accompanied by a Cd vacancy; forming a $\text{SO}_2\text{-V}_{\text{Cd}}$ complex. The SO_2^* in such complex can rotate and trapped in two stable configurations with almost exactly the same energy with a meta-stable structure that are named $[\text{SO}_2\text{-V}_{\text{Cd}}]^{b1}$, $[\text{SO}_2\text{-V}_{\text{Cd}}]^{b2}$ and $[\text{SO}_2\text{-V}_{\text{Cd}}]^{b3}$, respectively. Our calculated vibrational frequencies associated with the three complexes are in good agreement with the observed values of the γ_1 , γ_2 , and γ_3 modes. By using cNEB method, we found that the migration barriers for rotating SO_2^* are quite low; indicating that SO_2^* can easily rotate. This could make the observed peaks broadening and merged into one as the temperature increased.

Conflict of interest

We declare that we do not have any commercial or associative interest that represents a conflict of interest in connection with the work submitted.

Acknowledgments

This work was partially supported by NANOTEC, NSTDA (Thailand) through its Center of Excellence Network program. P.P. acknowledges the support from the OROG scholarship through Suranaree University of Technology and the Thailand Center of Excellence in Physics (ThEP Center), Commission on Higher Education, Bangkok, Thailand. J.T. is supported by Kasetsart University Research and Development Institute (KURDI).

References

- [1] I. Fongkaew, J. T-Thienprasert, D.J. Singh, M.H. Du, S. Limpjumnong, First principles calculations of Hydrogen-Titanium vacancy complexes in SrTiO_3 , *Ceram. Int.* 39 (2013) S273.
- [2] J. T-Thienprasert, I. Fongkaew, D.J. Singh, M.H. Du, S. Limpjumnong, Identification of hydrogen defects in SrTiO_3 by first-principles local vibration mode calculations, *Phys. Rev. B* 85 (2012) 125205.
- [3] S. Limpjumnong, X.N. Li, S.H. Wei, S.B. Zhang, Probing deactivations in Nitrogen doped ZnO by vibrational signatures: a first principles study, *Physica B* 376 (2006) 686.
- [4] S. Limpjumnong, S.B. Zhang, Resolving hydrogen binding sites by pressure – a first-principles prediction for ZnO, *Appl. Phys. Lett.* 86 (2005) 151910.
- [5] X. Li, B. Keyes, S. Asher, S.B. Zhang, S.-H. Wei, T.J. Coutts, S. Limpjumnong, C.G. Van de Walle, Hydrogen passivation effect in nitrogen-doped ZnO thin films, *Appl. Phys. Lett.* 86 (2005) 122107.
- [6] J. T-Thienprasert, T. Watcharatharapong, I. Fongkaew, M.H. Du, D.J. Singh, S. Limpjumnong, Identification of oxygen defects in CdTe revisited: first-principles study, *J. Appl. Phys.* 115 (2014) 203511.
- [7] J. T-Thienprasert, S. Limpjumnong, A. Janotti, C.G. Van de Walle, L. Zhang, M.H. Du, D.J. Singh, Vibrational signatures of O_{Te} and $\text{O}_{\text{Te-V}_{\text{Cd}}}$ in CdTe: a first-principles study, *Comput. Mater. Sci.* 49 (2010) S242.
- [8] G. Chen, J.S. Bhoale, I. Miotkowski, A.K. Ramdas, Spectroscopic signatures of novel oxygen-defect complexes in stoichiometrically controlled CdSe, *Phys. Rev. Lett.* 101 (2008) 195502.
- [9] G. Chen, I. Miotkowski, S. Rodriguez, A.K. Ramdas, Control of defect structure in compound semiconductors with stoichiometry: oxygen in CdTe, *Phys. Rev. B* 75 (2007) 125204.
- [10] G. Chen, I. Miotkowski, S. Rodriguez, A.K. Ramdas, Stoichiometry driven impurity configurations in compound semiconductors, *Phys. Rev. Lett.* 96 (2006) 035508.
- [11] D. Bastin, E.V. Lavrov, J. Weber, Reassignment of the $\text{O}_{\text{Se-V}_{\text{Cd}}}$ complex in CdSe, *AIP Conf. Proc.* 1583 (2014) 169.
- [12] D. Bastin, E.V. Lavrov, J. Weber, Cadmium vacancy passivated by two hydrogen atoms in CdSe, *Phys. Rev. B* 85 (2012) 195204.
- [13] E.V. Lavrov, D. Bastin, J. Weber, J. Schneider, A. Fauler, M. Fiederle, Reassignment of the $\text{O}_{\text{Te-V}_{\text{Cd}}}$ complex in CdTe, *Phys. Rev. B* 84 (2011) 233201.
- [14] J. T-Thienprasert, S. Limpjumnong, M.H. Du, D.J. Singh, First principles study of O defects in CdSe, *Physica B* 407 (2012) 2841.
- [15] Sources of selenium and tellurium, (http://www.stda.org/se_te.html), 2017.
- [16] M. Stavola, Identification of defects in semiconductors, Academic Press, United States Of America, 1999.
- [17] G. Kresse, D. Joubert, From ultrasoft pseudopotentials to the projector augmented-wave method, *Phys. Rev. B* 59 (1999) 1758.
- [18] G. Kresse, J. Furthmüller, Efficiency of ab-initio total energy calculations for metals and semiconductors using a plane-wave basis set, *Comput. Mater. Sci.* 6 (1996) 15.
- [19] G. Kresse, J. Hafner, Norm-conserving and ultrasoft pseudopotentials for first-row and transition-elements, *J. Phys. Condens. Matter* 6 (1994) 8245.
- [20] H.J. Monkhorst, J.D. Pack, Special points for Brillouin-zone integrations, *Phys. Rev. B* 13 (1976) 5188.
- [21] U. Hojce, C. Rose, M. Binnewies, Lattice constants and molar volume in the system ZnS, ZnSe, CdS, CdSe, *Solid State Sci.* 5 (2003) 1259.
- [22] C.G. Van de Walle, J. Neugebauer, First-principles calculations for defects and impurities: applications to III-nitrides, *J. Appl. Phys.* 95 (2004) 3851.
- [23] W.B. Person, G. Zerbi, Vibrational Intensities in Infrared and Raman Spectroscopy, Elsevier, Amsterdam, 1982.
- [24] D. Sheppard, R. Terrell, G. Henkelman, Optimization methods for finding minimum energy paths, *J. Chem. Phys.* 128 (2008) 134106.
- [25] G. Henkelman, B.P. Uberuaga, H. Jónsson, A climbing image nudged elastic band method for finding saddle points and minimum energy paths, *J. Chem. Phys.* 113 (2000) 9901.
- [26] G. Henkelman, H. Jónsson, Improved tangent estimate in the nudged elastic band method for finding minimum energy paths and saddle points, *J. Chem. Phys.* 113 (2000) 9978.
- [27] G. Mills, H. Jónsson, G.K. Schenter, Reversible work transition state theory: application to dissociative adsorption of hydrogen, *Surf. Sci.* 324 (1995) 305.

Ga acceptor defects in SnO₂ revisited: A hybrid functional studyNirawith Palakawong^{a,b,c,*}, Yi-Yang Sun^c, Jiraraj T-Thienprasert^{b,d}, Shengbai Zhang^c, Sukit Limpijunnong^{a,b}^a School of Physics and NANOTEC-SUT Center of Excellence on Advanced Functional Nanomaterials, Suranaree University of Technology, Nakhon Ratchasima 30000, Thailand^b Thailand Center of Excellence in Physics, Commission on Higher Education, Bangkok 10400, Thailand^c Department of Physics, Applied Physics, and Astronomy, Rensselaer Polytechnic Institute, Troy, NY 12180, USA^d Department of Physics, Faculty of Science, Kasetsart University, Bangkok 10900, Thailand

ARTICLE INFO

Keywords:

First-principles calculations

SnO₂

Impurities

Acceptor defects

ABSTRACT

SnO₂ is one of the most interesting oxide semiconductors due to its wide band gap, good transparency, high thermal/chemical resistances, and low cost. As-grown SnO₂ usually exhibits *n*-type conductivity with high carrier concentrations. Similar to the case of ZnO, it is difficult to dope SnO₂ into *p*-type. Consequently, applications of SnO₂ for optoelectronic as well as electronic devices are limited. In principle, substitution of group-III elements, including Al, Ga, and In, for Sn atom in SnO₂ could give a hole carrier resulting in a *p*-type conductivity. Based on the HSE functional calculations (Varley et al., 2009) [13], it has been reported that these dopants are shallow acceptor defects. However, the calculations with PBE0 functional (Scanlon and Watson, 2012) [14] showed that these dopants are deep acceptors. In this work, Ga-doped SnO₂ are revisited by using HSE functional. We found that Ga_{Sn} defect is indeed a deep acceptor indicating that Ga_{Sn} can serve only as a compensating acceptor defect in SnO₂. Hoping to make the acceptor level shallower, we further study the effect of (compressive) strain on the acceptor level associated with Ga_{Sn} defect by alloying SnO₂ with Si atoms (Si_xSn_{1-x}O₂ alloy where $x = 0.17$). Our results showed that even with the application of strain, the acceptor level remains too deep to be useful.

1. Introduction

Tin dioxide (SnO₂), known as cassiterite in the mineral form, is one of the most interesting ceramics because of its wide band gap, good transparency, high thermal/chemical resistances, and low cost [1,2]. Due to its large direct band gap of ~3.60 eV [3], SnO₂ has been widely applied in various applications, such as transparent conductive oxides (TCOs), solar cells, and solid state gas sensing materials [4–6]. The crystal structure of SnO₂ at room temperature is tetragonal rutile, in which the Sn and O atoms are six-fold and three-fold coordinated, respectively [7]. Usually, as-grown SnO₂ exhibits *n*-type conductivity with a high carrier concentration, which has been attributed to the intrinsic or extrinsic defects [8–11]. There are experimentally reports showing that the electrical conductivity strongly depends on the oxygen availability during the crystal growth process [9,10]. Therefore, the origin of *n*-type conductivity in SnO₂ was assigned to intrinsic defects, especially the oxygen vacancies (V_O) [8,9]. However, there is no direct evidence to support this assignment.

In order to make SnO₂ usable for a wide range of electronic devices, SnO₂ must be able to be doped into both *n*- and *p*-types. However, the inherent *n*-type conductivity in SnO₂ is an obstacle for making it into *p*-type semiconductor. In addition, an effective *p*-type dopant for SnO₂ has not been identified. In principle, substitution of group-III elements for Sn site could make it *p*-type and there are many literatures studying the feasibility of making *p*-type SnO₂ [12–14]. Singh et al. have used density functional theory (DFT) calculations with GGA+*U* method to study SnO₂ doped with group-III elements [12]. They reported that *p*-type SnO₂ could be achieved by replacing Sn atom with Al (Al_{Sn}), Ga (Ga_{Sn}), or In (In_{Sn}) atom. Further, Varley et al. have repeated Singh's calculations by using DFT calculations with more accurate hybrid functional proposed by Heyd-Scuseria-Ernzerhof (HSE) with a default Hartree-Fock mixing parameter of 25% [13]. Their results showed that Al_{Sn}, Ga_{Sn}, and In_{Sn} defects in SnO₂ could act as a shallow acceptor in agreement with Singh's results. However, Scanlon and Watson have reinvestigated the possibility of making *p*-type SnO₂ by using the PBE0 hybrid functional [15] and revealed that these defects could not act as

* Corresponding author at: School of Physics and NANOTEC-SUT Center of Excellence on Advanced Functional Nanomaterials, Suranaree University of Technology, Nakhon Ratchasima 30000, Thailand.

E-mail address: nirawith@gmail.com (N. Palakawong).

<http://dx.doi.org/10.1016/j.ceramint.2017.05.235>

Available online 26 May 2017

0272-8842/ © 2017 Elsevier Ltd and Techna Group S.r.l. All rights reserved.

shallow acceptors contradicting to previous results [14]. In addition, they found that Ga_{Sn} defect is amphoteric with two defect transition levels $\varepsilon(+/0) = 0.54$ eV and $\varepsilon(0/-) = 1.05$ eV. This conflict is interesting and should be clarified. In this work, the Ga_{Sn} defect in SnO_2 is revisited by using DFT calculations with HSE hybrid functional. We found that Ga_{Sn} actually is a deep acceptor with defect transition level $\varepsilon(0/-) = 0.79$ eV.

To find a way to enhance the acceptor concentration, i.e., making the acceptor level shallower, we studied the effects of crystal strain on the acceptor level. It has been illustrated that for the case of Na-doped ZnO , applying the compressive strain can make the acceptor level shallower [16]. To make it more practical, the compressive strain could be introduced by alloying the host material with an isovalent element that has the same crystal structure but with a smaller lattice constant [17]. Here, the compressive strain in SnO_2 is introduced by alloying SnO_2 with Si. Both SiO_2 and SnO_2 have rutile structure, but different lattice parameters, i.e., $a = 4.18$ Å and $c = 2.66$ Å for SiO_2 [18] and $a = 4.74$ Å and $c = 3.19$ Å for SnO_2 [19]. Our results show that applying compressive strain through alloying does not sufficiently shift the acceptor level to a usable value.

2. Computational details

We used first-principles calculations based on density functional theory (DFT) within a plane-wave basis set as implemented in the VASP code [20–22]. The electron-ion interactions were described by the projector augmented wave (PAW) method [23]. The Sn 4d and Ga 3d states were treated as valence electrons. For the exchange-correlation energy, we used both generalized gradient approximation (GGA) parameterized by Perdew, Burke, and Ernzerhof (PBE) [15] and hybrid functional proposed by Heyd, Scuseria, and Ernzerhof (HSE) [24] with a mixing parameter of 0.32. The latter yields the calculated band gap of 3.61 eV in agreement with the experimental value of 3.60 eV [3]. The energy cutoff for expanding the plane wave basis set was set at 306 eV [21]. The spin polarization was treated for all cases with unpaired electrons. For bulk calculations, the Γ -centered grid scheme was used for k -space integration with a sampling mesh point of $3 \times 3 \times 5$. The calculated lattice parameters for SnO_2 obtained from both GGA-PBE and HSE are summarized in Table 1. They are in good agreement with the experimental values. For defect calculations, a supercell approach was employed using a supercell size of 72-atom, i.e., a $2 \times 2 \times 3$ repetition of the 6-atom primitive cell. All atoms in the supercell were allowed to relax until the residue force on each atom became less than 0.025 eV/Å. The chance of Ga substitution for Sn (Ga_{Sn}) could be determined from its formation energy, which is defined by [25]:

$$E^f(\text{Ga}_{\text{Sn}}^q) = E_{\text{tot}}(\text{Ga}_{\text{Sn}}^q) - E_{\text{tot}}(\text{SnO}_2) + \mu_{\text{Sn}} - \mu_{\text{Ga}} + q(E_F + E_{\text{VBM}}), \quad (1)$$

where $E_{\text{tot}}(\text{Ga}_{\text{Sn}}^q)$ is the calculated total energy of a supercell with Ga substitution for Sn in charge state q , $E_{\text{tot}}(\text{SnO}_2)$ is the calculated total energy of a perfect supercell, μ_{Sn} and μ_{Ga} are the atomic chemical potentials described below, and E_F is the Fermi energy referenced to the valence band maximum (VBM) of the perfect cell.

To grow SnO_2 crystal under the thermodynamic equilibrium, it is required that $\mu_{\text{SnO}_2} = \mu_{\text{Sn}} + 2\mu_{\text{O}}$, where μ_{SnO_2} is the total energy of SnO_2

per formula unit, μ_{Sn} and μ_{O} are the atomic chemical potentials for Sn and O, respectively. To prevent the formation of the undesired phases, such as metallic α -Sn and gaseous O_2 , the chemical potentials of Sn and O (μ_{Sn} and μ_{O}) are limited to the energy per formula unit of metallic α -Sn and half of the energy of gaseous O_2 molecule ($\mu_{\text{O}} = E_{\text{tot}}(\text{O}_2)/2$), respectively. For the calculations of Ga defects, the chemical potential of Ga (μ_{Ga}) is limited by β - Ga_2O_3 phase to prevent the formation of gallium oxide phase.

For the formation-energy calculations of charged defect by the supercell approach, there is a fictitious interaction arising from the neighboring cells due to periodic boundary conditions. This error can be reduced by applying a finite-size correction to the defect formation energy defined in Eq. (1). Here, we applied the finite-size correction scheme [26];

$$E_{\text{correct}}^f(\text{Ga}_{\text{Sn}}^q) = E^f(\text{Ga}_{\text{Sn}}^q) + \frac{q^2\alpha}{2\epsilon L}, \quad (2)$$

where $E^f(\text{Ga}_{\text{Sn}}^q)$ is the calculated formation energy obtained from Eq. (1). The last term on the right hand side is the Madelung energy, where α is the Madelung constant, ϵ is the static dielectric constant of material, and L is the linear dimension of the supercell (i.e., $L \sim \Omega^{1/3}$, where Ω is the supercell volume). We set α and ϵ to 2.84 [27] and 12.33 [28], respectively. This gives the calculated Madelung energy for a single charge state ($q = -1$ and $+1$) of Ga_{Sn} defect in the 72-atom SnO_2 supercell to be about 0.17 eV. After applying the finite-size correction as mentioned above, we could determine the defect transition level associated with the defect in two different charge states, i.e., q_1 and q_2 . This level is actually defined as the Fermi-level position at which the formation energies of the defect in the two charge states are equal, i.e.,

$$\varepsilon(q_1/q_2) = \frac{E_{\text{correct}}^f(\text{Ga}_{\text{Sn}}^{q_2}) - E_{\text{correct}}^f(\text{Ga}_{\text{Sn}}^{q_1})}{q_2 - q_1}. \quad (3)$$

To investigate the effect of compressive strain on the defect transition level associated with Ga_{Sn} defect in SnO_2 , four Sn atoms in a bulk 72-atom SnO_2 supercell were replaced with Si atoms to create $\text{Si}_4\text{Sn}_{68}\text{O}_{120}$ alloy with $x \sim 0.17$. While there are many ways to replace four Sn atoms with Si, in this work, four Si atoms were symmetrically substituted on the Sn's sites, as depicted in Fig. 1(a). The cell volume of the $\text{Si}_4\text{Sn}_{68}\text{O}_{120}$ alloy was fully optimized. Then, the Ga_{Sn} defect in this alloy was investigated in two different configurations, as illustrated in Fig. 1(b) and (c), where we labeled them as the Ga *inside* and *outside* Si-clusters, respectively.

3. Results and discussion

The lattice parameters obtained from both GGA-PBE and HSE functionals are tabulated in Table 1 in comparison with the experimental lattice parameters. It can be clearly seen that the calculations with HSE functional give better results when comparing with the experimental values. In addition, the calculated band gap and the heat of formation obtained from HSE functional are 3.61 eV and -6.09 eV, respectively, which are in good agreement with the experimental values of 3.60 eV [3] and -5.99 eV [29]. However, the calculations with HSE

Table 1
The calculated lattice parameters (a and c), internal parameter (u), and cell volume (Ω) of SnO_2 and SiO_2 in the tetragonal rutile structure by using the GGA-PBE and HSE functionals accompanied with the corresponding experimental values.

	GGA-PBE				HSE				Exp.			
	a (Å)	c (Å)	u	Ω (Å ³)	a (Å)	c (Å)	u	Ω (Å ³)	a (Å)	c (Å)	u	Ω (Å ³)
SnO_2	4.77	3.22	0.306	73.21	4.74	3.18	0.306	71.55	4.74	3.19	0.307	71.47 ^a
SiO_2	4.19	2.68	0.306	47.12	4.16	2.66	0.306	46.12	4.18	2.66	0.306	46.54 ^b

^a Ref. [19].

^b Ref. [18].

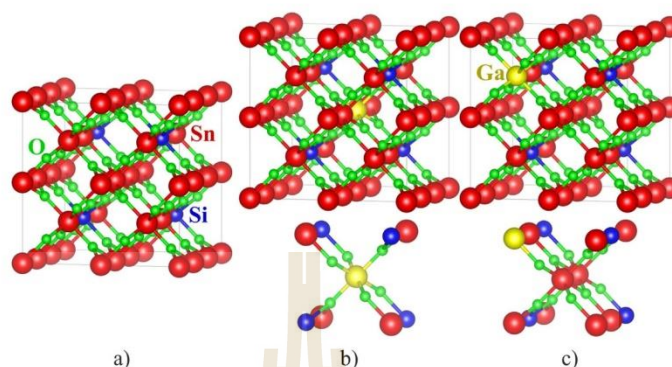


Fig. 1. Schematic illustration of the structures for $\text{Si}_4\text{Sn}_{16}\text{-O}_2$ alloy (a), Ga_{Sn} in $\text{Si}_4\text{Sn}_{16}\text{-O}_2$ alloy at inside (b) and outside (c) Si-cluster configurations. The red, green, blue, and yellow balls represent Sn, O, Si, and Ga atoms, respectively. (For interpretation of the references to color in this figure legend, the reader is referred to the web version of this article.)

functional take much more computational resources compared to the calculations with GGA-PBE functional. Note that the calculated band gap with GGA-PBE functional is only 1.27 eV, which is much lower than the experimental value due to the well-known DFT problems. Moreover, the VBM and CBM positions obtained from GGA-PBE functional are known to be incorrect. Therefore, the HSE functional will be used for further study.

To revisit the study of *p*-type conductivity in Ga-doped SnO_2 , we reinvestigated a Ga substitution for Sn (Ga_{Sn}) in SnO_2 . Because Ga has one less valence electron compared to Sn, Ga_{Sn} is expected to be stable in a negative charge state ($\text{Ga}_{\text{Sn}}^{-1}$) and/or neutral charge state (Ga_{Sn}^0) depending on the electron Fermi energy. For $\text{Ga}_{\text{Sn}}^{-1}$, we found that Ga atom prefers to stay on the Sn site surrounded by six oxygen atoms similar to the geometry of Sn-O bonds in bulk SnO_2 . This configuration is called *on-center* configuration. The six Ga–O bond lengths are 2% shorter than the Sn–O bond lengths in the bulk SnO_2 . For Ga_{Sn}^0 , we found that Ga in the *on-center* configuration is not the lowest-energy configuration. The formation energy can be lowered by breaking a Ga–O bond and shifting the Ga atom from the *on-center* site. The potential energy curve near the saddle point is illustrated in Fig. 2(a). The new

configuration with five Ga–O bonds is called *off-center* configuration as illustrated in Fig. 2(b). The energy different between the *on*- and *off-center* configurations is 0.5 eV; indicating that Ga_{Sn}^0 clearly stables in the *off-center* configuration, or a small-polaron configuration.

When taking into account the proper structural relaxation as explained above, the defect transition level $\varepsilon(0/-)$ associated with Ga_{Sn} is ~ 0.79 eV above the VBM. In addition, the hole states localized on the oxygen atom nearby Ga_{Sn} (see Fig. 2(b)) also reveal the deep characteristic. This means Ga_{Sn} is indeed a deep acceptor which is in agreement with the result of Scanlon and Watson [14]. Based on our results, Ga_{Sn} cannot be a source of *p*-type carriers in SnO_2 .

Recently, it has been proposed that compressive strain could shift the deep acceptor levels to shallower values [16]. It was shown that by applying (hydrostatic) compressive strain to ZnO , the acceptor level of N_{Zn} became shallower and can be used to improve the *p*-type conductivity. For the case of Ga in SnO_2 , the bond compression in the -1 charge state and the configuration distortion in the neutral charge state clearly suggest that the center around Ga prefers compressive strain. In addition, the structural distortion of the neutral charge state (from *on-center* to *off-center*) results in the energy lowering by 0.5 eV. This energy lowering is partially responsible for the very deep acceptor level. In principle, without this structural relaxation, the acceptor level can be 0.5 eV shallower. By analyzing the structure, application of the compressive strain into the SnO_2 host helps shifting the O neighbors closer to the Ga atom (reducing the strain for the -1 charge state) and at the same time might be sufficient to stop the neutral charge state from distorting to the *off-center* configuration (avoiding the structural distortion energy). Therefore, we tested to apply the compressive strain into SnO_2 by adding another element that crystallizes in the same crystal structure as the host, but with a smaller unit cell volume. We found that SiO_2 also has a tetragonal rutile structure with a smaller unit cell volume than that of SnO_2 as shown in Table 1. Therefore, we added Si into SnO_2 forming $\text{Si}_4\text{Sn}_{16}\text{-O}_2$ alloy by symmetrically replacing four Sn atoms in the SnO_2 supercell by four Si atoms as illustrated in Fig. 1(a) and re-optimized the cell volume of $\text{Si}_4\text{Sn}_{16}\text{-O}_2$ alloy. The alloy's volume is explicitly calculated using the GGA-PBE functional. We found that the volume of the alloy is 6.22% smaller than that of SnO_2 as shown in Table 2. After alloying, the tetragonal- SnO_2 has the supercell shape transformed into an almost perfect cubic- $\text{Si}_4\text{Sn}_{16}\text{-O}_2$. As shown in Table 1, the ratio between the unit cell volume of pure SnO_2 and pure SiO_2 obtained using the GGA-PBE and HSE functional are almost exactly the same, i.e., ~ 1.55 . We, therefore, assume the same compression ratio, i.e., $\sim 6.22\%$ compression from bulk SnO_2 , for the HSE calculations of

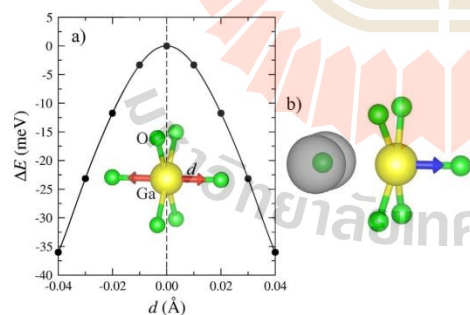


Fig. 2. (a) The total energy (ΔE) of Ga_{Sn}^0 in bulk SnO_2 as a function of the Ga's displacement (d) near the saddle point. The total energy of the Ga_{Sn}^0 at the *on-center* configuration ($d = 0.00$ Å) is set to be zero and the vertical dashed line marks the mirror symmetry point. (b) Ga atom is moved along the Ga–O bond, as indicated by the blue arrow, until one Ga–O bond appears broken and the total energy is reduced by 0.5 eV. The localized hole states on the oxygen atom nearby Ga_{Sn} are depicted as a gray color. (For interpretation of the references to color in this figure legend, the reader is referred to the web version of this article.)

N. Palakawong et al.

Ceramics International 43 (2017) S364–S368

Table 2

The calculated parameters of 72-atom SnO₂ with and without alloying with Si atom. L_x , L_y , and L_z are the expanded cell dimensions in relative to the primitive cell parameters, where $L_x = L_y = 2a$ and $L_z = 3c$. The parameters for the alloy are explicitly calculated only for the GGA-PBE case. For HSE calculations, the compression ratio obtained from the GGA-PBE case (−6.22%) is used to calculate the alloy parameters relative to bulk SnO₂ (the cell shape of the alloy is approximated to be a cube, i.e., $L_x = L_y = L_z = \Omega^{1/3}$).

	GGA-PBE		HSE	
	SnO ₂	Si ₆ Sn _{1−x} O ₂	SnO ₂	Si ₆ Sn _{1−x} O ₂
$L_x = L_y$ (Å)	9.54	9.37(44)	9.48	9.30
L_z (Å)	9.65	9.37(49)	9.55	9.30
Ω (Å ³)	878.51	823.86	858.62	805.20
$\Delta\Omega$ (%)	−6.22		−6.22	

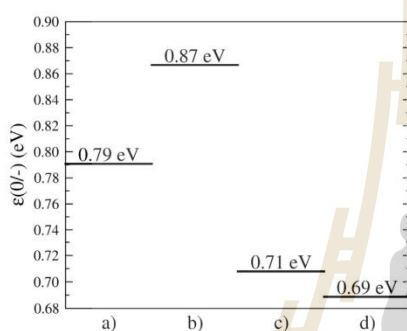


Fig. 3. Defect transition levels $\epsilon(0/-)$ associated with Ga_{Sn} in four configurations, i.e., (a) bulk SnO₂, (b) Si₆Sn_{1−x}O₂ alloy with *inside* configuration, (c) Si₆Sn_{1−x}O₂ with *outside* configuration, and (d) 6.22% compressed bulk SnO₂. In the plot, the valence band maximum for each configuration is set to be zero.

Si₆Sn_{1−x}O₂ alloy.

To study the effects of compressive strain on the defect transition level associated with Ga_{Sn}, we substituted one Ga atom on Sn's site in Si₆Sn_{1−x}O₂ alloy. To test different Sn sites in the alloy, two different configurations were studied: (1) Ga_{Sn} *inside* Si-cluster (Ga_{Sn}ⁱⁿ) and (2) Ga_{Sn} *outside* Si-cluster (Ga_{Sn}^{out}) as shown in Fig. 1(b) and (c), respectively. We found that the relaxations of the neutral Ga_{Sn} remains the same as the non-strain case and the defect transition levels are still very deep. The levels associated with Ga_{Sn}ⁱⁿ and Ga_{Sn}^{out} are 0.87 eV and 0.71 eV above the VBM, respectively. This indicates that the strain effect is not sufficient to enhance the p-type carrier for Ga-doped SnO₂. Even the best case, the acceptor level is reduced by only ~ 0.1 eV.

Further, we investigated whether the change in the transition levels is mainly due to the effect of compressive strain or the effect of atomic Si. We directly compressed the cell volume of SnO₂ with the same ratio as mentioned before without alloying with Si and then replaced one Sn atom with Ga to create Ga_{Sn} defect. We found that under the compression, the defect transition level is 0.69 eV above VBM. This is about 0.1 eV lower than the uncompressed case. The compressive strain helps to make the acceptor level shallower as expected. However, the effect is too small to be useful as the level remains too deep. The defect transition levels associated with Ga_{Sn} defect in bulk SnO₂, Si₆Sn_{1−x}O₂ alloy, and compressed bulk SnO₂ are shown in Fig. 3. Because the acceptor levels in all cases remain deep, we conclude that Ga_{Sn} cannot be a source of hole carrier in SnO₂.

4. Conclusion

We performed first-principles calculations with GGA-PBE and HSE

functionals to study Ga in SnO₂ with and without compressive strain. We found that Ga acts as a deep acceptor in SnO₂ with the ionization energy of ~ 0.8 eV. We further tested the compressive strain effect on the acceptor level. We found that by applying the strain of ~ 6% either by direct compression or alloying with smaller cations (Si), the acceptor level can be lowered but by only about 0.1 eV and the acceptor level still too deep to be useful. Therefore, we conclude that Ga could not be the source of hole carriers in SnO₂.

Conflict of interest

We declare that we do not have any commercial or associative interest that represents a conflict of interest in connection with the work submitted.

Acknowledgments

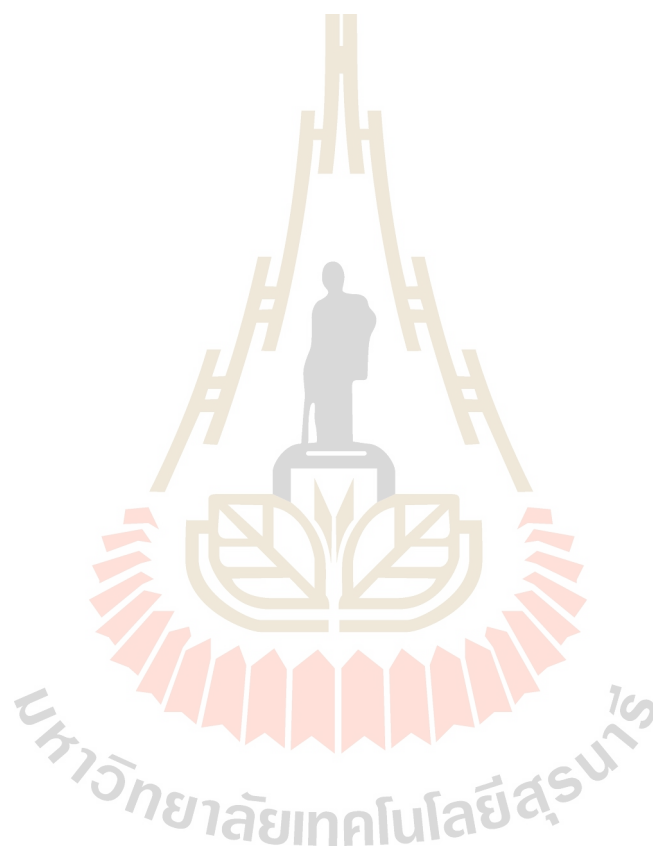
This work was partially supported by NANOTEC, NSTDA (Thailand) through its Center of Excellence Network Program. N.P. is supported by the Thailand Research Fund through the Royal Golden Jubilee Ph.D. Program (Grant no. PHD/0180/2552) and the Thailand Center of Excellence in Physics (ThEP Center), Commission on Higher Education, Bangkok, Thailand. J.T. is supported by the Kasetsart University Research and Development Institute (KURDI), Bangkok, Thailand. The supercomputer time was provided by the Center for Computational Innovations (CCI) at Rensselaer Polytechnic Institute, New York, USA.

References

- [1] Z.M. Jarzebski, J.P. Marton, Physical properties of SnO₂ materials: II. Electrical properties, *J. Electrochem. Soc.* 123 (1976) 299C–310C.
- [2] Z.M. Jarzebski, J.P. Marton, Physical properties of SnO₂ materials: III. Optical properties, *J. Electrochem. Soc.* 123 (1976) 333C–346C.
- [3] K. Reimann, M. Steube, Experimental determination of the electronic band structure of SnO₂, *Solid State Commun.* 105 (1998) 649–652.
- [4] M. Batzill, U. Diebold, The surface and materials science of tin oxide, *Progress. Surf. Sci.* 79 (2005) 47–154.
- [5] H.M. Yates, P. Evans, D.W. Sheel, S. Nicolay, L. Ding, C. Ballif, The development of high performance SnO₂:F as TCOs for thin film silicon solar cells, *Surf. Coat. Technol.* 213 (2012) 167–174.
- [6] G.N. Advani, A.G. Jordan, Thin films of SnO₂ as solid state gas sensors, *J. Electron. Mater.* 9 (1980) 29–49.
- [7] S. Das, V. Jayaraman, SnO₂: a comprehensive review on structures and gas sensors, *Progress. Mater. Sci.* 66 (2014) 112–255.
- [8] C.G. Fonstad, R.H. Rediker, Electrical properties of high-quality stannic oxide crystals, *J. Appl. Phys.* 42 (1971) 2911–2918.
- [9] S. Samson, C.G. Fonstad, Defect structure and electronic donor levels in stannic oxide crystals, *J. Appl. Phys.* 44 (1973) 4618–4621.
- [10] N. Masahiro, S. Shigeo, Properties of oxidized SnO₂ single crystals, *Jpn. J. Appl. Phys.* 10 (1971) 727.
- [11] B. Stjerna, C.G. Granqvist, A. Seidel, L. Häggström, Characterization of rf-sputtered SnO₂ thin films by electron microscopy, Hall-effect measurement, and Mössbauer spectrometry, *J. Appl. Phys.* 68 (1990) 6241–6245.
- [12] A.K. Singh, A. Janotti, M. Scheffler, C.G. Van de Walle, Sources of electrical conductivity in SnO₂, *Phys. Rev. Lett.* 101 (2008) 055502.
- [13] J.B. Varley, A. Janotti, A.K. Singh, C.G. Van de Walle, Hydrogen interactions with acceptor impurities in SnO₂: first-principles calculations, *Phys. Rev. B* 79 (2009) 245206.
- [14] D.O. Scanlon, G.W. Watson, On the possibility of p-type SnO₂, *J. Mater. Chem.* 22 (2012) 2323–2324.
- [15] J.P. Perdew, M. Ernzerhof, K. Burke, Rationale for mixing exact exchange with density functional approximations, *J. Chem. Phys.* 105 (1996) 9982–9985.
- [16] Y.Y. Sun, T.A. Abtew, P. Zhang, S.B. Zhang, Anisotropic polaron localization and spontaneous symmetry breaking: comparison of cation-site acceptors in GaN and ZnO, *Phys. Rev. B* 90 (2014) 165301.
- [17] Y.R. Ryu, T.S. Lee, J.A. Lubguban, A.B. Cormann, H.W. White, J.H. Leem, M.S. Han, Y.S. Park, C.J. Yoon, W.J. Kim, Wide-band gap oxide alloy: BeZnO, *Appl. Phys. Lett.* 88 (2006) 052103.
- [18] W.H. Baur, A.A. Khan, Rutile-type compounds. IV. SiO₂, GeO₂ and a comparison with other rutile-type structures, *Acta Crystallogr. Sect. B* 27 (1971) 2133–2139.
- [19] W. Baur, Über die verfeinerung der kristallstrukturbestimmung einiger vertreter des rutiltyps: TiO₂, SnO₂, GeO₂ und MgF₂, *Acta Crystallogr.* 9 (1956) 515–520.
- [20] G. Kresse, D. Joubert, From ultrasoft pseudopotentials to the projector augmented-wave method, *Phys. Rev. B* 59 (1999) 1758–1775.
- [21] G. Kresse, J. Furthmüller, Efficiency of ab-initio total energy calculations for metals

Manuscript published in *Ceramics International**N. Palakawong et al.**Ceramics International 43 (2017) S364–S368*

- and semiconductors using a plane-wave basis set, *Comput. Mater. Sci.* 6 (1996) 15–50.
- [22] G. Kresse, J. Hafner, Norm-conserving and ultrasoft pseudopotentials for first-row and transition elements, *J. Phys.: Condens. Matter* 6 (1994) 8245.
- [23] P.E. Blöchl, Projector augmented-wave method, *Phys. Rev. B* 50 (1994) 17953–17979.
- [24] J. Heyd, G.E. Scuseria, M. Ernzerhof, Hybrid functionals based on a screened Coulomb potential, *J. Chem. Phys.* 118 (2003) 8207–8215.
- [25] A. Janotti, C.G. Van de Walle, Native point defects in ZnO, *Phys. Rev. B* 76 (2007) 165202.
- [26] G. Makov, M.C. Payne, Periodic boundary conditions in *ab initio* calculations, *Phys. Rev. B* 51 (1995) 4014–4022.
- [27] M. Leslie, N.J. Gillan, The energy and elastic dipole tensor of defects in ionic crystals calculated by the supercell method, *J. Phys. C: Solid State Phys.* 18 (1985) 973.
- [28] K.F. Young, H.P.R. Frederikse, Compilation of the static dielectric constant of inorganic solids, *J. Phys. Chem. Ref. Data* 2 (1973) 313–410.
- [29] E.G. Lavit, B.I. Timofeyev, V.M. Yuldashova, E.A. Lavit, G.L. Galchenko, Enthalpies of formation of tin (IV) and tin (II) oxides from combustion calorimetry, *J. Chem. Thermodyn.* 13 (1981) 635–646.



Abstract submitted for the Siam Physics Congress 2012,
Phra Nakhon Si Ayutthaya (2012)

Siam Physics Congress SPC2012
Past, Present and Future of Physics 9-12 May 2012

First Principles Study of Oxygen Defects in AlN

Nirawith Palakawong^{1,2}, Jiraroj T-Thienprasert^{2,3}, and Sukit Limpijumnong^{1,2*}

¹*School of Physics, Suranaree University of Technology and Synchrotron Light
Research Institute, Nakhon Ratchasima 30000, Thailand*

²*Thailand Center of Excellence in Physics, Commission on Higher Education, Bangkok
10400, Thailand*

³*Department of Physics, Kasetsart University, Bangkok 10900, Thailand*

*Corresponding author. E-mail: sukit@sut.ac.th

Abstract

Aluminium nitride (AlN) is a wide band gap semiconductor which is currently used to alloy with GaN and InN for optoelectronic applications. In the growth processes, oxygen impurity could easily incorporate into AlN crystal and affect its electrical properties. Due to its comparable in size with nitrogen, oxygen should easily substitute on the nitrogen site (O_N). In addition, O might also assume an interstitial position (O_i). In this work, we employed first-principles calculations based on density functional theory (DFT) within the local density approximation (LDA) as implemented in the Vienna *ab initio* simulation package (VASP) to study O impurities in wurtzite AlN. The defect local structures, formation energies, defect states, and density of states of bulk and O impurities in AlN crystal will be discussed.

Keywords: optoelectronic devices, wide band gap semiconductor, first-principles calculations, AlN

มหาวิทยาลัยเทคโนโลยีสุรนารี

Abstract submitted for the Siam Physics Congress 2013, Chiang Mai (2013)

Siam Physics Congress SPC2013
Thai Physics Society on the Road to ASEAN Community 21-23 March 2013

Nitrogen and Oxygen Defects in Group III (Al, Ga, and In) Oxides and Nitrides: First-Principles Calculations

Nirawith Palakawong^{1,2}, Jiraroj T-Thienprasert^{2,3}, and Sukit Limpijumnong^{1,2*}

¹*School of Physics, Suranaree University of Technology and Synchrotron Light Research Institute, Nakhon Ratchasima 30000, Thailand*

²*Thailand Center of Excellence in Physics, Commission on Higher Education, Bangkok 10400, Thailand*

³*Department of Physics, Kasetsart University, Bangkok 10900, Thailand*

*Corresponding author. E-mail: sukit@sut.ac.th

Abstract

Group III oxides and nitrides have been widely studied because of their suitable properties for numerous applications, especially for optoelectronics devices. In the growth processes, oxygen and nitrogen are the common impurities in metal nitride compound (MN) and metal oxide compound (MO), respectively. In MN, oxygen atoms should easily substitute on the nitrogen sites (O_N), whereas, in MO, nitrogen atoms should easily substitute on the oxygen sites (N_O). This is because the oxygen and nitrogen atoms are comparable in size. In this work, we employed first-principles calculations based on density functional theory (DFT) within the local density approximation (LDA) as well as the generalized gradient approximation (GGA) as implemented in the Vienna *ab initio* simulation package (VASP), to systematically study N_O and O_N defects in group III (Al, Ga, and In) oxides and nitrides. The defect transition levels and the stabilities of N_O in MO and O_N in MN were investigated. In order to compare the defect transition levels in different compounds, the band alignments between compounds studied were calculated.

Keywords: First-principles calculations, Density functional theory, Formation energy, Band alignment

มหาวิทยาลัยเทคโนโลยีสุรนารี

Abstract submitted for the RGJ-Ph.D. Congress XIV, Chon Buri (2013)

Concentration Effects on XANES of $\text{Mg}_x\text{Zn}_{1-x}\text{O}$ Alloy: First-Principles Study

Nirawith Palakawong,^{a,b} Jaru Jutimoosik,^a Jiraraj T-Thienprasert,^{b,c} Saroj Rujirawat^{a,b} and Sukit Limpijumnong^{a,b}

^aSchool of Physics, Suranaree University of Technology, Nakhon Ratchasima 30000, Thailand.

^bThailand Center of Excellence in Physics, Commission on Higher Education, Bangkok 10400, Thailand.

^cDepartment of Physics, Kasetsart University, Bangkok 10900, Thailand

Introduction and Objective

Previously, the measurement of Zn and Mg *K*-edge x-ray absorption spectroscopy (XAS), especially for the x-ray absorption near edge structure (XANES) region, on $\text{Mg}_x\text{Zn}_{1-x}\text{O}$ alloy samples were studied [S. Limpijumnong *et al.*, *Appl. Phys. Lett.* **99**, 261901 (2011)]. In that work, the two local structure models were considered, four-fold (from the pure wurtzite ZnO) and six-fold coordinated (from the pure rocksalt MgO). For the Zn *K*-edge, the linear combination fits based on the two mentioned models were in good agreement with the experimental results. However, for the Mg *K*-edge, the deficiency of the linear combination fits can be detected. In this work, based on first-principles calculations and density functional theory, the Zn and Mg *K*-edge XANES spectra will be simulated to study the effects of the concentration on the XANES features.

Methods

This work was based on first-principles density functional calculations using the projector augmented wave (PAW) method as implemented in the Vienna *ab initio* simulation package (VASP) codes with an energy cutoff of 500 eV for the plane wave basis set. We used the local density approximation (LDA) for the exchange-correlation potential. A supercell approach was performed for defect calculations. The Monkhorst-Pack scheme with a sampling mesh of $2 \times 2 \times 2$ was used for *k*-space integration. FEFF 8.2 code was used to simulate XANES spectra.

Results

From the defect formation energy calculations, we found that the substitutional Mg (Mg_{Zn}) is electrically neutral and does not prefer to bind with native defects and unlikely to form Mg clusters. From the inconsistency in a linear combination fit of the Mg *K*-edge XANES spectra, we proposed that there could be an additional form of Mg, possibly five-fold Mg (of HX-MgO).

Conclusion

We suggest that the deficiency of the model for Mg *K*-edge could be treated by including the XANES spectrum of MgO in HX structure as a basis in the linear combination fits.

Keywords: x-ray absorption spectroscopy, first-principles calculation, $\text{Mg}_x\text{Zn}_{1-x}\text{O}$ alloy

Selected References:

1. Limpijumnong, S.; Jutimoosik, J.; Palakawong, N.; Klysubun, W.; Nukeaw, J.; Du, M. H.; Rujirawat, S. *Appl. Phys. Lett.*, **2011**, *99*, 261901.

Abstract submitted for the 26th International Conference on Defects in
Semiconductors, Nelson, New Zealand (2011)



ICDS Abstract Template



First principles study of Mg-doped ZnO

ABSTRACT

The role of Magnesium as an impurity in Zinc oxide (ZnO) is studied. While the focus of recent research is on the MgO-ZnO alloys for bandgap engineering purposes, this work is focused on the diluted Mg conditions. Based on first-principles calculations and density functional theory, the Mg impurities in both substitutional and interstitial forms are studied. Their comparative stabilities and possible charge states are reported for different growth and carrier conditions. To aid experimental identifications, Mg *K*-edge x-ray absorption spectra (XAS), especially for the x-ray absorption near edge structures (XANES) region, are simulated based on the local structure models obtained from the calculations.

มหาวิทยาลัยเทคโนโลยีสุรนารี

Abstract submitted for the 3rd Academic Conference on Natural Science for Master and PhD Students from ASEAN Countries, Phnom Penh, Cambodia (2013)

FIRST PRINCIPLES STUDY OF OXYGEN SUBSTITUTIONAL DEFECT IN GROUP III NITRIDES

Nirawith Palakawong^{a,b,*}, Jiraroj T-Thienprasert^c, and Sukit Limpijumngong^{a,b}

^{a)} School of Physics and NANOTEC-SUT Center of Excellence on Advanced Functional Nanomaterials, Suranaree University of Technology, Nakhon Ratchasima 30000, Thailand

^{b)} Thailand Center of Excellence in Physics, Commission on Higher Education, Bangkok 10400, Thailand

^{c)} Department of Physics, Faculty of Science, Kasetsart University, Bangkok 10900, Thailand
E-mail: nirawith@gmail.com

Group III-nitride materials have been widely studied due to their suitable properties for numerous applications, especially for optoelectronic devices. Light impurity elements, especially oxygen, can easily incorporate into these materials during growth. They can strongly affect material properties. Due to a comparable in size, an oxygen atom prefers to substitute for the nitrogen in this class of materials and acts as a donor defect. In this work, we employed first-principles calculations based on density functional theory (DFT) within the local density approximation (LDA) as well as the generalized gradient approximation (GGA) as implemented in the Vienna *ab initio* simulation package (VASP), to systematically study the oxygen substituted for nitrogen (O_N) defect in AlN, GaN and InN. The defect local structures, formation energies, and defect states were investigated. In order to compare the band positions between different compounds, the band alignment method is carried out to align the band positions for each compound with the universal reference, i.e., vacuum level.

Keywords: First-principles calculations, Density functional theory, III-Nitride, Defect

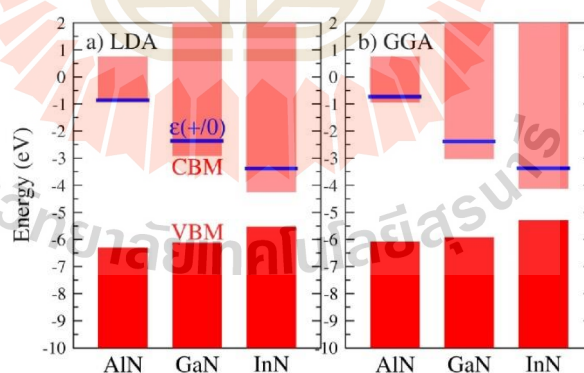


Fig. 1. Illustration of valence-band maximum (VBM), conduction-band minimum (CBM) and defect transition level ($\epsilon(+0)$) with respect to the vacuum level for AlN, GaN, and InN calculated by using (a) LDA and (b) GGA for the exchange-correlation energy.

Abstract submitted for the 10th Asian Meeting on Electroceramics,
Taipei, Taiwan (2016)

AMEC-2016
The 10th Asian Meeting on Electroceramics
Dec. 04-07, 2016, Taipei, Taiwan

Ga Acceptor Defects in SnO₂ Revisited: A Hybrid Functional Study

Nirawith Palakawong^{1,2,3}, Yiyang Sun³, Jiraroj T-Thienprasert^{2,4},
Shengbai Zhang³, and Sukit Limpijumnong^{1,2,*}

¹*School of Physics and NANOTEC-SUT Center of Excellence on Advanced Functional Nanomaterials,
Suranaree University of Technology, Nakhon Ratchasima 30000, Thailand*

²*Thailand Center of Excellence in Physics, Commission on Higher Education,
Bangkok 10400, Thailand*

³*Department of Physics, Applied Physics, and Astronomy, Rensselaer Polytechnic Institute,
Troy, New York 12180, USA*

⁴*Department of Physics, Faculty of Science, Kasetsart University, Bangkok 10900, Thailand*

SnO₂ is one of the most interesting oxide semiconductors due to its wide band gap, good transparency, high thermal/chemical resistances, and low cost. As-grown SnO₂ usually exhibits *n*-type conductivity with high carrier concentrations, which is attributed to the existences of V_O and/or H defects in a crystal. This is a big obstacle to make it become *p*-type semiconductor similar to the case of ZnO. Consequently, applications of SnO₂ for optoelectronic as well as electronic devices are limited. In theory, substitution of group-III elements, including Al, Ga, and In, for Sn atom in SnO₂ could give a hole carrier resulting in a *p*-type conductivity. Based on the HSE functional calculation [Phys. Rev. B **79**, 245206 (2009)], it has been reported that these dopants are shallow acceptor defects. In contrast, the calculations with PBE0 functional [J. Mater. Chem. **22**, 25236 (2012)] reveals that these dopants are deep acceptors. In this work, Ga-doped in SnO₂ are revisited by using HSE functional. Our results reveal that Ga_{Sn} defect is actually a deep acceptor; indicating that Ga_{Sn} can serve only as a compensating acceptor defect in SnO₂. We further study the effect of strain on the acceptor level associated with Ga_{Sn} defect by alloying SnO₂ with Si atoms (Si_xSn_{1-x}O₂ alloy where *x* ~ 0.17). Nevertheless, we find that introducing the strain into SnO₂ could not affect such acceptor level.

Keywords: first-principles calculations; SnO₂; Ga; acceptor defects

* Corresponding author's email: sukkit@sut.ac.th

CURRICULUM VITAE

Mr. Nirawith Palakawong was born on May 26, 1984 in Narathiwat province, one of the southern provinces of Thailand. He received his Bachelor degree in physics with second-class honor from Department of Physics, Faculty of Science and Technology, Thammasat University in 2008. After he graduated in Bachelor degree, he has been continued to study Master program at School of Physics, Institute of Science, Suranaree University of Technology and granted the scholarships from the provides scholarships for graduate students which faculty members get the research grants from the external funding sources program. In 2009, he was past a qualifying examination and upgraded his program to Ph.D. program (For B.Sc. holder) and granted the scholarship from the Thailand Research Fund under the Royal Golden Jubilee Program to pursue a Ph.D. degree under the supervision of Prof. Dr. Sukit Limpijumng. He interested in condense matter physics using first-principles and density functional calculations. He has participated to several national/international conferences (listed in APPENDIX B) and got the outstanding poster presentation award from the 10th Asian Meeting on Electroceramics, Taipei, Taiwan. His publications are also listed in APPENDIX B.